Astrochemistry in Interface Regions

Tammay K Nguyen

Thesis submitted for the Degree of Doctor of Philosophy

of the University of London

Department of Physics & Astronomy

UNIVERSITY COLLEGE LONDON

2002 January 7

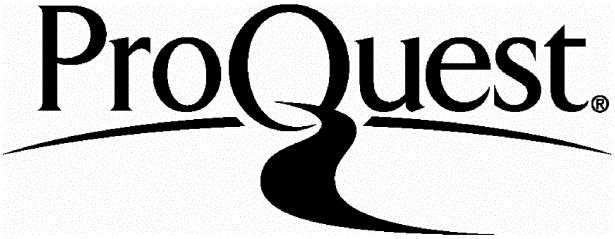

ABSTRACT

This thesis is concerned with the chemical modelling of molecular species in a selection of interface layers between astrophysically interesting environments. The aim is to identify 'tracers' for the theoretical scenarios studied, and to try to explain observational data presently available. These tracers can give detailed information concerning the physical conditions in the environment, and may also help to determine its evolutionary status. The ordering of the discussions will reflect the increasingly energetic processes present in each of the different environments studied.

Firstly discussed in Chapter 2, is the formation of water ice mantles, in relatively quiescent regions. Using gas-grain chemical models, water ice is studied under a variety of physical conditions. We find that at low A_V water ice can be present in clouds at late times or if the cloud is clumpy. Chapters 3 and 4 concentrate on interface layers in progressively more energetic regions. These scenarios range from the mixing of cold molecular gas with warm ionized gas, coupled with the presence of a modestly enhanced ionization rate to the turbulent boundary layers of a diffuse cloud, in which high temperatures and pressures are present. In Chapter 3, we find that at temperatures greater than 100 K, a rich and abundant chemistry can exist. In Chapter 4, we find if an interface layer occupies a few percent of the total column, many polyatomic species in the interface should have detectable abundances. Finally, in Chapters 5 and 6 consideration is moved to the most energetic environments.

In Chapter 5, we simulate x-ray ionization in dark clouds and include the formation of C^{++}, and find that the abundance of CH^+ is significantly enhanced when C^{++} is included in the reaction network. In Chapter 6 we study photon dominated regions above disks surrounding main sequence stars and find that the chemical processing produces a large number of tracers with significant column densities.

"For those who believe

no explanation is necessary,

For those who do not

no explanation will suffice."

–

from "The song of Bernadette"

by Franz Werfel

Contents

List of Figures

List of Tables

CHAPTER 1

Introduction to Astrochemistry

"In general it is a good morning exercise for a researcher to destroy a favourite hypothesis every day before breakfast - it keeps him young."

– Konrad Lorenz

The first detection of matter in the interstellar medium was made by Hartmann (1904), who observed absorption from Ca II at 3934 Å. The first interstellar molecules observed include CH, CH^+ and CN, which were detected between 1937 and 1941. These detections have sparked a new and exciting branch of astronomy: astrochemistry.

There are now over 100 identified molecular species in our Galaxy, which are found to lie within the interstellar medium. The interstellar medium itself is made of a number of distinct regions and contains a number of different interstellar cloud types. A list of the properties for regions of interest in this study is given in Table 1.1.

The observed molecules are 'tracers' of gas in the interstellar medium and the theoretical astrochemical study of these molecules is important because the information on the molecular content of a region can be used as a diagnosis of the physical

conditions within the region being studied. In this thesis, we concentrate on investigating the interface layer between two different regions in the interstellar medium, in the hope that distinctive tracers of the layer can be identified. Interface layers are especially interesting because they can provide information on a number of different dynamical processes occurring within them, such as the extent of the mixing occurring between the two regions. Studying the molecular content may also provide clues concerning the physical conditions within the layer. Identified tracers may also help us determine the evolutionary status of the layer and its surrounding area.

Such interface layers have been probed in the past, and these studies include those made by Charnley *et al.* (1990); Duley *et al.* (1992) and Rawlings and Hartquist (1997). Charnley *et al.* (1990) looked at the chemical evolution in molecular clump–stellar wind interfaces, Duley *et al.* (1992) made a study of a diffuse cloud–intercloud interface to identify possible mechanisms for the production of CH^+, while Rawlings and Hartquist (1997) considered a diffusive boundary layer between dark star–forming cores and warm, shocked T–Tauri winds, assuming that turbulence–driven diffusion is occurring.

In this chapter, we will describe how the modelling of these interface regions is accomplished. In §1.1 and 1.2 a more detailed description of diffuse and dark clouds respectively, will be given. These are two cloud types of particular interest in this work. §1.3 gives a brief discussion of dust grains. In §1.4 we describe the processes by which different species are formed within diffuse and dark clouds. In §1.5 we give a description of the physical model of the clouds as well a as brief discussion of the codes used and finally in §1.6 we discuss the grain surface physical processes.

Table 1.1: Physical conditions in interstellar diffuse and dark clouds.

Most of the interstellar space is occupied by very hot 'coronal' gas and by warm interstellar gas.

Hot 'coronal' gas	$T^{\dagger} \sim 10^6$ K, $n_{\rm H}{}^{\ddagger} \leq 10^{-2}$ cm^{-3}, which is heated by supernovae shocks.
Warm interstellar gas	$T \sim 10^3$ K, $n_{\rm H} < 1$ cm^{-3}, which is heated by x–rays.
Region around massive stars	$T \sim 10^4$ K, $n_{\rm H} \sim 10^2$ cm^{-3}, which is heated by the copious UV radiation from the star.

However, these regions are not chemically important. Diffuse and dark clouds are the regions where molecules are observed. Together, these regions occupy only a few percent of the interstellar volume, but contain almost all the mass.

Diffuse clouds	$T \sim 100$ K, $n_{\rm H} \sim 100$ cm^{-3}.
Dark clouds	$T \sim 10$ K, $n_{\rm H} \sim 10^4$ cm^{-3}.

Diffuse clouds are readily penetrated by starlight since the dust extinction is less than one optical depth in the visual. Radiative processes dominate the chemistry in these regions. Stellar radiation is largely excluded from dark clouds. Both regions are freely penetrated by cosmic–rays (fast protons and electrons). Cosmic–rays cause ionization which promotes chemistry in the clouds.

† T = kinetic temperature; ‡ $n_{\rm H}$ = number density of H nuclei.

1.1 Diffuse Clouds

A simple definition of a diffuse cloud is that of a parcel of gas and dust through which one can still see background stars (Meyer, 1997). The extinction caused by the dust in a diffuse cloud is usually taken to be $A_V \leq 2$ mag, therefore starlight can easily pass through these regions. This penetration of starlight means that the UV and optical radiation inhibits the formation of molecular species within the clouds.

A typical example of a diffuse cloud is ζ Ophiuchus, which is a bright early type star at a distance of $\sim$ 130 pc from the Sun. It is found that the light from the star is obscured by at least two distinct diffuse clouds in the line–of–sight. UV and optical absorption lines of molecules have enabled us to determine physical conditions including densities, temperatures and radiation fields.

The molecules which have been detected in diffuse clouds include H_2, CO, OH, NH, CH, CH^+, CN and C_2. Liszt and Lucas (2001) have made a recent study of a number of diffuse clouds in the line–of–sight towards a sample of compact extragalactic mm-wave continuum sources and detected a number of further species including HCO^+, C_2H and C_3H_2.

1.2 Dark Clouds

Many of the identified molecular species are observed to lie within relatively dense clouds. Unlike diffuse clouds, these regions are opaque to visible and UV radiation, which is due to the high concentrations of dust within them. Such clouds are known as dark or molecular clouds. Typical dark clouds are known as sources of star and planetary system formation and within these clouds dense clumps often exist (which have $T \sim 10$ K and $n_H \sim 10^{4-5}$ cm^{-3}). A giant molecular cloud is an association of molecular clouds, which have been swept together by galactic–wide events.

An example of a dark cloud is TMC–1 (Taurus Molecular Cloud – 1), which is at a distance of $\sim$ 140 pc in Taurus. Ohishi and Kaifu (1998) recently made an exten-

sive spectral line survey towards TMC–1 using the 45 m mm–wave telescope of the Nobeyama Radio Observatory, National Astronomical Observatory of Japan. They detected 404 lines from 38 molecules including 11 previously undetected molecules (including C_6H, CCO, CCCO, CCS, CCCS, HNCCC, HCCNC, $HCCCNH^+$, HCCCHO, CH_2CN and C_3H). In total, 40 types of molecules have been detected in TMC–1, including CO, HCN and HCO^+.

1.3 Dust Grains

The surfaces of dust grains may provide sites for the formation of molecular species. A prime example of such a species is molecular hydrogen. Hydrogen is the most abundant species in the Universe and it is generally accepted that H_2 molecules are formed on the surface of dust grains (Hollenbach and Salpeter, 1971, given in reaction 1.1).

$$H + H : \text{grain} \longrightarrow H_2 + \text{grain} \tag{1.1}$$

The dust grain (with an atomic hydrogen attached to its surface) acts as a sink (third body) for the excess energy that must be lost by the combining pair. Upon formation, the H_2 molecule is immediately returned to the gas–phase. Assuming that every H atom sticking to the surface of a grain ultimately leaves as part of a H_2 molecule, then the rate of formation by this process is given by equation 1.2.

$$\frac{dn_{H_2}}{dt} = \frac{1}{2}(n_H \, \pi \, a^2 n_g \, v(H) P), \tag{1.2}$$

which is equivalent to the collision rate of H atoms striking the grain surface, times the sticking probability. n_H is the number density of H atoms, n_g is the number density of grains, a is the radius of the grain, $v(H)$ is the velocity of the bombarding H atom and P is the sticking probability. The rate given in equation 1.2 is clearly the maximum possible rate for H_2 formation.

To explain the observed fractional abundance of a number of other species (including water ice, NH and CN) also requires the use of surface grain formation. This is because their respective gas–phase chemistries are insufficient to account for their observed abundances Molecules trapped in ices on interstellar grains can in certain circumstances rapidly desorb (via a number of processes including thermal desorption, non–thermal desorption and photo–desorption), thereby significantly enhancing their gas–phase abundances.

1.4 Gas–phase Chemical Network

There are two main methods for the formation of interstellar molecules. The first involves grain surface reactions (as discussed in §1.3 and the second is gas–phase molecular formation. Observations of molecules suggest that both formation methods are important, the effectiveness of each depending on the molecule. In this section, we will concentrate on gas–phase reactions. A discussion of grain surface reactions is given in § 1.6.

Chemical networks consisting of gas–phase atoms responsible for the formation of more complex molecules have been widely studied (e.g. Dalgarno and Black (1976); Dalgarno (1976*b*); Watson (1978)). Consider the physical processes occurring when a molecule is formed. There are three molecular bond processes (i) formation (ii) destruction and (iii) rearrangement. Molecular bonds may either be formed in the gas–phase by radiative association reactions ($X + Y \rightarrow XY + h\nu$), or on grain surfaces. The molecular bonds can be destroyed by photodissociation reactions ($XY + h\nu \rightarrow X + Y$), which are common in diffuse and translucent clouds where UV radiation can easily penetrate, or dissociative recombination reactions ($XY^+ + e^- \rightarrow X + Y$), which can be rapid at low temperatures. The final process involves the rearrangement of molecular bonds, which can be accomplished via ion–molecule exchange reactions ($X^+ + YZ \rightarrow XY^+ + Z$), charge transfer ($X^+ + YZ \rightarrow X +$

YZ^+) and neutral–neutral reactions (X + YZ → XY + Z).

It has been shown that ion–molecule reactions, rather than radiative association reactions, are an efficient mechanism for molecular formation. Both experimental and quantum mechanical calculations have shown that ion–molecule reactions have very high rate coefficients, often corresponding to a reaction occurring on almost every collision. Conversely radiative association reactions are inefficient since the X–Y system needs to lose excess energy while they are in contact, otherwise the system would be forced apart. While the atoms are separated they posses kinetic energy, when they approach each other this kinetic energy increases due to a mutual attractive force. As they collide they will start to repel each other, due to their overlapping charge clouds and unless an energy equivalent to the bond energy of the system is removed the molecule will fall apart (Duley and Williams, 1984). Neutral–neutral reactions were also thought to be inefficient at low temperatures; however radical–radical (e.g. CN + O_2) and radical–unsaturated molecule (e.g. CN + C_2H_2) reactions have recently been studied in the laboratory and found to be efficient.

1.4.1 Chemical Networks

A brief discussion of the main reaction networks of H, C, O, N and S is given below.

1.4.1.1 Hydrogen Chemical Network

In the gas–phase, H_2 can be ionized and the products are used to drive the chemistry in the cloud, thereby producing more complex molecules. H_2 is ionized by cosmic–rays to form a H_2^+ ion which rapidly reacts with another H_2 to form H_3^+, in the following sequence,

$$H_2 + \text{c.r.} \longrightarrow {H_2}^+ + e^- \tag{1.3}$$

$${H_2}^+ + H_2 \longrightarrow H_3^+ + H. \tag{1.4}$$

H_3^+ then participates in more complex chemical networks involving proton transfer (H_3^+ has a small proton affinity, therefore it can easily transfer protons to most atoms and molecules in the interstellar medium), molecular hydrogen abstraction and dissociative recombination with electrons. This is seen in the reaction sequence 1.5-1.9.

Proton transfer initiates the formation of other species,

$$O + H_3^+ \longrightarrow OH^+ + H_2 \tag{1.5}$$

followed by H Abstraction:

$$OH^+ + H_2 \longrightarrow H_2O^+ + H \tag{1.6}$$

$$H_2O^+ + H_2 \longrightarrow H_3O^+ + H \tag{1.7}$$

and Dissociative Recombination:

$$H_3O^+ + \text{electron} \longrightarrow H_2O + H \tag{1.8}$$

$$\longrightarrow OH + H_2 \tag{1.9}$$

Molecular hydrogen can also be destroyed by photodissociation through a line excitation process. Although H_2 is self-shielding, therefore while the molecules in the outer regions of the cloud are destroyed via direct photodissociation, the molecules in the inner region become shielded from the UV and remain unaffected.

1.4.1.2 Carbon Chemical Network

The ionization potential of atomic carbon is less than 13.6 eV, therefore carbon exists mainly as C^+ in diffuse clouds. However, in dark clouds, shielding of atomic carbon from the background radiation means that it is present mainly in the form of C and CO.

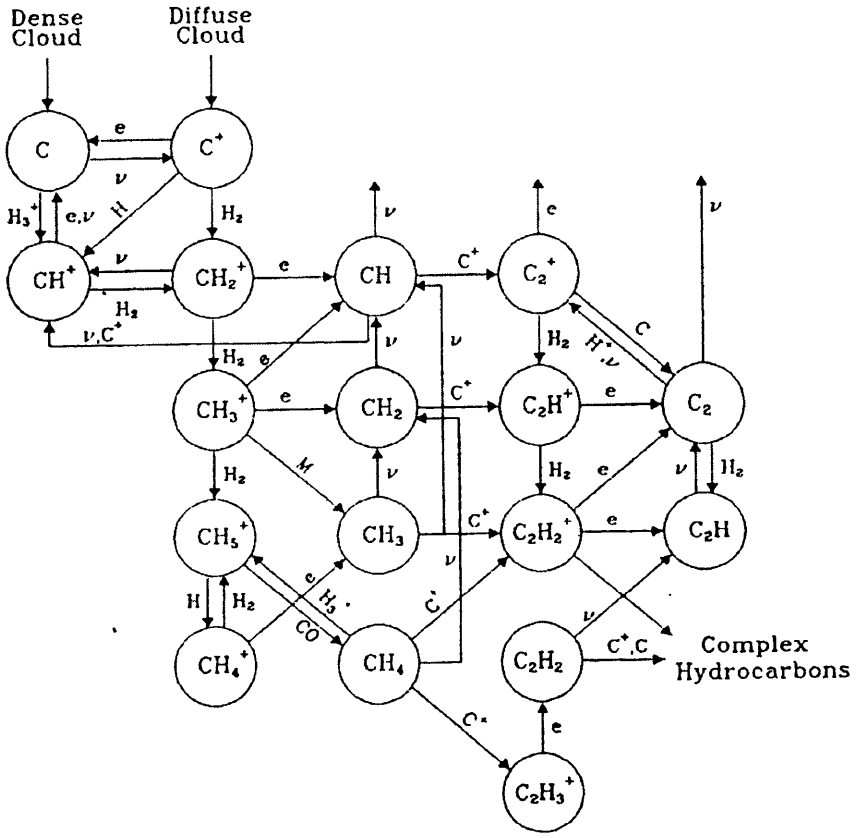

Figure 1.1: Schematic diagram of the main reactions in the carbon chemical network in diffuse and dark clouds. Figure taken from van Dishoeck (1998).

In diffuse clouds the carbon chemistry is initiated by the reaction,

$$C^+ + H_2 \longrightarrow CH_2^+ + h\nu \tag{1.10}$$

Although this reaction proceeds slowly, once formed the CH_2^+ ion rapidly reacts with H_2 molecules to form CH_3^+. The CH_3^+ ion reacts with electrons to form CH and CH_2.

In dark clouds carbon chemistry is initiated when C reacts with H_3^+ forming CH^+,

$$C + H_3^+ \longrightarrow CH^+ \xrightarrow{H_2} CH_2^+ \xrightarrow{H_2} CH_3^+ \tag{1.11}$$

In these regions CH_3^+ reacts with species such as O, CO and HCN to form

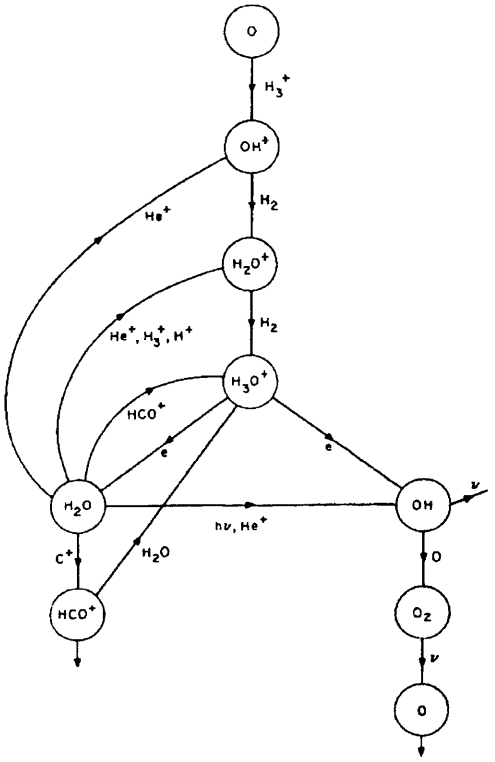

Figure 1.2: Schematic diagram of the chemistry of OH and H_2O in dense clouds. Figure taken from Sternberg *et al.* (1987).

CO, CH_2CO and CH_3CN respectively. The carbon chemical network is depicted in Fig. 1.1.

1.4.1.3 Oxygen Chemistry Network

Unlike carbon, oxygen is mainly neutral, even in diffuse clouds. The oxygen chemical network is therefore initiated with reactions with H_3^+ (given in equation 1.5). If the gas temperature is sufficiently high (T > 100 K), atomic oxygen may react with H^+, to form OH^+ via the following sequence,

$$O + H^+ \longrightarrow O^+ + H \tag{1.12}$$

$$O^+ + H_2 \longrightarrow OH^+ + H \tag{1.13}$$

The OH^+ ion rapidly produces OH and H_2O, via the reaction sequence depicted in Fig. 1.2.

Oxygen bearing molecules are mainly destroyed by photodissociation or reactions with C^+; OH may form CO^+, which can lead to HCO^+ and CO being formed.

1.4.1.4 Nitrogen Chemistry Network

Unlike C and O chemistries, the nitrogen chemical network at low temperatures is not initiated by reactions with H_3^+ ions because the reaction is endothermic. Instead, the nitrogen network is initiated by neutral–neutral reactions with OH and CH to form NO and CN respectively.

$$N + OH \longrightarrow NO + H \tag{1.14}$$

$$N + CH \longrightarrow CN + H \tag{1.15}$$

The nitrogen chemistry may also be initiated with a nitrogen ion reacting with molecular hydrogen, which when followed by further hydrogen abstraction and dissociative recombination reactions can produce molecules such as NH, NH_2 and NH_3.

$$N^+ + H_2 \longrightarrow NH^+ + H \tag{1.16}$$

$$NH^+ + H_2 \longrightarrow NH_2^+ + H \tag{1.17}$$

$$NH_2^+ + e^- \longrightarrow NH + H \tag{1.18}$$

However, reactions of nitrogen with H_3^+ ions (which have an energy barrier of only 100 K) can occur to some extent, either thermally or via the internal rotational energy of H_2.

1.4.1.5 Sulphur Chemistry Network

The sulphur chemistry network is similar to that of nitrogen, whereby the chemistry network is not initiated by sulphur atoms reacting with a H_3^+ ion. Although this reaction is exothermic, the subsequent reaction of S^+ with H_2 (similar to the nitrogen sequence given in equations 1.16-1.17) is endothermic. Sulphur bearing molecules

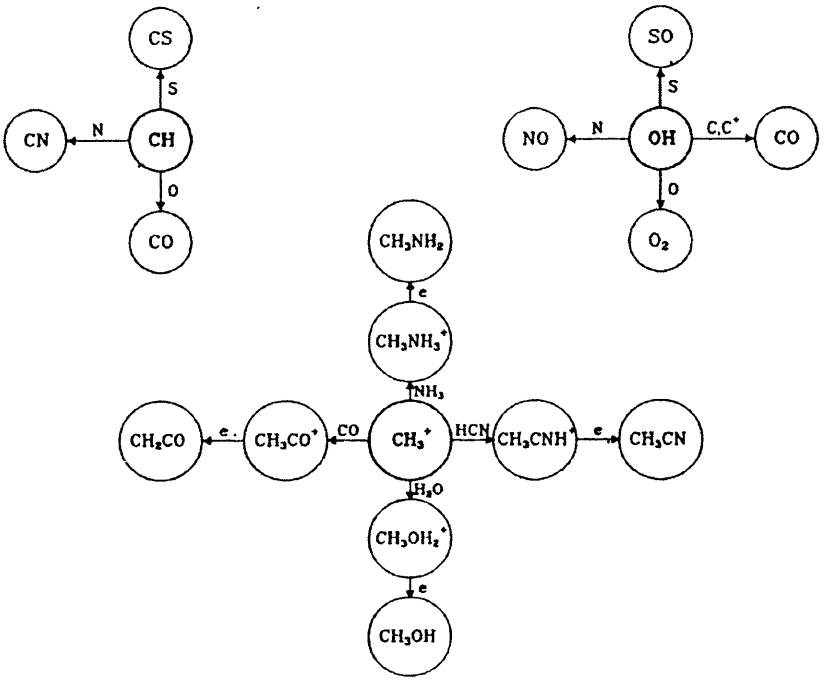

Figure 1.3: Schematic diagram of the important reactions connecting the carbon, oxygen, nitrogen and sulphur chemical networks. Figure taken from van Dishoeck (1998).

are, instead, formed from reactions of atomic and ionic sulphur with oxygen and carbon bearing species to form molecules such as CS and SO (examples are given below).

$$S + CH \longrightarrow CS + H \tag{1.19}$$

$$S + OH \longrightarrow SO + H \tag{1.20}$$

The carbon, oxygen, nitrogen and sulphur chemistry networks are also interconnected. The important connection reactions between C, O, N, and S are depicted in Fig. 1.3.

1.4.2 Initial Conditions

In all the models studied, an initial set of elemental fractional abundances of all atoms is inputted into the model. The initial fractional abundance of each species depends on the physical conditions being studied. For dark clouds, depletion of atoms onto dust grains is taken in account when assuming the elemental fractional abundances. Both sets of conditions are given in Table 1.2. However, Table 1.2 gives representative values for each situation, and the abundances can be set to represent any circumstance.

For instance, in Chapter 4 a warm high pressure interface in a diffuse cloud is being studied with varying intensities of the radiation field, therefore all the carbon is assumed to be initially in the form of C^+ rather than neutral C. Carbon could also be assumed to be partially ionized and partially neutral, or even in the form of CO. In some calculations a more complex set of initial conditions are assumed, where the cloud is taken to be initially molecular, this is known as an initially molecular–rich "soup" (described in more detail in § 3.2).

1.5 Physical Models

The chemical modelling of interstellar clouds, circumstellar regions and interface layers is accomplished using a set of integrated astrochemical codes. The main code calculates the time–dependent fractional abundances of different species, assuming a semi–infinite parcel of gas with a plane parallel approximation. A program called Deload (written originally by Dr. Lida Nejad) writes the ordinary differential equations (ODEs) for all the species and corresponding reactions in the chemical ratefile. The ordinary differential equations are inputted into the main program and using the integrator (GEAR), the time-dependent abundances are calculated.

The physical model uses a chemical network containing 337 species (238 gas–phase) incorporated into a reaction network of 4192 reactions (3865 gas–phase).

Table 1.2: Initial elemental fractional abundances of H, He, C, N, O, S, Mg, Na and Si, appropriate for dark and diffuse clouds.

Species	Dark Cloud	Diffuse Cloud
	Fractional Abundances	Fractional Abundances
H	0.0†	0.4
He	7.0(−02)	7.1(−02)
C	1.0(−04)	3.0(−04)
N	2.0(−05)	2.0(−05)
O	2.0(−04)	6.0(−04)
S	2.0(−08)	3.0(−06)
Mg	3.0(−09)	2.5(−05)
Na	2.0(−07)	1.0(−06)
Si	7.0(−09)	1.0(−06)

Notation a(b) $\equiv$ a $\times$ 10^{b}. † The initial abundance of H is set to zero because all the hydrogen is assumed to be initially molecular.

The ratefile contains species using nine elements, H, He, C, N, O, Na, Mg, Si and S. The original network was taken from the UMIST database (Millar, Farquhar and Willacy, 1997), although it originally only contained gas–phase species, the freeze-out species were added later by Ruffle (1998) (see § 1.5.1).

The ratefile contains reactions of the type:

- •Neutral – Neutral: $X + YZ \rightarrow XY + Z$
- •Ion – Neutral $X^{+} + YZ \rightarrow XY^{+} + Z$
- •Charge – Exchange $X^{+} + YZ \rightarrow X + YZ^{+}$
- •Ion – Ion Neutralization $X^{-} + Y^{+} \rightarrow Z$
- •Dissociative Recombination $XY^{+} + e^{-} \rightarrow X + Y$
- •Radiative Recombination $X^{+} + e^{-} \rightarrow X + h\nu$

- Associative Detachments $X^- + Y \rightarrow XY + e^-$
- Radiative Associations $X + Y \rightarrow XY + h\nu$
- Photoprocesses e.g. $XY + h\nu \rightarrow X + Y$

  $XY + h\nu \rightarrow XY^+ + e^-$

  $X + h\nu \rightarrow X^+ + e^-$
- Cosmic – ray Ionizations $X +$ cosmic–ray proton $\rightarrow X^+ + e^-$
- Cosmic – ray Induced Photoreactions $XY +$ cosmic–ray photon $\rightarrow X + Y$

For each reaction, the rate coefficient, k, can be calculated using one of the following equations (1.21–1.24).

$$k = \alpha \left(\frac{T}{300}\right)^{\beta} exp\left(\frac{-\gamma}{T}\right) \quad (cm^3 s^{-1}), \tag{1.21}$$

for two–body reactions, where T is the gas kinetic temperature and α, β and γ are terms given in the ratefile,

$$k = \alpha \quad (s^{-1}), \tag{1.22}$$

for direct cosmic–ray ionization, where $\alpha = 1.3 \times 10^{-17}$ s^{-1} is the standard interstellar cosmic–ray ionization rate,

$$k = \alpha \, exp(-\gamma \, A_V) \quad (s^{-1}), \tag{1.23}$$

for interstellar photoreactions where α represents the rate in the unshielded interstellar UV radiation field, and γ is the parameter used to take into account the extinction of the UV radiation by dust particles, and

$$k = \frac{\alpha \, \gamma}{(1 - \omega)} \quad s^{-1}, \tag{1.24}$$

for cosmic–ray induced photoreactions, where ω is the grain albedo in the far UV, typically 0.6 at 150 nm, and γ is the probability per cosmic–ray ionization that the appropriate photoreaction occurs.

Table 1.3: Parameters required for the single–point code.

Initial density	n_{H_0}
Final density	n_{H_f}
Temperature	T
Initial elemental fractional abundance	see Table 1.2
Visual magnitude	A_V
Ionization rate	$\zeta^{\dagger}$
Radiation field	in units of $G_0^{\ddagger}$
Freeze–out rate	D
Grain radius	r
Collapse parameter	B

†: $1\ \zeta = 1.3 \times 10^{-17}\mathrm{s}^{-1}$ which is equivalent to the standard interstellar cosmic–ray ionization rate. ‡: 1 G_0 = background interstellar radiation field.

In addition to the chemical ratefile and the corresponding species file, the main code also requires a number of parameters to complete the calculation. These parameters are given in Table 1.3.

1.5.1 Freeze–out Reactions

Freeze–out reactions and simple grain surface hydrogenation reactions were added to the original UMIST ratefile by Ruffle (1998). The freeze–out rate onto dust grains for species X, Γ_X is given by equation 1.25 (Rawlings *et al.*, 1992).

$$\Gamma_{\mathrm{X}} = 1.1 \times 10^{-17}\mathrm{s}^{-1} DA \left(\frac{m_{\mathrm{X}}}{a.m.u.}\right)^{1/2} \left(\frac{T}{1\ \mathrm{K}}\right)^{1/2} \left(\frac{n_{\mathrm{H}}}{1\ \mathrm{cm}^{-3}}\right), \tag{1.25}$$

where D is a parameter which describes the variation in sticking efficiency and the grain size distribution, A is given either by equation 1.26 or 1.27, m_{X} is the mass of one particle of species X and T is the temperature.

$$A = 1 \qquad \text{(for neutral species)} \tag{1.26}$$

$$A = 1 + \left(\frac{167}{T}\right) \qquad \text{(for positive ions)} \tag{1.27}$$

The variation in the A parameter is due to the fact that grains are assumed to be negatively charged. This is because electrons, being lighter than positive ions, move faster and hence will collide more readily with grains. The radius of the grain is assumed to be 0.1 μm and the sticking efficiency assumed in the models ranges from 0.1-1.0.

1.5.2 Static vs. Collapse Models

The main code can be used to calculate the time–dependent fractional abundances of species in an interstellar cloud, which can either be in a static state (pseudo time–dependent) or undergoing collapse (time–dependent). If the cloud is in a static state, then its density is assumed to be constant. Under these conditions, the visual extinction of the cloud, A_V, is also assumed to be constant (typically these values might be $A_V \sim 0$ for a diffuse cloud, 3 for a translucent cloud and 10 for a dark cloud).

If the interstellar cloud is, on the other hand, in a state of collapse, the desired initial and final cloud densities (n_{H_0} and n_{H_f} respectively) are preset and the interim density values increase according to equation 1.28, given by Rawlings *et al.* (1992).

$$\frac{dn_H}{dt} = B\left(\frac{{n_H}^4}{n_{H_0}}\right)^{1/3}\left\{24\pi\, G m_H n_H \left[\left(\frac{n_H}{n_{H_0}}\right)^{1/3} - 1\right]\right\}^{1/2}, \tag{1.28}$$

where B is the collapse parameter ($B = 1$ represents a free–fall collapse and $B < 1$ if magnetic effects and rotational support are assumed to be present), G is the gravitational constant, t is time (where $t = 0$ is time from the onset of collapse) and $m_H = 1$ atomic mass units (a.m.u.).

There will also be a corresponding increase in A_V with density, and hence time for a collapse model. The change in A_V is given by equation 1.29 (Ruffle, 1998).

Table 1.4: Additional parameters required in the multi–point code.

Number and position of depth points
Density variation with depth point
Temperature variation with depth point
Length of column of gas

$$A_V = 0.5 + 2.5 \left(\frac{n_H}{n_{H_0}} \right)^{2/3} \tag{1.29}$$

1.5.3 Single–point vs. Multi–point Calculations

There are two versions of the main code. The first, as described above, is a single–point code calculating the time–dependent fractional abundances of each species. The second code uses an identical chemical ratefile but is a multi–point code. This version is used when considering more complicated astronomical scenarios, such as that discussed in Chapter 6. This multi–point code is more specifically a two–dimensional code, which calculates the time-dependent fractional abundance of each species at different depth points in a column of gas.

The parameter set required for the the multi–point code includes the same as that for the single–point code (as given in Table 1.3) plus the addition of a few others. These are given in Table 1.4.

1.6 Grain Chemical Network

It has been found that a significant fraction of molecular material is present on grain surfaces (van Dishoeck and Blake, 1998), the study of which could provide information on the temperature and levels of irradiation in the region. There are two main processes by which surface molecules are formed. Firstly molecules can form in the gas–phase via reactions described in § 1.4 and subsequently accrete

onto grain surfaces, or they can be formed on grain surfaces themselves via surface reactions. It should be noted that this process will also produce surface molecules which are subsequently desorbed into the gas–phase, either by thermal desorption, non–thermal desorption, or photo–desorption.

Starting initially with the large chemical gas–phase reaction network of Herbst and Leung (1989, 1990), Hasegawa, Herbst and Leung (1992) added a significant number of grain surface reactions involving complex molecules (up to 10 heavy atoms). Their chemical reaction network assumes dust grains with a radius of 1000 Å, a density of 3 gcm^{-3} and 10^6 surface sites for adsorption. The code also assumes the dust and gas temperature to be equal. The sticking probability of all neutral molecules and atoms striking the grain is assumed to be 1, whereas molecular and atomic ions are not assumed to stick to the grain surfaces. The accretion rate of neutral species is given by equation 1.30 (Hasegawa *et al.*, 1992),

$$R_{\rm acc}(i) = \sigma_{\rm d} < v(i) > n(i) n_{\rm d} \tag{1.30}$$

where $n(i)$ is the concentration of species i, $n_{\rm d}$ is the density of dust grains, $< v(i) >$ is its thermal velocity and $\sigma_{\rm d}$ is the geometrical dust cross–section.

Once the gaseous species have been adsorbed onto the grain surface, they 'hop' across the surface, reacting with other species at one of the different surface sites. The timescale of this thermal hopping is given by,

$$t_{\rm hop} = \nu^{-1} exp\,(E_{\rm b} k T_{\rm d}) \tag{1.31}$$

where ν is the characteristic vibration frequency for the adsorbed species, $T_{\rm d}$ is the dust temperature and $E_{\rm b}$ is the potential energy barrier between adjacent surface potential energy wells (i.e. the different surface sites) (Hasegawa *et al.*, 1992). Although it is found that the $E_{\rm b}$ values for most large species is prohibitively large, therefore the majority of surface reactions involve light, atomic and diatomic species.

With their relatively small E_b values, these species can migrate across the grain surface at relatively fast rates.

The time–dependent gas–grain chemistry is calculated by solving coupled (accretion and thermal evaporation) differential equations. The rate equations for species i in the gas phase and on grain surfaces are given by,

$$\frac{dn(i)}{dt} = \sum_l \sum_j K_{lj} n(l) n(j) - n(i) \sum_j K_{ij} n(j) \\ -R_{\rm acc}(i) + t_{\rm evap}(i)^{-1} n_s(i), \tag{1.32}$$

$$\frac{dn_s(i)}{dt} = \sum_l \sum_j k_{lj} n_s(l) n(j) - n_s(i) \sum_j k_{ij} n_s(j) \\ +R_{\rm acc}(i) - t_{\rm evap}(i)^{-1} n_s(i), \tag{1.33}$$

where $n(i)$ and $n_s(i)$ are the concentrations of gas–phase and surface species i respectively, and K and k signify the rates coefficients for the gas–phase and surface reactions respectively.

The gas–grain chemical network of Hasegawa *et al.* (1992) consisted of 156 surface reactions, involving 118 surface species which have been added to the reaction network of Herbst and Leung (1989), which contained 2575 gas–phase reactions with 274 gas–phase species. These models assume rate coefficients where surface reactions are occurring at a relatively fast rate compared to the gas–phase counter–parts. Once a species is adsorbed onto the surface, it moves quickly across the surface and reacts with another species shortly afterwards. Approximate half of the reactions are hydrogenation reactions. More complex molecules, such as hydrocarbons and cyanopolyynes, can be formed with the addition of atomic carbon and nitrogen. There is no activation energy if a hydrocarbon, which is a radical, reacts with a hydrogen atom, whereas a small activation energy exists if the hydrocarbon contains an even number of hydrogen atoms.

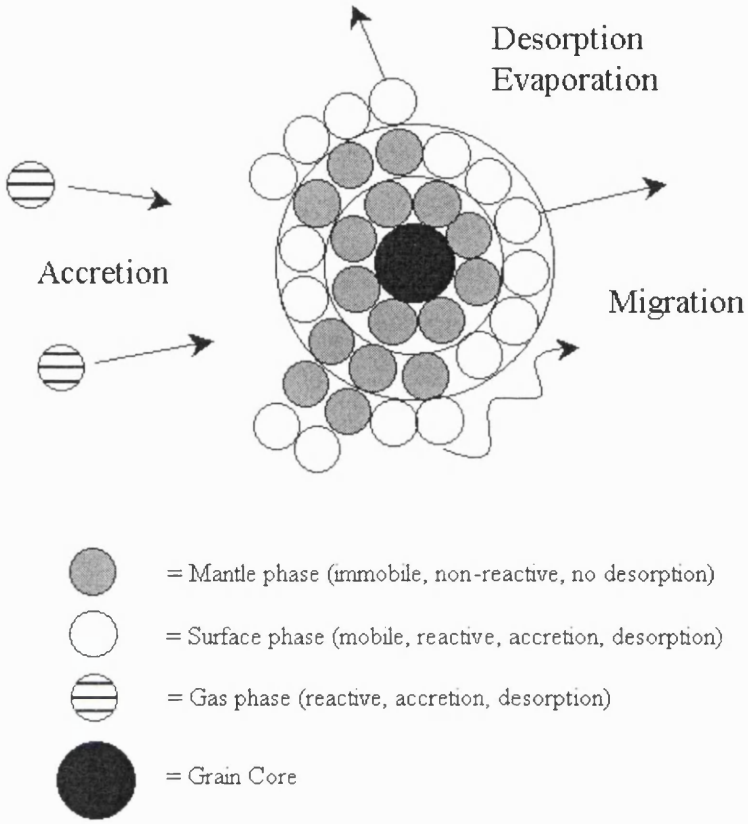

Figure 1.4: Diagram of the three–phase model

The gas–grain chemical network described was modified by Hasegawa and Herbst (1993*a*). Firstly, the model was further improved with the addition of gas–phase and surface chemistry reactions. The sulphur chemical network of Millar and Herbst (1990) was included into the original gas–phase network. The surface reaction network also contained a number of significant additions. These include (i) hydrogenation of hydrocarbons by H_2 reactions, (ii) hydrogenation of other species by H_2 reactions, (iii) reactions involving light radicals, and (iv) reactions from shock chemistry. In all, the modified network now contains 2671 gas–phase reactions, 254 surface reactions and a number of new species. Another significant modification to the model was the addition of a non–thermal desorption term, which was accomplished by the inclusion of cosmic–ray heating of the entire grain.

Further modifications to the the gas–grain model were made by Hasegawa and

Herbst (1993*b*). In the original scenario, a two–phase model was assumed, consisting of the gas and the surface of the grain (a refractory core of the grain is also assumed to exist). All the molecules lie on the grain surface and are available for chemical processing via reactions in the chemical network. However, this two–phase assumption is not realistic, in reality the grain surface is thought to build up to approximately 100 monolayers. The new grain model consists of a refractory core, mantles and the surface layer. The mantle lies below the surface layer and therefore is assumed to be chemically inert. This inert mantle region could now allow a build up of species to occur, which would otherwise be destroyed on the grain surface.

In the modified regime, a three–phase model is assumed, consisting of the gas–phase, grain surface and inert mantle region (depicted in Fig. 1.4). A chemical distinction between the grain surface and mantle is made. The mantle species are now totally unreactive. The rate equations 1.33 and 1.34 were modified to take into account the fraction of material now lying in the inert mantle. The modified differential rate equations are now given by,

$$\begin{aligned}\frac{dn(i)}{dt} &= \sum_l \sum_j K_{lj} n(l) n(j) - n(i) \sum_j K_{ij} n(j) \\ &\quad -k_{\rm acc}(i) n(i) + [k_{\rm evap}(i) + k_{\rm crd}(i)] n_s(i),\end{aligned} \tag{1.34}$$

$$\begin{aligned}\frac{dn_s(i)}{dt} &= \sum_l \sum_j k_{lj} n_s(l) n(j) - n_s(i) \sum_j k_{ij} n_s(j) \\ &\quad +k_{\rm acc}(i) n(i) - [k_{\rm evap}(i) + [k_{\rm crd}(i)] n_s(i),\end{aligned} \tag{1.35}$$

where $n(i)$ and $n_{\rm s}(i)$ are the concentrations of gas–phase and surface species i respectively. A capital K signifies the rates coefficients for the gas–phase and k represents that for the surface reaction rate. Subscript evap and crd represent the thermal evaporation and the cosmic–ray induced desorption terms respectively.

Additional alterations to the model were made after data from Katz *et al.* (1999) were released. Katz *et al.* (1999) made a study of the the activation energy barrier against diffusion, E_b for H and the desorption rates, E_D of H and H_2 for different grain surfaces (olivine and amorphous carbon). They found that the energy barriers were higher than previously assumed in the original models. The diffusion rates of species are dependent on E_b and the desorption rates of species are dependent on the desorption rate E_D, and with the new higher barriers, hydrogen atoms are now thought to diffuse across grain surfaces at a slower rate. They also found that the formation of molecular hydrogen does not occur via the quantum tunneling of a hydrogen atom through the energy barrier to the activation site of the second hydrogen. Instead they proposed that H_2 is formed when hydrogen atoms thermally hop over the thermal heightened energy barriers. The coupling of the need for thermal hopping and the lower diffusion rates leads to an overall decline in hydrogen surface mobility and the slowing down of grain surface chemistry. It should also be noted that the desorption energy for H_2 on olivine is lower than originally assumed.

The new data was incorporated into the three–phase model by Ruffle and Herbst (2000), who altered the diffusion rate of hydrogen to the new, lower values. They produced two new models, the first (labelled M1) with the high energy barriers of hydrogen diffusion taken from Katz *et al.* (1999) for an olivine surface. The second model (labelled M2) contains the the modified hydrogen diffusion rate values and also assumes an increase in energy barriers for other reactive species. The original and modified E_b and E_D values for all modified species are given in Table 1.5.

The final modification to the gas–grain model to date, was made by Ruffle and Herbst (2001*a*). This further modification of the gas–grain model came about because the models M1 and M2 described above, failed to reproduce the observed high abundance of surface CO_2 towards Elias 16 (Gerakines *et al.*, 1999). This discrepancy in CO_2 abundance has been explained by the photodissociation of surface

Table 1.5: Original and modified activation energy barriers and desorption energy (K) for all modified species.

	E_D(i) Value		E_D(i) Value		
Species	Original	M1 and M2	Original	M1	M2
H	350	373	100	200	287
H_2	450	315	135	135	243
He	100	100	30	30	77
C	800	800	240	240	616
N	800	800	240	240	616
O	800	800	240	240	616
S	1100	1100	330	330	847
CH	654	654	196	196	504
NH	604	604	181	181	465
OH	1260	1260	378	378	970

species which are used in the formation of CO_2.

The gas–grain chemical network was therefore expanded to account for photochemistry. Two sources of photons were included in the model, the background interstellar radiation field and the cosmic–ray induced UV field. The cosmic–ray induced UV field is expected to penetrate deep into the interiors of dense cores, whereas the background interstellar radiation field is not expected to be effective at visual magnitudes greater than ~ 7.

The new photochemistry includes photodissociation reactions only, photo– desorption is not modelled. Photoionization is also included but the resultant ion and electrons instantly recombine to form secondary products (the chemistry of which is taken from the gas–phase chemical network). The increase gas–grain chemical network now contains 4218 gas–phase reactions involving 455 species and 1202 surface reactions, involving 196 surface species.

1.7 Aims and Objectives

The aim of this thesis is to identify 'tracers' for the theoretical astrophysical interface layers studied, and to try to explain observational data presently available. These tracers can give detailed information concerning the physical conditions in the environment, and may also help to determine its evolutionary status. Interface layers are especially interesting because they can provide information on a number of different processes and conditions occurring within the interface. This could include the extent of the mixing between the two regions. It may be found that extensive mixing in interface layers is ubiquitous in the interstellar medium and that we should not necessarily consider the different interstellar regions and clouds as separate and distinct entities when constructing theoretical models.

Chapter 2 gives a description of the formation of water ice, in relatively quiescent regions. We study the efficiency of water ice formation under a variety of physical conditions. In Chapter 3 we look at the effects of the mixing of hot ionized gas into the edge of a cold neutral molecular cloud. Chapter 4 concentrates on the turbulent boundary layers of a diffuse cloud, and we consider the effects of the high temperatures and pressures which may be present. In Chapter 5, we simulate x-ray ionization in dark clouds and include the formation of C^{++} to study the effects on the abundance of CH^{+}. Finally in Chapter 6 we consider how, if present, a photon dominated region above a disk could enhance the column densities of molecular species and thereby providing a large number of tracers from which we could observe. Conclusions, and future work to be accomplished are discussed in Chapter 7.

CHAPTER 2

The Water Ice Distribution in Taurus

Observations show that water ice begins to be deposited on grain surfaces at a certain critical depth within molecular clouds, and that its column density beyond that depth rises nearly linearly with visual extinction into the cloud. Our aim is to interpret this behaviour in this transition *interface* where ice is deposited using the gas–grain chemical model described in §1.6, and to determine what constraints such an interpretation places on the physical model of such regions. We find that for higher values of extinction, our models predict that much of the elemental abundance of available oxygen is in the form of ice for evolutionary times greater than about 10^5 yrs., and this leads to the observed near–linear relationship between ice column density and A_V. For lower extinction, our models show that if any significant amount of ice is still present, its existence can be attributed to great cloud age, to our poor understanding of dust grain surfaces, or to cloud clumpiness. The first and third explanations pertain only if photo–desorption of ice is inefficient.

2.1 Introduction

Water ice is the major constituent of grain mantles in dense, cold interstellar clouds (Whittet *et al.*, 1988). It was proposed by Jones and Williams (1984) that ice is synthesised on the surfaces of interstellar grains via the hydrogenation of surface oxygen atoms when hydrogen atoms land on the grain and rapidly diffuse. The detection of water ice via the use of field stars as sources of infra–red radiation, as opposed to internal protostellar sources, has been especially interesting because the cool foreground dust is not contaminated by warm regions surrounding protostellar material. Given the heterogeneity of molecular cloud complexes, a major focus of ice observations has been the determination of the relationship between the ice column density and the visual extinction along various lines of sight through a cloud complex. The two regions studied most closely have been the Taurus and Ophiuchus dark clouds. The former is a rather quiescent region of low mass star formation while the latter is more active because of the presence of nearby hot young stars that enhance the local UV field. Only the Taurus cloud has been studied using background field stars.

Starting with the observations of Harris, Woolf and Rieke (1978) on the ρ Ophiuchus dark cloud and Whittet *et al.* (1983) on the Taurus cloud, a number of observations have indicated a threshold, or critical visual extinction, A_{Vcrit}, for detection of water ice of ~ 3 in Taurus (e.g. Whittet *et al.*, 1988; Smith *et al.*, 1993; Chiar *et al.*, 1995) and ~ 12 in Ophiuchus (Tanaka *et al.*, 1990). The most recent paper on Taurus supporting this point of view is that of Whittet *et al.* (2001), who derived a critical visual extinction of 3.2 ± 0.1. A similar critical extinction has been measured towards the dark cloud R Coronae Australis (Whittet *et al.*, 1996). Two recent studies (Murakawa, Tamura and Nagata, 2000; Teixeira and Emerson, 1999) show, however, less evidence for individual distinct thresholds in Taurus and ρ Ophiuchus. In Taurus, which appears to be the better studied of the two sources, the data of

Murakawa *et al.* (2000), which are solely concerned with field stars as the sources of radiation, show a large scatter in data points at $A_V \leq 3$, with some lines of sight showing detectable ice features. Although these authors suggest that their data can be interpreted in terms of a variable critical threshold of 2-5 for ice detection, it is perhaps simpler to conclude from their data that there is no real threshold at all. Indeed, the data set of Murakawa *et al.* (2000) appears to indicate detectable amounts of water ice at extinctions down to less than unity, but given the significant uncertainty in their relevant data points (see their Fig. 2), as well as difficulties in determining extinctions, it is unclear whether they have indeed detected ice at very low extinction.

What all studies seem to agree upon is that above a certain extinction, there is a clear linear dependence between the ice column density and A_V, at least through an extinction of ~ 14. At higher visual extinctions, there may be a discontinuity in the ice vs. A_V curve if one includes water ice observed towards young stellar objects (YSO's), as was done by Teixeira and Emerson (1999).

The existence of a critical extinction for the detection of water ice has been interpreted in terms of photo–desorption via external or internal ultra–violet and infra–red photons (Adamson *et al.*, 1988; Smith *et al.*, 1993; Williams *et al.*, 1992) in an inhomogeneous medium. This interpretation has been maintained by Murakawa *et al.* (2000) despite their failure to find a single threshold extinction for ice in Taurus. The lack of a single critical A_V has been explained in terms of clumpiness (Murakawa *et al.*, 2000).

Although the destruction of ice doubtlessly plays a role in determining the shape of the ice vs A_V curve, little attention has been paid to the formation efficiency of water ice under differing physical conditions. The need to consider both formation and destruction suggests that a detailed study of the chemistry of water ice be undertaken under conditions ranging from low density and low visual extinction to

high density and high visual extinction. It is conceivable that when ice formation is taken into account, calculated abundances may show that the ice column density–A_V plot is not particularly sensitive to the clumpiness of clouds along the lines of sight.

In this chapter, we report the use of chemical models to investigate water ice abundances over a wide range of physical conditions relevant to the interstellar medium. Our models used, incorporate both gas–phase and diffusive grain surface chemistry. The results we obtain are used to produce theoretical plots of ice column density vs. A_V which are then compared with observations for the well studied Taurus dark cloud. In § 2.2 we describe the models used, in § 2.3 we present the results and finally in § 2.4 we discuss the significance of our findings.

2.2 Model Calculations

The models used contain the gas–grain chemical networks of Ruffle and Herbst (2000, 2001*a*), in which gas–phase and grain surface chemistries are linked through accretion and desorption processes. The networks are based on a diffusive surface chemistry occurring on an olivine–like material. Developed in response to simulations of new experimental data on the surface mobility of hydrogen atoms (Katz *et al.*, 1999), the networks incorporate slower rates of diffusion of species across grain surfaces than assumed previously (e.g. Hasegawa, Herbst and Leung, 1992; Willacy and Millar, 1998). A variety of models have been developed from the chemical networks (refer to § 1.6 for a more detailed physical description of the models). Ruffle and Herbst (2000) make a detailed discussion of two distinct models – M1 and M2; these differ in the adopted surface diffusion rates. In M1, atomic H is the only species with reduced mobility relative to that used in previous models, and the diffusion of H is not fully slowed to the extent measured by Katz *et al.* (1999). In M2, the atomic hydrogen diffusion rate is indeed slowed to the measured value,

while the diffusion rates of all other species are slowed proportionally. In both models, desorption of surface species occurs via thermal evaporation (which returns only the most weakly bound species to the gas–phase at low grain temperatures) and via heating caused by the passage of cosmic–rays through grains (Léger, Jura and Omont, 1985; Hasegawa and Herbst, 1993*a*). For dense quiescent sources, the extent of surface chemistry that occurs in M1 is greater than in M2, where only surface reactions involving atomic H are of any importance.

Ruffle and Herbst (2001*a*) went on to extend models M1 and M2 to incorporate surface photochemistry and were renamed P1 and P2, respectively. Terms were included for both the external background radiation field and the cosmic–ray induced field. The surface photochemistry takes the form of photodissociation, with products remaining on the surface. Differences with the calculated gas–phase and surface abundances of the earlier M1 and M2 models occur only at very long times for dense quiescent sources in molecular clouds.

In this work, we introduce new models which incorporate photo–desorption following the photodissociation of water ice. The cross sections for photodissociation are such that its efficiency per sufficiently energetic photon is approximately 0.01 per monolayer if the monolayer is pure ice. Although photo–desorption via visible photons appears to be very inefficient (Bourdon, Prince and Duley, 1982), there is some evidence for photo–desorption following photodissociation of water ice with UV photons. In particular, Westley *et al.* (1995) found that pure cold ice can undergo photo–desorption at the Lyman α wavelength (122 nm) at efficiencies up to 0.01. Although the efficiency apparently refers to the total of all monolayers of ice up to the penetration depth of 450 Å, Westley *et al.* (1995) assume that most desorption takes place in the outer monolayer. In addition, this efficiency is reached only after the ice is bombarded by a large number of photons. If, as suggested by the authors, the process involves intermediate formation of surface OH radicals via photodisso-

ciation of water followed by photo–desorption of the radicals or their reaction with excited water molecules, then it is likely to be even less efficient in the interstellar medium, where H atoms from the gas can recombine with surface OH radicals prior to their desorption.

The models with limited photo–desorption were discussed in Ruffle and Herbst (2001*a*), for the case where all hydrogen atoms produced via surface photochemistry are ejected into the gas–phase. The results of these models for cold quiescent sources were found to be identical to those in which the atomic H is retained on the surface because H atoms are sufficiently abundant in dense cores that enough atomic H arrives on to the surface to replace atoms ejected. In this chapter, the effect of allowing both H atoms and OH radicals produced via photodissociation of surface water molecules to desorb are investigated. We assume two cases with different ejection efficiencies of H and OH, following photodissociation. The first case assumes a 100 % efficiency in OH desorption following photodissociation, which implies an overall efficiency per energetic photon per monolayer of 0.01. Since the process is allowed to occur for up to 100 monolayers of ice, this efficiency is far higher than the maximum efficiency determined by Westley *et al.* (1995) with Lyman α photons except when only one monolayer of ice is present. The second case assumes only a 30 % efficiency in OH desorption. The versions of the models P1 and P2 that incorporate this photo–desorption mechanism are labelled Z1 and Z2, and the corresponding P2 model with a OH desorption efficiency of 30 % is labelled Z3. In Table 2.1 the five models used in this paper, P1, P2, Z1, Z2 and Z3, are compared.

In the models, grains with radii of 0.1 μ and 10^6 binding sites are assumed. A standard value of the sticking coefficient of 0.5 is assumed. The standard value for the cosmic–ray ionization rate, ζ, of 1.3×10^{-17} s^{-1} is used. As in Ruffle and Herbst (2000, 2001*a*), we use the "low metal" values for the initial elemental abundances, following Lee, Bettens and Herbst (1996), which can be found in Table 2.2. These

Table 2.1: Comparison of models with olivine–like grain surfaces.

Model	H Diffusion	Diffusion of Other Species†	OH Photo–desorption
P1	slow	unaltered	no
P2	very slow	very slow	no
Z1	slow	unaltered	yes
Z2	very slow	very slow	yes
Z3	very slow	very slow	yes (30% efficiency)

†: all species other than H and H_2.

abundances pertain to the sum of the gas–phase and grain–mantle compositions; all the material not incorporated in refractory grains is initially in the gas.

The kinetic equations used for surface diffusion are taken from the modified rate equation approach of Caselli, Hasegawa and Herbst (1998); Shalabiea, Caselli and Herbst (1998); Stantcheva, Caselli and Herbst (2001) although the need for modifications is greatly reduced due to the low diffusion rates employed (equations 1.34-1.35). Recent work (Green *et al.*, 2001) on a full master equation technique for a small system demonstrates that a modified rate equation approach is reasonably accurate for the chosen model conditions.

We have examined the behaviour of water ice over varying physical conditions, including a wide range of realistic interstellar environments from warm, tenuous diffuse clouds, through cooler translucent clumps, and on to dense, cold, dark cores. The assorted densities, $n_{\rm H}$, temperatures, T, and extinctions $A_{\rm V}$ used are given in Table 2.3. The assumed temperatures apply to both the gas and the grains. The initial form of hydrogen is assumed to be either purely atomic or molecular, depending on the density. It should be noted that the use of molecular rather than atomic hydrogen at low $A_{\rm V}$ does not significantly affect our results. The chosen sets of conditions will be referred to hereafter by the value of $A_{\rm V}$.

Table 2.2: Initial elemental fractional abundances.

Element(Initial Form)	Fractional Abundance
H	1.00
He	1.4(−1)
N	2.14(−5)
O	1.76(−4)
C^+	7.3(−5)
S^+	8.0(−8)
Si^+	8.0(−9)
Fe^+	3.0(−9)
Na^+	2.0(−9)
Mg^+	7.0(−9)
P^+	3.0(−9)
Cl^+	4.0(−9)

The notation a(b) implies a $\times$ 10^b.

Table 2.3: Comparison of selected model conditions.

A_V	n_H(cm)	T (K)	L (cm)	Initial Form Of Hydrogen
0.5	1.0(02)	25	8.0(18)	Atomic
1	5.0(02)	20	3.2(18)	Atomic
3	1.0(03)	15	4.8(18)	Atomic
5	5.0(03)	10	1.6(18)	Atomic
10	2.0(04)	10	8.0(17)	Molecular
15	5.0(04)	10	4.8(17)	Molecular
20	1.0(05)	10	3.2(17)	Molecular

The notation a(b) implies a $\times$ 10^b.

To simulate the observed ice column density vs A_V curve, the assumption has been made that the ice abundance along any given line of sight is determined by one major component from those in Table 2.3 with a given length L, also listed in the table, and determined from the simple relation (van Dishoeck 1998),

$$L(\mathrm{cm}) = 1.6 \times 10^{21} \times \left(\frac{A_V}{n_H}\right), \tag{2.1}$$

based originally on diffuse cloud data (Bohlin, Savage and Drake, 1978) but consistent with other sources. All lesser contributions to the ice column density along the line of sight have been ignored. The column density of water ice, $N(H_2O$ ice), is calculated from the relation

$$N(H_2O \text{ ice}) = x(H_2O \text{ ice}) \times n_H \times L, \tag{2.2}$$

where x denotes the fractional abundance of solid water determined in our model calculations. Substituting L from equation 2.1 yields

$$N(H_2O \text{ ice}) = x(H_2O \text{ ice}) \times 1.6 \times 10^{21} \times A_V \ . \tag{2.3}$$

Thus, if x is constant, a plot of the column density of ice vs the visual extinction should be a straight line with slope $x \times 1.6 \times 10^{21}$.

In addition to studying the dependence of the water ice abundance on A_V we also consider the dependence of condensed phase CO on A_V since this has been studied observationally for the Taurus dark cloud, although to nowhere near the extent of the water ice studies.

2.3 Results

2.3.1 Water Ice vs. Extinction

The calculated column density of water ice vs A_V over the range $0.5 \leq A_V \leq 20$ at assorted times is plotted for models P1 and Z1 in Fig. 2.1, for models P2 and Z2 in Fig. 2.2 and for model Z3 in Fig. 2.3. For P1 and P2, values are shown for 10^5 yrs. $(\cdots)$, 10^6 yrs. $(- \cdot -)$ and 10^7 yrs. $(- \cdots -)$, whereas for Z1 and Z2, results are given at only 10^6 yrs. $(- -)$ and 10^7 yrs. (— —) since the results at 10^5 yrs. do not differ from those of P1 and P2. For the Z3 plot, results are given for all three times with 10^5 yrs. depicted as $(\cdots)$ and 10^6 and 10^7 yrs. linestyles are the same as Z1 and Z2. In addition to the calculated results, the observational results for the Taurus dark cloud of Murakawa *et al.* (2000, denoted by diamonds), Whittet *et al.* (2001, denoted by stars), and of Teixeira and Emerson (1999, denoted by squares) are included in the figures. Uncertainties for selected data points of Murakawa *et al.* (2000) are also shown. Data at higher visual extinction are not included. Finally, the solid line in each figure represents the column density obtained if water ice is assumed to have a constant fractional abundance of 1.8×10^{-4} cm^{-3}, the maximum allowable given the abundance of oxygen used, at all values of A_V.

Postponing a detailed discussion of the results at low A_V ($0.5 \leq A_V \leq 6$) until later, we see from the figures that the calculated results at higher A_V show (a) a linear to near–linear relationship between the water column density and A_V for all models and times used, with a slope similar to the observed data, and (b) an increasing water abundance with increasing time, especially for models P1 and P2, in which there is no photo–desorption. Moreover, the observational data are reasonably bracketed by the results of all models at 10^5 yrs., which lie slightly below almost all of the observational points, and all models at 10^6 yrs., which lie either slightly above them (P1 and P2) or above most of them (Z1, Z2 and Z3). These data are consistent with a constant fractional abundance of water ice equal to $\sim 30 - 40\%$

of the oxygen elemental abundance once A_V exceeds 5. Some data at higher visual extinction than shown indicate even higher ice abundances (Teixeira and Emerson, 1999). Since the ordinate is linear, all model results at all times lie within a factor of 2-3 of virtually all the observed ice column densities for $A_V > 5$.

If there is evidence for clumpiness along the line of sight, it is likely to occur at low A_V since small high density clumps with large fractional abundances of water ice will strongly affect the results. In Fig. 2.4, the low A_V results given in Figs. 2.1, 2.2 and 2.3 are expanded. The data of Murakawa *et al.* (2000) indicate that there may be lines–of–sight with A_V as low as 0.5 that show a significant column density ($\sim 10^{17}$ cm^{-2}) of water ice. At these low A_V, the data of Teixeira and Emerson (1999) represent upper limits only. A variety of model results are shown in Fig. 2.4. Since the four models produce similar results at 10^5 yrs., results for only one model (P1) are plotted at this time. Values are displayed for P1 at 10^5 yrs. ($\cdots$), 10^6 yrs. (—) and 10^7 yrs. (—△—), for P2 at 10^6 yrs. (– –) and 10^7 yrs. (— —), for Z1 at 10^6 yrs. (– · –) and 10^7 yrs. (– $\cdots$), and for Z3 at 10^6 yrs. (—×—) and 10^7 yrs. (—$^+$—). Results for Z2 have not been included in Fig. 2.4 as they are very similar to those for Z1.

It is useful for the purpose of comparison between theory and observation to divide the low A_V range into two sub–ranges: 0.5-3 and 3-6. Whether or not water ice has been detected in the former range is controversial (Whittet *et al.*, 2001), while the latter range is above the standard extinction threshold. The A_V = 3-6 range is fit well by the models, which can be considered to represent translucent sources, as long as the time significantly exceeds 10^5 yrs., a rather short dynamical time for all but dense clouds. In this range there is a good correlation between models Z3 at 10^{6-7} yrs. and the observations. Most of the column densities lie between results for models Z1/Z2 at 10^{6-7} yrs. and models P1/P2 at 10^6 yrs. The former models, which include a mechanism for photo–desorption of water ice, contain results which

lie somewhat below the data points, while the latter models contain results that are somewhat above the data. Further fine–tuning of the time for P1/2 or the efficiency of photo–desorption for model Z3 could improve the agreement even more.

The A_V = 0.5-3 range is represented by diffuse to weakly translucent cloud models. These clouds are likely to be dynamically old, and so it is reasonable to consider results at a time in the vicinity of 10^7 yrs. At this time, there is a strong difference between our P1 and P2 model results, on the one hand, and our Z1 and Z2 model results on the other hand. The P1 model results lie near or somewhat below much of the Murakawa *et al.* (2000) data while the P2 model results lie somewhat above most of the data. A somewhat reduced time for P2 and a somewhat longer time for P1 would reproduce the data better. The Z(1-3) models predict very low abundances, because of the photo–desorption mechanism, which is very important for low extinction sources. Thus, the Z(1-3) model results are incompatible with the Murakawa *et al.* (2000) data but strongly support the existence of a critical extinction of ~ 3 (see Fig. 2.4).

Towards the low end of the 0.5-3 extinction range, we cannot reproduce the non–zero Murakawa *et al.* (2000) data with any of our single–point calculations. We simply cannot produce significant amounts of water ice for A_V= 0.5, while for A_V= 1, most of our models predict very low abundances of water at times through 10^7 yrs. The lines of sight with supposedly large ice column densities of almost 10^{17} cm^{-2} imply fractional ice abundances near 5×10^{-5}. This value exceeds that of our most prolific model (P2) for ice production at A_V= 1 by a factor of 5 or so at a time of 10^7 yrs.

If the non–zero ice points at very low extinction are real, it is tempting to conclude that small clumps of high density are the cause although there are other explanations. For example, in models without photo–desorption, the water ice abundances build up as the clouds age; at a time of 10^8 yrs, for example, P2 yields a very

Table 2.4: Column density (cm^{-2}) of H_2O ice for model P2 with A_V = 1, 3, 5 and 10 for sticking coefficients, S, of 0.5 and 1.

Time (yrs.)	$A_V = 1$		$A_V = 3$		$A_V = 5$		$A_V = 10$	
S	0.5	1.0	0.5	1.0	0.5	1.0	0.5	1.0
1(04)	1.5(13)	6.2(13)	7.7(14)	1.5(15)	5.3(15)	1.0(16)	3.7(16)	3.7(16)
3(04)	6.1(13)	2.7(14)	2.4(15)	4.8(15)	1.7(16)	3.3(16)	1.2(17)	1.2(17)
1(05)	1.9(14)	1.1(15)	7.7(15)	1.5(16)	5.1(16)	1.0(17)	3.4(17)	3.4(17)
3(05)	5.4(14)	3.7(15)	2.4(16)	4.8(16)	1.5(17)	2.8(17)	7.8(17)	7.8(17)
1(06)	1.6(15)	1.0(16)	7.2(16)	1.4(17)	3.8(17)	6.4(17)	1.4(18)	1.4(18)
3(06)	5.1(15)	2.7(16)	2.1(17)	3.7(17)	7.8(17)	9.6(17)	1.9(18)	1.9(18)
1(07)	1.6(16)	6.6(16)	5.3(17)	7.2(17)	1.1(18)	1.2(18)	2.2(18)	2.2(18)
3(07)	4.8(16)	1.3(17)	8.2(17)	8.6(17)	1.3(18)	1.4(18)	2.7(18)	2.7(18)
1(08)	1.3(17)	1.6(17)	8.6(17)	8.6(17)	1.4(18)	1.4(18)	2.7(18)	2.7(18)

The notation a(b) implies a $\times$ 10^b.

large column density of 1.3×10^{17} cm^{-2} at $A_V = 1$. The formation of water ice, though inefficient, is inexorable in models without photo–desorption, as long as A_V is not less than unity. The age needed for development of a significant amount of ice can be reduced considerably if we increase the sticking coefficient S for gas–phase species striking grains from 0.5 to unity. In Table 2.4, calculated column densities for ice using model P2 are tabulated for times through 10^8 yrs and A_V= 1, 3, 5, 10 for S = 0.5 and 1. In particular, at a time of 10^7 yrs, the use of S = 1 in model P2 leads to a column density of 6.6×10^{16} cm^{-2} at A_V=1, in good agreement with the high–ice, low extinction Murakawa *et al.* (2000) data. Other explanations for the possibly non–zero ice points at very low extinction are given in §2.4.

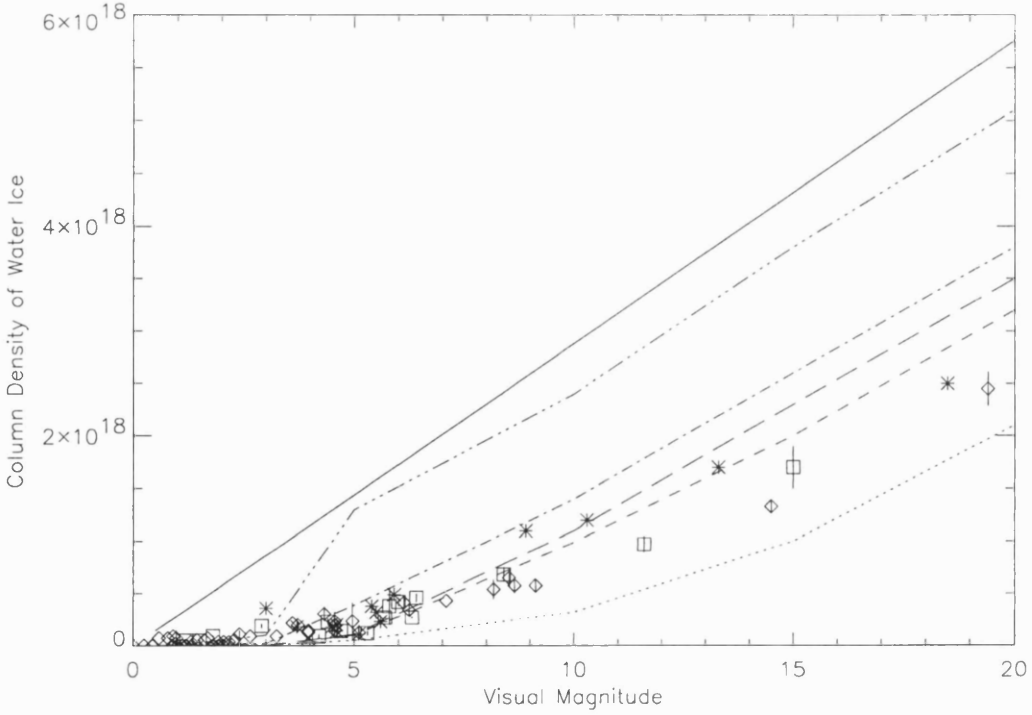

Figure 2.1: Calculated and observed column densities of water ice as a function of A_V over the range $0 \leq A_V \leq 20$ for Taurus. Results for model P1 are given at three times: $\cdots$ denotes 10^5 yrs., $- - -$ depicts 10^6 yrs. and $- \cdots -$ represents 10^7 yrs. Results for model Z1 are given at two times: $- - -$ depicts 10^6 yrs. whilst — — denotes 10^7 yrs. Diamonds represent the observations of Murakawa *et al.* (2000), stars represent those of Whittet *et al.* (2001) and squares those of Teixeira and Emerson (1999).

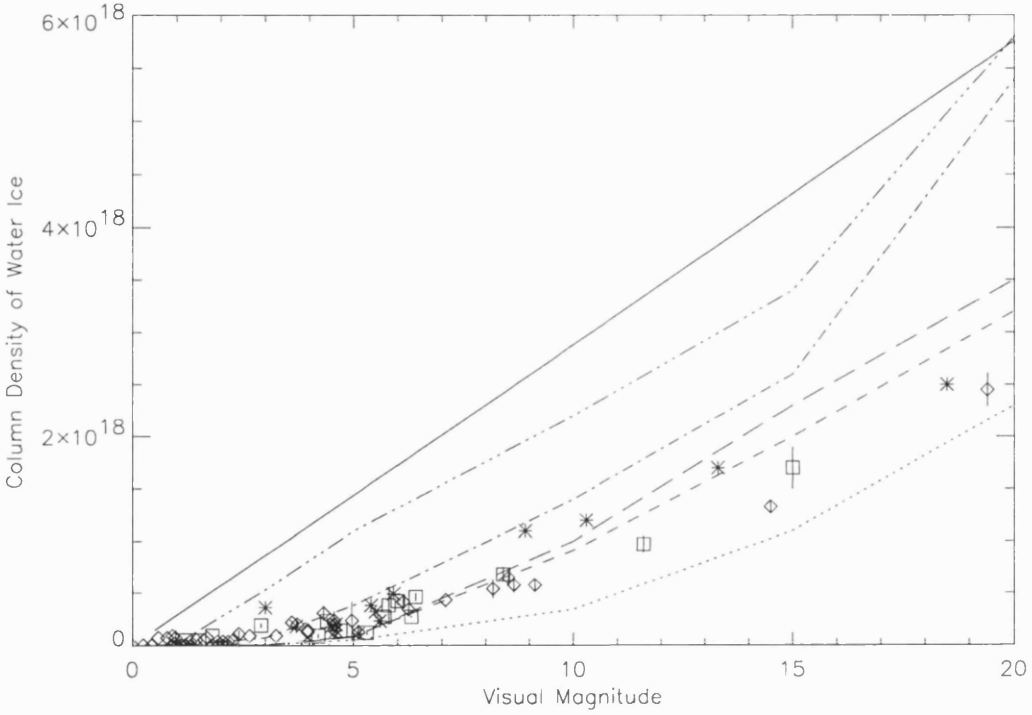

Figure 2.2: Calculated and observed column densities of water ice as a function of A_V over the range $0 \leq A_V \leq 20$ for Taurus. Results for model P2 are given at three times: $\cdots$ denotes 10^5 yrs., $- - -$ depicts 10^6 yrs. and $- \cdots -$ represents 10^7 yrs. Results for model Z2 are given at two times: $- - -$ depicts 10^6 yrs. whilst — — denotes 10^7 yrs. Diamonds represent the observations of Murakawa *et al.* (2000), stars represent those of Whittet *et al.* (2001) and squares those of Teixeira and Emerson (1999).

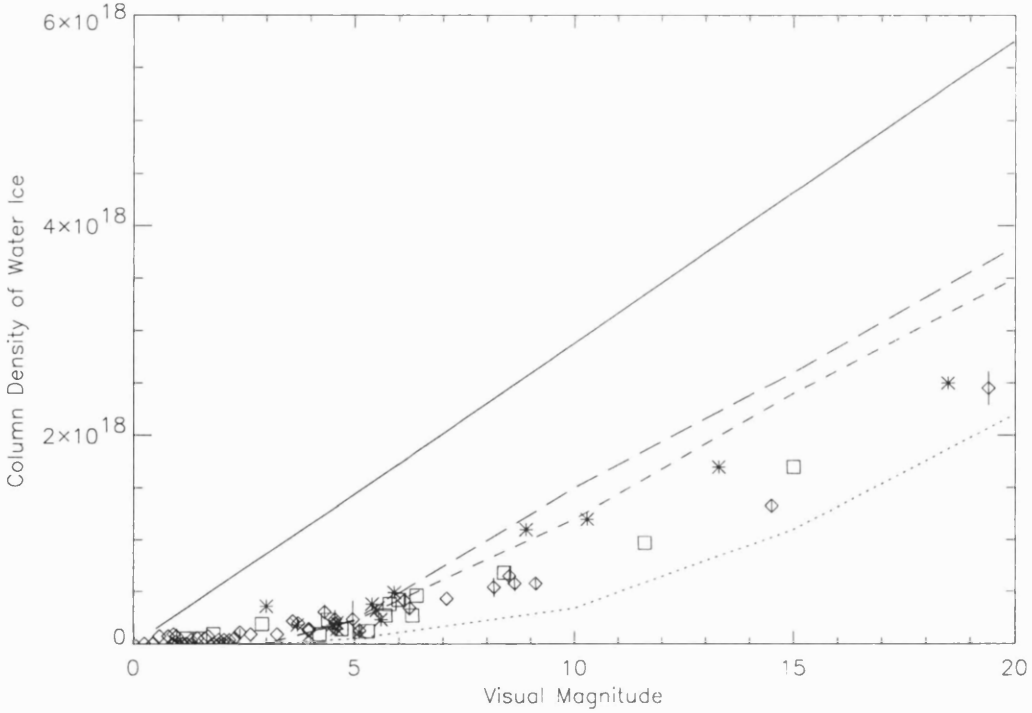

Figure 2.3: Calculated and observed column densities of water ice as a function of A_V over the range $0 \leq A_V \leq 20$ for Taurus. Results for model Z3 are given at three times: $\cdots$ denotes 10^5 yrs., $- - -$ depicts 10^6 yrs. whilst — — denotes 10^7 yrs.. Diamonds represent the observations of Murakawa *et al.* (2000), stars represent those of Whittet *et al.* (2001) and squares those of Teixeira and Emerson (1999).

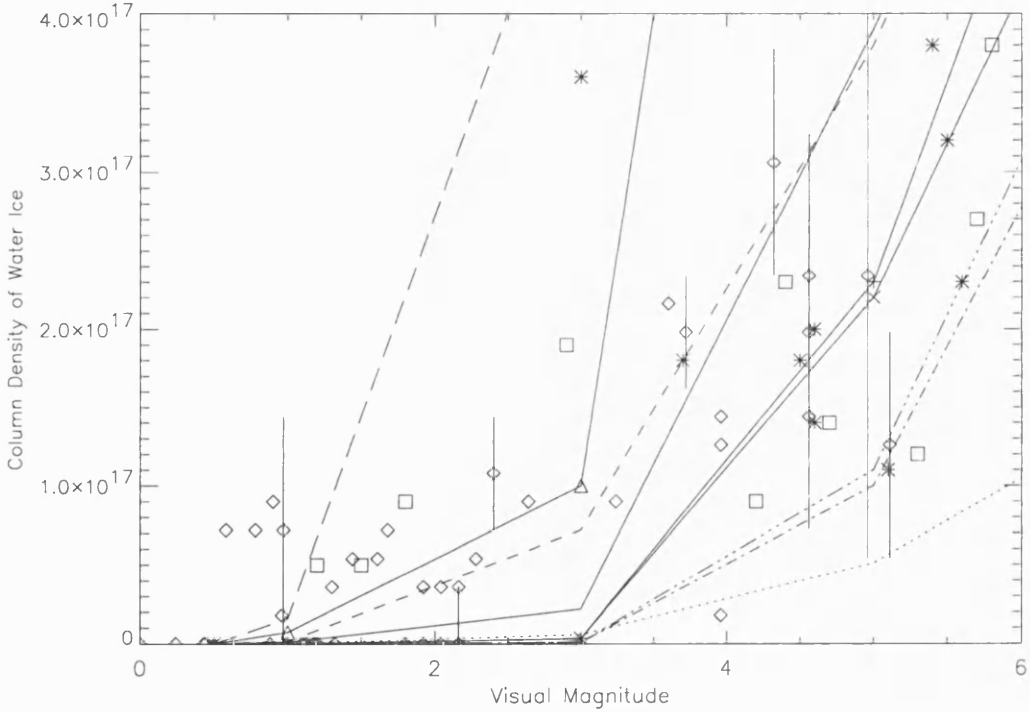

Figure 2.4: Calculated and observed column densities of water ice as a function of A_V over the limited range $0 \leq A_V \leq 6$ for Taurus. For model P1, $\cdots$ denotes 10^5 yrs., — depicts 10^6 yrs. and —△— represents 10^7 yrs. For P2, - - - depicts 10^6 yrs. whilst — — denotes 10^7 yrs. For Z1, 10^6 yrs. is represented by - · - and - $\cdots$ represents 10^7 yrs. For Z3, 10^6 yrs. is represented by —×— and —$^+$— represents 10^7 yrs. The observed values are once more represented by diamonds (Murakawa *et al.*, 2000), stars (Whittet *et al.*, 2001) and squares (Teixeira and Emerson, 1999).

2.3.2 Condensed Phase CO vs. Extinction

Teixeira and Emerson (1999) have studied the dependence of the condensed phase CO column density on A_V in Taurus. Their data (represented by squares) are compared with our results for models P1 and Z1 in Fig. 2.5. The results for models P2, Z2 and Z3 are not significantly different from that of P1 and Z1 and therefore have not been depicted. It can be seen that CO ice appears to become detectable at $A_V = 3$, and that its column density gradually increases with increasing A_V, albeit with much scatter. Our model results generally agree with the observational data. In Fig. 2.5, we use the same symbols for model and time as in Fig. 2.1. Since the models produce similar results at 10^5 yrs., once again only one model is plotted at this time. The 10^6 yrs. line for model Z1 has also been removed as it is very similar to model P1.

Unlike ice, condensed phase CO cannot be a chronometer for any models, since its abundance does not build up on grains inexorably. It is produced in the gas phase and condenses onto grain mantles, where it can react slowly to produce species such as formaldehyde and methanol (Ruffle and Herbst, 2000).

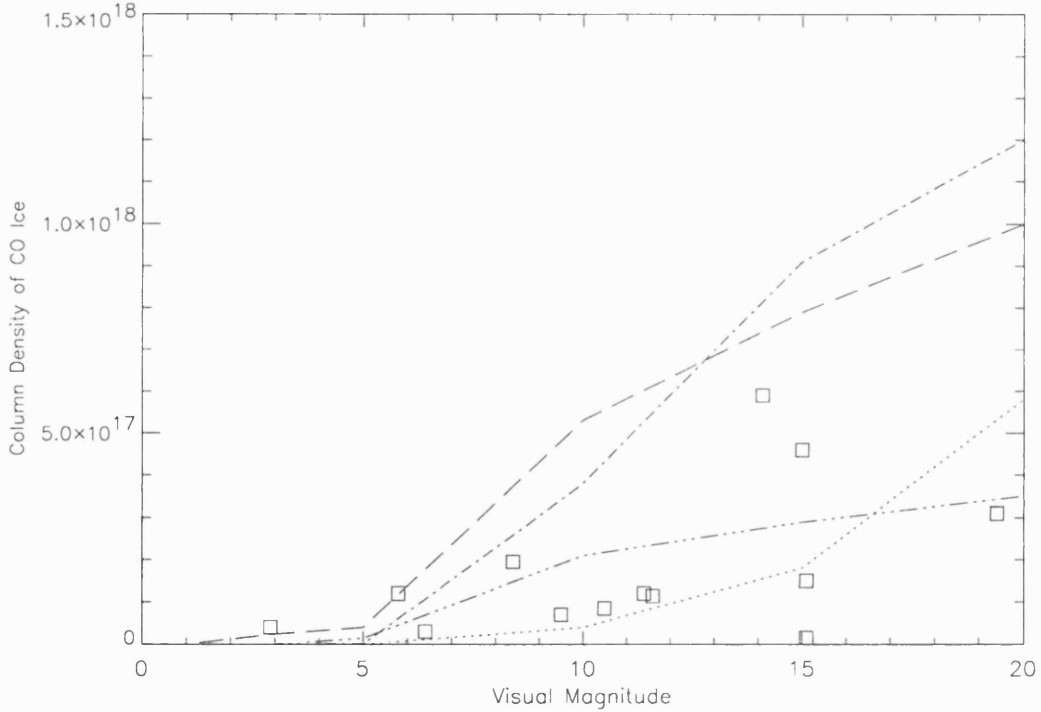

Figure 2.5: Calculated and observed column densities of condensed phase CO as a function of A_V over the range $0 \leq A_V \leq 20$ for Taurus. Results for model P1 are given at three times: $\cdots$ denotes 10^5 yrs, $- \cdot -$ depicts 10^6 yrs and $- \cdots -$ represents 10^7 yrs. Results for model Z1, denoted by — —, are given for 10^7 yrs. only. The squares represent the data of Teixeira & Emerson (1999).

2.4 Discussion

With our current gas–grain chemical models, we have attempted to simulate the relationship between the water ice column density and visual extinction seen in the direction of the Taurus dark cloud. According to the most recent observations (Whittet *et al.*, 2001; Murakawa *et al.*, 2000; Teixeira and Emerson, 1999), there is a linear relationship between the two quantities which extends down from $A_V = 20$ to rather low extinction, at which point there may be a critical extinction of $A_V \sim 3$, below which there is no water ice (Whittet *et al.*, 2001), or there may be lines of sight with little extinction that do show a considerable amount of ice (Murakawa *et al.*, 2000).

Assorted models were run for sources with different but fixed conditions, ranging from diffuse to dense, and characterised by assumed values of gas densities, temperatures, and A_V. The model results are concentrations of gas–phase and condensed–phase species as a function of time, from which column densities can be estimated. The ice column density along any line of sight in Taurus was assumed to be determined by one dominant type of source, as listed in Table 2.3, which means that the possibility of several important clumps along a line of sight was not taken into account.

The model results can explain most and possibly all of the observed relationship between ice column density and A_V without additional assumptions. For the higher values of visual extinction ($A_V \gtrsim 6$), the models predict that much of the elemental abundance of oxygen is in the form of water ice at times after 10^5 yrs. This leads to linear or near–linear relationships between ice column density and A_V. For the models without photo–desorption of water, the ice abundance builds up with time, while for those models with photo–desorption, the build–up is much less dramatic. There is no single time of perfect agreement over the whole range of A_V which is expected since the denser objects doubtless have shorter dynamical lifetimes. For

$A_V \gtrsim 6$, the data are fit best by assorted models at times between 10^5 and 10^6 yrs., while for somewhat lower A_V in the range 3-6, the data are fit well by models with longer lifetimes, depending specifically on whether photo–desorption is included.

For the range A_V = 0.5-3, observational data differ as to whether or not water ice can be detected. Within the constraints of our olivine–based models and single source conditions along any given line of sight, the major variable that can lead to the production of water ice under conditions of low extinction is the lifetime of the source since water ice builds up inexorably in models (P1 and P2) without photo–desorption. Simply put, objects with high ice abundance and low extinction have remained cold for very long periods of time. The actual ages needed are sensitive to the sticking efficiency employed. This explanation is only useful for models without photo–desorption. Models with efficient photo–desorption, on the other hand, show little water ice development at any time in this range of extinction, and are thus in agreement with a critical value for extinction (Whittet *et al.*, 2001).

A second explanation for the possibility of ice at low extinction is the diversity of grain surfaces, because the formation of water ice can have different rates on surfaces other than olivine. Ruffle and Herbst (2001*b*) have recently developed a model that includes diffusive chemistry on amorphous carbon. On this surface, adsorbates bind more strongly than on olivine, and evaporation is less efficient at diffuse cloud temperatures. Consequently, the formation of water is also more efficient. For example, model results show an appreciable build up of water ice for A_V= 1 by 3×10^6 yrs. As another example, current calculations show that surface chemistry on graphite may occur up to much higher temperatures than on amorphous carbon via a non–diffusive mechanism known as the Eley–Rideal process (Meijer *et al.*, 2001). It must also be remembered that once a monolayer of ice is formed (corresponding to a column density of 1.6×10^{15} cm^{-2} at A_V=1), the characteristics of the original surface will change appreciably and begin to resemble those of amorphous ice. Although a

recent experimental study of H atom diffusion on amorphous ice shows that molecular hydrogen can be formed on such a surface at low temperature (Manicò *et al.*, 2001), detailed parameters for the motion, which would allow us to model surface chemistry on ice, were not determined. From theoretical work on H diffusion on amorphous ice (Takahashi and Williams, 2000), it appears that the parameters for diffusive motion (desorption energy, barrier against diffusion), although likely to have a range of values on this complex surface, more closely resemble those used in our model for amorphous carbon than those used for olivine. Thus, if a monolayer of ice can be formed under the harsh conditions of diffuse clouds on a surface such as amorphous carbon, the initial monolayer may "catalyse" the subsequent formation of further monolayers.

A third explanation, discussed in some detail by Murakawa *et al.* (2000), is that any ice at low A_V is caused by clumpiness along the line of sight, which is to be expected given the degree of inhomogeneity perpendicular to this direction. To fully explore this explanation requires a much more complex series of model calculations than presented here, with a detailed treatment of radiative transfer. Nevertheless, one can use the following argument to gauge this possibility. In our current calculations, an extinction of 1 is interpreted in terms of a diffuse cloud. Alternative interpretations (taken from Table 2.3) could be (a) two clumps at density 5×10^3 cm^{-3} and length 1.6×10^{17} cm or 1 clump at density 2×10^4 cm^{-3} and length 8.0×10^{16} cm. For model P2, we obtain a total ice column density of 3×10^{17} cm^{-2} for both alternative scenarios at 10^7 yrs., far in excess of the value of 1.6×10^{16} cm^{-2} obtained for the diffuse cloud case. It is perhaps more reasonable to consider smaller ages for the clumps. If we consider an age of 3×10^5 yrs., the enhancement is more modest but still noticeable, with total computed ice column densities of 3×10^{16} cm^{-2} for the two–clump case and 8×10^{16} cm^{-2} for the one–clump case. For the model Z2, which contains ice photo–desorption via photodissociation, the clump

enhancement is greater although the initial diffuse cloud value is much smaller. At an age of 1×10^7 yrs., the computed A_V =1 ice column density in the diffuse cloud case is a very low 1×10^{10} cm^{-2}; while the column densities for the two–clump and one–clump cases are 5×10^{13} cm^{-2} and 2×10^{14} cm^{-2}, respectively, at all times after 10^4 yrs. These enhanced values are still well below the high–ice data points of Murakawa *et al.* (2000) at very low extinction. It appears then that altered model results incorporating cloud clumpiness are consistent or inconsistent with the high ice, low extinction data points of Murakawa *et al.* (2000) depending upon whether or not photo–desorption of ice is not or is efficient.

2.5 Conclusions

To understand the dependence of the ice column density on A_V in more detail and to understand what it tells us about the Taurus dark cloud, we have run gas–grain chemical models under a variety of physical conditions. We have included the photo–desorption of OH from grain surfaces, once it is formed from the photodissociation of water. For high extinction, our models predict that much of the elemental abundance of available oxygen is in the form of ice for evolutionary times greater than about 10^5 yrs., and this leads to the observed near–linear relationship between ice column density and A_V. For lower extinction, we find that if photo–desorption of water via photodissociation is inefficient under interstellar conditions, we can possibly account for relatively large abundances of water ice at $A_V \leq 3$ by great age, possibly by surface chemistry on initial surfaces other than olivine, followed by formation on ice itself, and by small dense clumps of material along the line of sight. If, on the other hand, photo–desorption of ice is efficient, the first and third explanations, discussed above, do not appear to help sufficiently, leaving only the second as a possibility. Absent this possibility, our results from the Z1, Z2 and Z3 models are in close accord with the view that below a critical extinction of $\sim$ 3 no ice exists. These models with

efficient photo–desorption are partially supported by the photo–desorption studies of Westley *et al.* (1995) when not too many monolayers of ice are present. It is clear though that a full understanding of the proper low–extinction ice vs A_V relation in Taurus and other sources will require an improvement in our understanding of surface chemistry, especially on amorphous ice, and of photo–desorption on a variety of surfaces.

CHAPTER 3

Bistability and Temperature Effects in Mixing Regions

Cool neutral molecular clouds exist as discrete entities. They are embedded in a background gas, whose properties are not well understood. Yet, the background gas may affect the formation and evolution of molecular clouds. Here, we assume that the cloud is embedded in ionized gas, and we consider processes in the *interface* between the two media. We propose a simple method of assessing the chemical consequences of mixing at interfaces between cool neutral gas with ionized material. It is shown that the temperature within the interface has a significant effect; at low temperatures ($\backsim$ 10 K) the chemistry is significantly suppressed, but for temperatures above 100 K the chemistry initiated by proton/O–atom charge exchange gives rise to a rich and abundant chemistry. The chemical state of the cool neutral gas has an important consequence for the interface. A mainly molecular cool gas can give rise to a high ionization state in the interface; this high ionization state appears stable against parameter variations. C_2H is one of the most easily observed molecules having a high abundance in some interfaces.

3.1 Introduction

An interface layer between cold molecular gas and warm ionized gas can occur in a variety of astronomical situations. Tracers of the conditions in these interface layers have been identified in several papers (Charnley *et al.*, 1990; Duley *et al.*, 1992; Nejad and Hartquist, 1994; Taylor and Raga, 1995; Rawlings and Hartquist, 1997). Charnley *et al.* (1990) studied the mixing of cool clump gas which are embedded in star forming regions with stellar wind plasma and found that CH is a good tracer of such clump–diffuse medium interfaces. They also stated that the abundances of C and C^+ increased in models with high mixing rates. Duley *et al.* (1992) state that the large observed column densities of CH^+ could be due to its formation in cloud–intercloud interfaces. Nejad and Hartquist (1994) extended the work of Charnley *et al.* (1990) by including the effects of magnetic pressure on the interface layer. The authors found that CH, OH and H_2O are enhanced with the presence of heating in the boundary layer. They also found that the fractional abundances of C_2, C_2H, CN and HCN are also sensitive to the presence of mixing and heating. Taylor and Raga (1995) made a study of the turbulent boundary layer between a high velocity atomic wind and a stationary, molecular region and found that in this mixing layer, the temperature becomes very hot ($T > 10^4$ K) and therefore the layer becomes chemically active. Rawlings and Hartquist (1997) examined the boundary layer between dark cores and warm, shocked T–Tauri winds and found that C^+, CH, OH and CO are good tracers of this layer. Identification of these species in a particular interface should allow an inference of the extent of dynamical mixing or diffusion occurring in the region. Tracers that have been identified are generally molecular, and the chemistry that gives rise to these species is driven by the enhanced ionization injected into the interface region.

Chemical models of such mixing regions are in principle rather complex. They require a coupling of chemical codes with a mathematical description of the assumed

mixing process. Such codes can be time consuming and difficult to run. In this chapter we present a new and simple method of identifying potential chemical tracers of mixing zones.

The chemistry in interstellar clouds is largely energized by the cosmic ray ionization of H_2 and He,

$$H_2 \xrightarrow{c.r.} H^+ + H + e^- \quad 1.60\% \tag{3.1}$$

$$H_2^+ + e^- \quad 88.90\% \tag{3.2}$$

$$H + H \quad 9.60\% \tag{3.3}$$

$$H^- + H^+ + e^- \quad 0.03\% \tag{3.4}$$

where the total ionization rate in the interstellar medium has the canonical value of 1.3×10^{-17} s^{-1}, and

$$He \xrightarrow{c.r.} He^+ + e^- \tag{3.5}$$

Complex reactions are mainly initiated by proton donation from H_3^+, which is formed rapidly in reactions of H_2^+ with H_2, and recombination of these protonated molecular ions gives rise to various neutrals. For example, OH and H_2O may be formed in the following sequence of reactions:

$$O \xrightarrow{H_3^+} OH^+ \xrightarrow{H_2} H_2O^+ \xrightarrow{H_2} H_3O^+ \xrightarrow{e} OH, H_2O \tag{3.6}$$

Reactions of neutrals with He^+ create ions from neutral species, and these ions may also feed the chemistry; e.g.

$$OH \xrightarrow{He^+} O^+ \xrightarrow{H_2} OH^+ - - - . \tag{3.7}$$

By contrast, protons are much less important in driving chemistry in a mainly neutral gas. Charge exchange of protons with H_2 is endothermic by 1.8 eV, and

this energy barrier is not reached under cold cloud conditions. Accidentally near–resonance charge exchange between protons and O atoms has an energy deficit of 232 K and therefore this reaction is suppressed unless the temperature rises to $\gtrsim$ 100 K. Charge exchange of protons with other available interstellar species is very slow.

In most of the studies of chemistry in interfaces listed above, the injection of ions into the mixing layer gives rise to the interface tracers. However, if the ions are mainly protons, then the molecular cloud may suffer a reduction of chemical complexity. The effect of an injection of ions into the mixing layer will be discussed in this chapter. The different model calculations are described in § 3.2, the results and discussions are given in § 3.3 and conclusions are made in § 3.4.

3.2 Model Calculations

We have explored the chemical effects of mixing by artificially manipulating the branching ratios of reactions 3.1-3.4. The standard branching ratio consists of 88.9 % of H_2 ionising to form H_2^+, while only 1.6 % forming H^+, but if the rate of the H_2^+ formation channel is reduced while that of the H^+ channel is increased, then we may regard this as representing the chemistry in an interface layer in which ionized atomic gas is injected into molecular gas. We illustrate the effects of such changes in a few simple single–point calculations in which the molecular gas is taken to be cool (10 K) and dense ($n_H = 10^4$ cm^{-3}). A modest temperature rise may occur as the ionized gas is injected, and this rise can be included in the models. As an example of the utility of this approach, we run a grid of models to explore the effects of a range of ionization rates of (1ζ-100ζ, where $\zeta = 1.3 \times 10^{-17}$ s^{-1} $\equiv$ the canonical interstellar value).

The chemistry used in this chapter consists of 2950 reactions relating to 238 gas phase species taken from the UMIST database (as described in §1.4. The effects of

Table 3.1: Parameter set for each model.

Model	T (K)	Production Rate of Chemical Composition			Ionization
		H^+	H_2^+	at t=0	Rate, ζ (s^{-1})
A	10	1.63 %	88.75 %	atomic	1, 100
B	10	88.75 %	1.63 %	atomic	1, 100
C	10	88.75 %	1.63 %	molecular	1, 100
D	10	88.75 %	0 %	atomic	1, 100
E	100	88.75 %	1.63 %	atomic	1, 100

freeze–out on to grain surfaces have been excluded, so we have implicitly assumed that desorption is effective. There is some evidence that this may be the case (Willacy and Williams, 1993; Howe *et al.*, 1996; Taylor *et al.*, 1996). The clouds are assumed to be dark therefore the initial chemical conditions set for all models, except Model C, are equivalent to those of a dark cloud (see Table 1.2 for elemental abundances). The number density of H nuclei is taken to be 10^4 cm^{-3} and the visual extinction A_V, is assumed to be 10. Each model is run using both the standard cosmic ray ionization rate and 100 times the standard rate.

For Model C a more complex set of initial conditions is adopted. Instead of assuming an initial simple set of atomic species consisting of H, He, C, N, O, S, Mg, Na and Si, a molecular rich set of all 238 gas phase species is used. This is the first time that such an extensive chemistry has been used in an investigation of interfaces, and its adoption was facilitated by the simple approach employed to treat mixing. The molecular set of conditions is generated by making an initial calculation of a cloud of same density, temperature and A_V, and running the model until a steady–state is reached. The steady–state fractional abundances are then inputted into the new models, described above, as the initial cloud composition.

The model types explored in these calculations are listed in Table 3.1 in which

the assumed production rates of H^+ and H_2^+ for equations 3.1 and 3.3 are given. Table 3.1 also gives the values for the cloud temperature, initial chemical composition and assumed ionization rates. In summary, Model A is the reference standard model, while in the other models the H^+ and H_2^+ branching ratios are modified. Models C explore the consequences of an initially molecular rich assumption, Models D test the effect of switching off H_2^+ production entirely (reaction branch 3.3), and Models E examine the effects of a temperature increase, due to the injection of hot, ionized gas in the mixing zone.

3.3 Results and Discussion

Selected results are shown in Figs. 3.1 and 3.2 for Models A and B for an ionization rate of 1ζ and 100ζ respectively. It can be seen in Fig. 3.1 that, while CO is unaffected by the switch in branching ratios, C, C^+ and CH should be good tracers of mixing, each being enhanced in Model B by over one order of magnitude. This increase in the abundances of C, C^+ and CH has a counter productive effect on the abundances of species such as C_3H_2 and HCO^+. From Models A to B the abundance of C_3H_2 decreases by over two orders of magnitude. This is due to the low abundance of H_3^+, which is a direct consequence of the low formation rate of H_2^+. The H_3^+ ion is used to initiate more complex chemistry networks, including the carbon chemistry in dark clouds via the reactions,

$$C + H_3^+ \longrightarrow CH^+ \longrightarrow CH_2^+ \longrightarrow - - - \tag{3.8}$$

The initiation of the carbon chemistry is also depicted in Fig. 1.1.

A more noticeable decrease can be seen in HCO^+ which can be attributed to the low production rate of H_3^+, which is required for the main formation path of HCO^+, given by the reaction,

$$H_3^+ + CO \longrightarrow HCO^+ + H. \tag{3.9}$$

When comparing Models A and B at the higher ionization rate of 100ζ (see Fig. 3.2), it can be seen that, although there is still an enhancement in abundance of C, C^+ and CH from the standard model, there is now little difference between Models A and B. This is due to presence of such a high ionization rate. The high ionization rate photodissociates species such as CO into C and O, and these atoms are then ionized by the increase abundance of He^+ (the abundance of which follows the cosmic–ray rate). The large decrease in abundance of C_3H_2 and HCO^+ is still seen.

When the ionization rate is enhanced in Models A and B, the general effect is a reduction of molecular abundances in the mixing zone. This occurs mainly because of the destructive effects of He^+. This can more clearly seen in Figs. 3.3 and 3.4. Fig. 3.3 depicts the results for Models A with an ionization rate of 1ζ and 100ζ and Fig. 3.4 depicts the results of varying ionization rates for Models B.

Thus, for Model A (Fig. 3.3), CO is reduced by two orders of magnitude, CH is, however, enhanced by the C^+ released from CO by the reaction,

$$He^+ + CO \longrightarrow C^+ + O, \tag{3.10}$$

while other hydrocarbons remain at about the same level. For Model B (Fig. 3.4), the decrease in abundance of CO, HCO^+ and C_3H_2 is further depressed, as the H_3^+ route is an important contributor to their production.

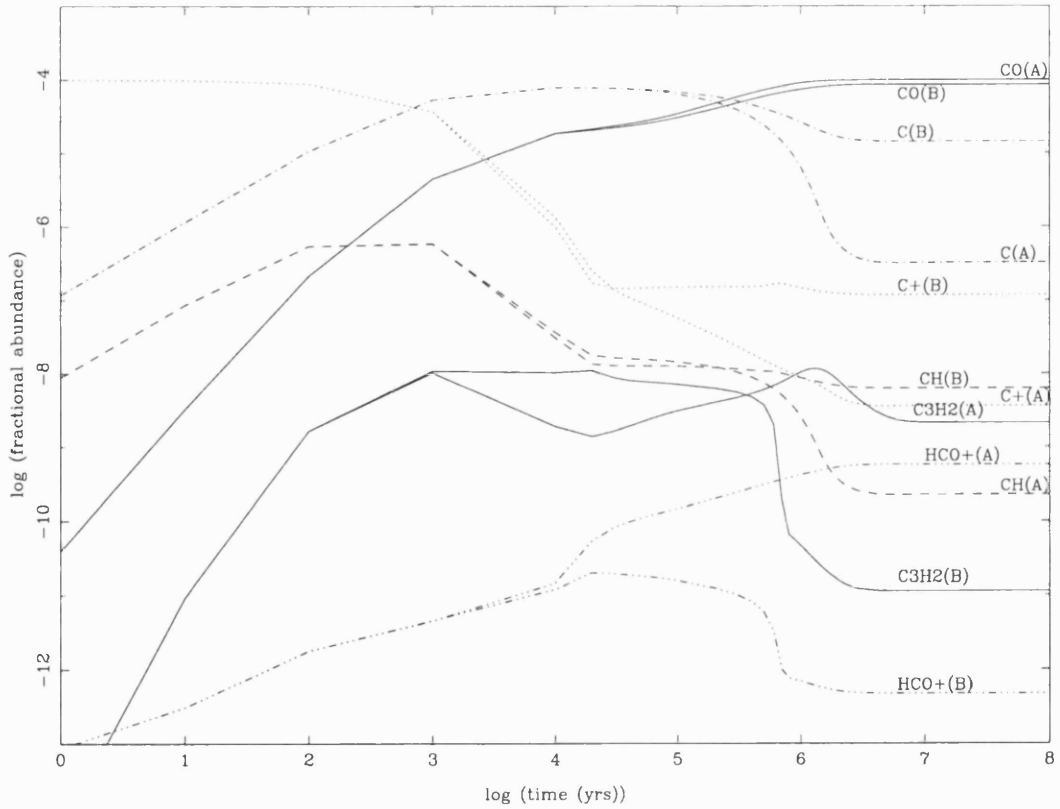

Figure 3.1: Fractional abundance results for selected species for Models A and B for an ionization rate of 1ζ (s^{-1}). CO and C_3H_2 are depicted by —, – · – represents C, ··· denotes C^+, – – – depicts CH and – · · · – represents HCO^+.

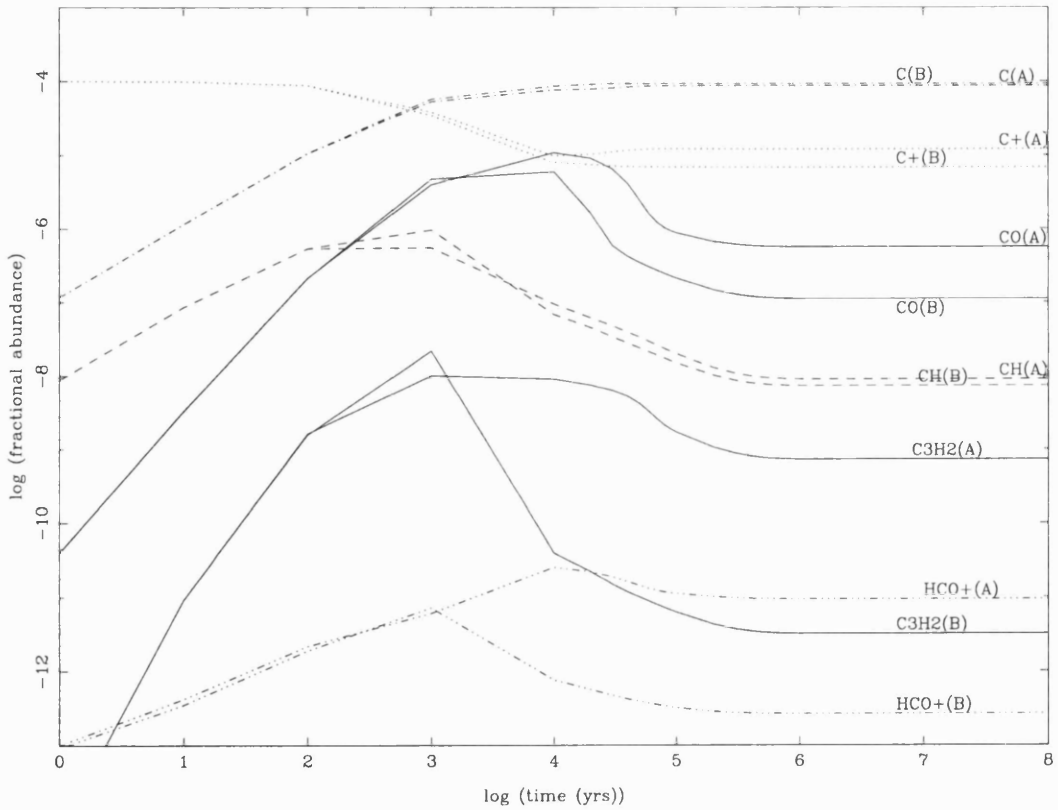

Figure 3.2: Fractional abundance results for selected species for Models A and B for an ionization rate of 100ζ (s^{-1}). CO and C_3H_2 are depicted by —, – · – represents C, · · · denotes C^+, – – – depicts CH and – · · · – represents HCO^+.

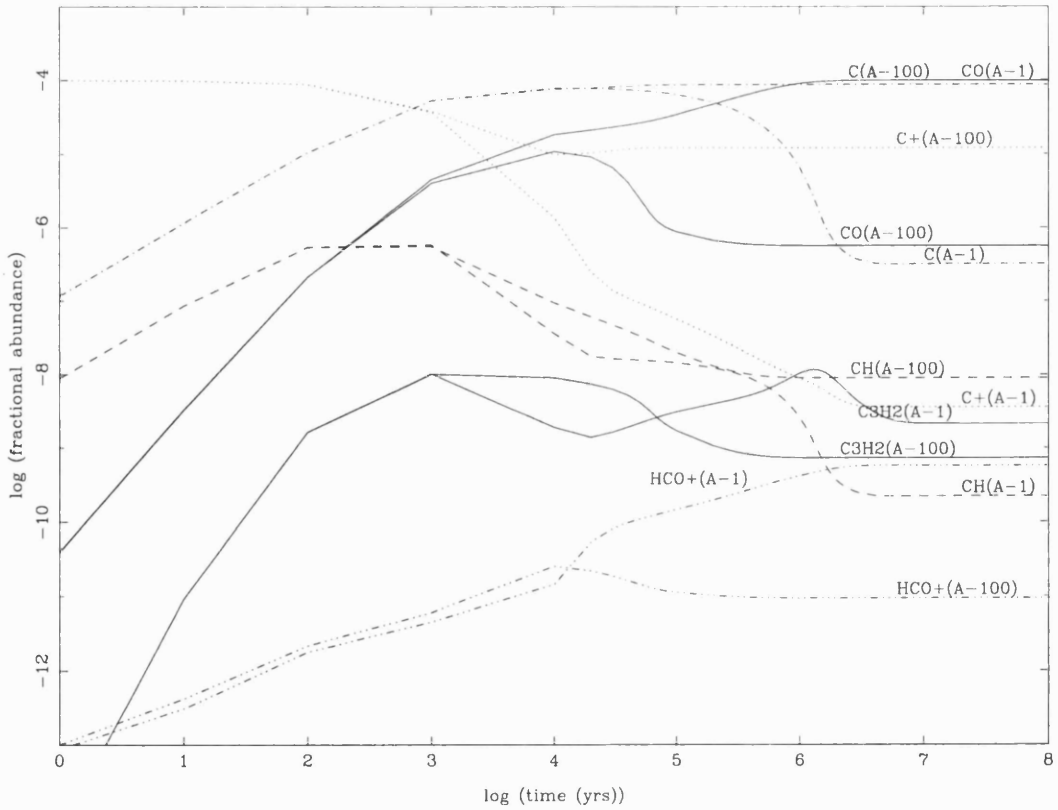

Figure 3.3: Fractional abundance results for selected species for Models A 1ζ and 100ζ (s^{-1}). CO and C_3H_2 are depicted by —, – · – represents C, · · · denotes C^+, – – – depicts CH and – · · · – represents HCO^+. (B-1) represents Model A with ionization rate of 1ζ and (B-100) represents Model A with ionization rate of 100ζ (s^{-1}).

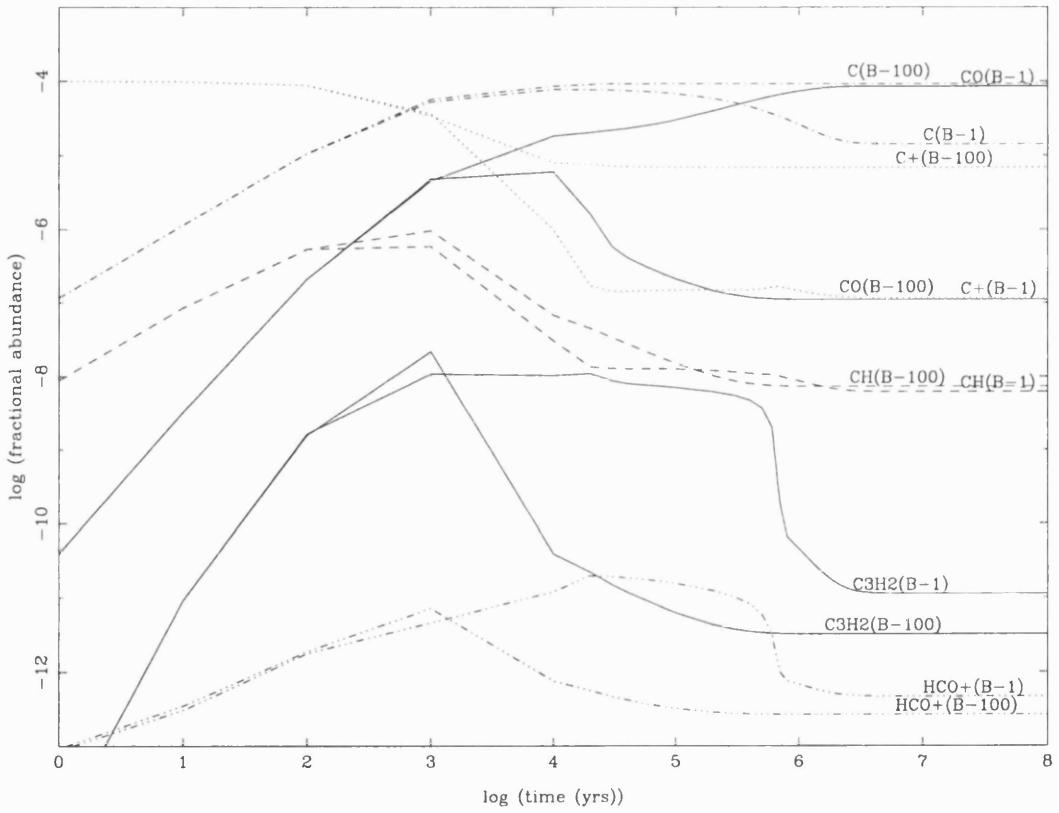

Figure 3.4: Fractional abundance results for selected species for Models B 1ζ and 100ζ (s^{-1}). CO and C_3H_2 are depicted by —, – · – represents C, · · · denotes C^+, – – – depicts CH and – · · · – represents HCO^+. (B-1) represents Model B with ionization rate of 1ζ and (B-100) represents Model B with ionization rate of 100ζ (s^{-1}).

Table 3.2 presents results for Models A, B and C, after steady state has been reached. These tabulated results illustrate clearly the points made above, and in particular emphasize the important prediction that there are rather few tracers of low temperature interfaces.

Models C (initially molecular–rich) give results that differ considerably from those of Models B. Most notably, the results for Model C, 1ζ case are a high ionization solution in which C^+ is a very abundant ion and the priority order of the fractional abundances of C^+, C and CO is reversed from Model B, 1ζ. Consequently, some of the hydrocarbons, e.g. C_2H, are considerably enhanced in abundance. Intuitively, one might expect the chemistry predicted in Models B and C to differ at intermediate times but to converge as one approaches the steady state. This is apparently not the case. In the astrochemistry literature, the term "bistability" is associated with the existence of two solutions of the chemical rate equations for steady–state conditions. The existence of two mathematical solutions for certain regions of parameter space has been known for some time and has been investigated by Le Bourlot *et al.* (1993) and Lee *et al.* (1998). The two stable steady–state solutions are labelled the high ionization phase and the low ionization phase. The high ionization solution is characterized by a high C/CO abundance ratio, whereas the low ionization solution is characterized by a low C/CO abundance ratio.

For the most part, in Model C the 100ζ case shows very similar trends to that of the 1ζ case, with the notable exception of an enhancement in the abundance of OH and H_2O. As with the CH enhancement between Models A and B stated earlier, this can be attributed to the increase in ionization rate. It remains unclear whether the high ionization solutions represent physical reality. Some authors have found the solutions to be very sensitive to parameter choices and to exist over rather narrow regions of parameter space (Pineau des Forêts *et al.*, 1992; Le Bourlot *et al.*, 1993, 1995). It appears that bistability is less likely to appear where the models are made

Table 3.2: Steady–state fractional abundances for a selection of species for Models A, B, and C.

Species	1ζ (s^{-1})			100ζ (s^{-1})		
	Model A	Model B	Model C	Model A	Model B	Model C
H	1.2(−04)	8.8(−05)	4.3(−03)	1.2(−02)	7.9(−03)	1.0(−02)
H^+	4.7(−10)	3.2(−06)	1.4(−05)	2.9(−06)	3.3(−05)	1.3(−05)
O	9.1(−05)	1.1(−04)	2.0(−04)	2.0(−04)	2.0(−04)	2.0(−04)
OH	8.1(−08)	1.8(−10)	4.0(−11)	2.9(−08)	3.2(−09)	1.2(−09)
H_2O	1.9(−06)	4.5(−11)	—	6.2(−09)	5.0(−10)	5.3(−11)
C_2H_2	4.1(−09)	6.1(−11)	1.6(−10)	8.1(−10)	1.3(−11)	6.3(−11)
C	3.6(−07)	1.5(−05)	1.1(−05)	8.7(−05)	9.3(−05)	1.2(−05)
C^+	3.8(−09)	1.2(−07)	8.9(−05)	1.2(−05)	6.9(−06)	8.8(−05)
CH	2.5(−10)	6.3(−09)	9.6(−08)	9.0(−09)	7.3(−09)	4.9(−08)
CH_2	5.1(−11)	1.7(−09)	6.0(−09)	4.6(−10)	4.9(−10)	2.5(−09)
CH_3	4.2(−11)	6.4(−11)	1.2(−10)	2.9(−10)	3.4(−11)	8.8(−11)
C_2H	4.8(−11)	9.6(−11)	1.2(−08)	3.1(−09)	2.0(−10)	4.8(−09)
C_3H	4.1(−08)	1.8(−11)	1.4(−10)	6.7(−10)	—	3.8(−11)
C_3H_2	4.2(−09)	1.2(−11)	—	7.3(−10)	—	—
CO	1.0(−04)	8.5(−05)	8.8(−08)	5.6(−07)	1.1(−07)	3.8(−08)
HCO^+	5.6(−10)	—	—	—	—	—
H_2CO	1.6(−08)	4.1(−11)	—	1.1(−10)	—	—
S	1.7(−09)	5.8(−11)	3.1(−10)	5.1(−10)	5.0(−10)	3.3(−10)
S^+	4.1(−11)	1.9(−08)	2.0(−08)	1.9(−08)	1.9(−08)	2.0(−08)
CS	1.6(−08)	3.6(−10)	1.6(−11)	1.3(−10)	—	—
He	7.0(−02)	7.0(−02)	7.0(−02)	7.0(−02)	7.0(−02)	7.0(−02)
He^+	2.5(−10)	3.2(−10)	7.1(−09)	8.2(−07)	8.8(−07)	7.1(−07)
Mg	1.5(−09)	1.4(−10)	1.3(−10)	1.4(−10)	1.4(−10)	1.3(−10)
Mg^+	1.5(−09)	2.9(−09)	2.9(−09)	2.9(−09)	2.9(−09)	2.9(−09)
N	7.9(−07)	1.8(−05)	2.0(−05)	2.0(−05)	2.0(−05)	2.0(−05)
N^+	1.1(−11)	—	—	2.9(−10)	6.7(−11)	5.3(−11)
NH_3	1.7(−08)	—	—	1.4(−11)	—	—
HC_3N	8.7(−10)	—	—	—	—	—
Na^+	1.4(−07)	2.0(−07)	2.0(−07)	1.9(−07)	2.0(−07)	2.0(−07)
C_4	4.8(−10)	—	3.0(−10)	7.8(−10)	—	5.4(−11)
Na	6.4(−08)	4.9(−09)	5.0(−09)	5.2(−09)	4.8(−09)	5.0(−09)
Si	1.5(−10)	3.0(−10)	4.8(−11)	1.4(−10)	2.1(−10)	5.3(−11)
Si^+	1.1(−10)	6.7(−09)	7.0(−09)	6.9(−09)	6.8(−09)	6.9(−09)

Notation: a(b) $\equiv$ a $\times$ 10^b; A dash (–) indicates that the fractional abundance $< 1(-12)$.

more complex, including for example time dependence and freeze–out of species onto dust grains. A series of models were made to test the robustness of the high ionization state found. These models were made assuming varying densities and temperature conditions. The models also assumed the same initial molecular rich conditions used in Models C. The results from these models, for the same selection of species as discussed in Table 3.2 are given in Table 3.3. From a consideration of these extra models, it is found that the high ionization state appears stable. If Model C results do represent reality, then the solution is very striking, and C^+ and C emissions should be strong in interfaces where the material is mainly molecular.

Results for Models D (equation 3.3 switched off) are not presented here. They show the expected behaviour, with only small changes from the results of Models B (significantly reduced H_2^+ formation). A few results for Model E calculations, in which we have assumed a temperature increase are presented in Table 3.4. The changes in Models E results from those of Models B are generally dependent on the specific species being studied. For the 1ζ case, species such as CO, CH and He^+ show very little change, whereas a two order of magnitude change in abundance can be seen for some species such as OH, H_2O, HCO^+ and NH_3. The effect of an increase in temperature is even more pronounced in the 100ζ case. Even the species which showed fairly small changes for 1ζ show a fairly significant change in abundance in the case of high ionization rate. Therefore, the mixing zone temperature plays a critical role in determining its chemistry.

Table 3.3: Steady–state fractional abundances for a selection of species for extra models to test validity of bistability.

n_H (cm^{-3})	10^4		10^5	
T (K)	10		100	
ζ (s^{-1})	1ζ	100ζ	1ζ	100ζ
H	4.0(−03)	2.8(−02)	2.4(−03)	3.2(−03)
H^+	4.3(−08)	4.2(−06)	3.9(−10)	4.5(−08)
O	2.0(−04)	2.0(−04)	2.0(−04)	2.0(−04)
OH	3.3(−09)	3.2(−07)	3.8(−11)	3.6(−10)
H_2O	5.7(−10)	5.3(−08)	—	4.7(−11)
C_2H_2	5.9(−11)	1.1(−11)	1.7(−09)	1.3(−09)
C	3.7(−06)	4.7(−06)	4.4(−05)	4.4(−05)
C^+	9.6(−05)	9.3(−05)	5.4(−05)	5.4(−05)
CH	7.6(−08)	1.5(−08)	1.4(−07)	1.1(−07)
CH_2	5.0(−09)	6.5(−10)	6.9(−09)	5.2(−09)
CH_3	4.9(−11)	3.5(−11)	1.9(−10)	1.8(−10)
C_2H	1.3(−08)	2.4(−09)	2.9(−08)	2.3(−08)
C_3H	7.7(−11)	1.3(−11)	5.1(−10)	4.0(−10)
C_3H_2	1.5(−10)	2.5(−11)	1.8(−09)	1.4(−09)
CO	1.1(−07)	1.9(−06)	1.5(−06)	1.2(−06)
HCO^+	2.0(−11)	1.1(−09)	—	—
H_2CO	—	—	2.3(−11)	2.1(−11)
S	8.4(−11)	9.6(−11)	4.9(−10)	4.7(−10)
S^+	2.0(−08)	2.0(−08)	1.9(−08)	1.9(−08)
CS	1.7(−11)	—	6.6(−10)	5.1(−10)
He	7.0(−02)	7.0(−02)	7.0(−02)	7.0(−02)
He^+	2.6(−09)	2.3(−07)	5.1(−10)	5.6(−08)
Mg	1.8(−11)	1.8(−11)	1.3(−10)	1.3(−10)
Mg^+	3.0(−09)	3.0(−09)	2.9(−09)	2.9(−09)
N	2.0(−05)	2.0(−05)	2.0(−05)	2.0(−05)
Na^+	2.0(−07)	2.0(−07)	2.0(−07)	2.0(−07)
C_4	2.0(−10)	2.8(−11)	4.1(−09)	3.1(−09)
Na	1.0(−09)	1.0(−09)	5.0(−09)	5.0(−09)
Si	1.3(−11)	1.6(−11)	1.0(−10)	1.0(−10)
Si^+	7.0(−09)	7.0(−09)	(6.9−09)	6.9(−09)

Notation: a(b) $\equiv$ a $\times$ 10^b; A dash (–) indicates that the fractional abundance $< 1(-12)$.

Table 3.4: Steady–state fractional abundances for a selection of species, for Model B (T = 10 K) and Model E (T = 100 K).

Species	1ζ (s^{-1})		100ζ (s^{-1})	
	T=10 K	T=100 K	T=10 K	T=100 K
H	8.8(−05)	1.8(−04)	7.9(−03)	x.8(−02)
H^+	3.2(−06)	4.1(−08)	3.3(−05)	2.8(−06)
O	1.1(−04)	9.6(−05)	2.0(−04)	1.1(−04)
OH	1.8(−10)	4.9(−08)	3.2(−09)	2.2(−06)
H_2O	4.5(−11)	4.8(−07)	5.0(−10)	7.8(−07)
C_2H_2	6.1(−11)	6.5(−11)	1.3(−11)	8.6(−11)
C	1.5(−05)	6.8(−07)	9.3(−05)	1.5(−05)
C^+	1.2(−07)	1.0(−07)	6.9(−06)	9.6(−07)
CH	6.3(−09)	2.7(−10)	7.3(−09)	4.2(−10)
CH_2	1.7(−09)	5.7(−11)	4.9(−10)	2.8(−11)
CH_3	6.4(−11)	—	3.4(−11)	5.6(−11)
C_2H	9.6(−11)	—	2.0(−10)	2.7(−10)
C_3H	1.8(−11)	—	—	5.6(−11)
C_3H_2	1.2(−11)	—	—	2.0(−11)
CO	8.5(−05)	9.9(−05)	1.1(−07)	8.4(−05)
HCO^+	—	3.4(−10)	—	3.3(−09)
H_2CO	4.1(−11)	3.3(−10)	—	3.4(−11)
S	5.8(−11)	1.0(−08)	5.0(−10)	4.2(−09)
S^+	1.9(−08)	6.9(−09)	1.9(−08)	1.5(−08)
CS	3.6(−10)	2.3(−09)	—	6.2(−10)
He	7.0(−02)	7.0(−02)	7.0(−02)	7.0(−02)
He^+	3.2(−10)	2.4(−10)	8.8(−07)	2.8(−08)
Mg	1.4(−10)	7.5(−11)	1.4(−10)	2.1(−11)
Mg^+	2.9(−09)	3.0(−09)	2.9(−09)	3.0(−09)
N	1.8(−05)	3.5(−06)	2.0(−05)	1.5(−05)
N^+	—	—	6.7(−11)	—
NH_3	—	1.2(−08)	—	3.0(−09)
HC_3N	—	—	—	—
Na^+	2.0(−07)	2.0(−07)	2.0(−07)	2.0(−07)
C_4	—	—	—	—
Na	4.9(−09)	3.7(−09)	4.8(−09)	1.0(−09)
Si	3.0(−10)	5.4(−10)	2.1(−10)	1.2(−09)
Si^+	6.7(−09)	5.1(−09)	6.8(−09)	5.7(−09)

Notation: a(b) $\equiv$ a $\times$ 10^b; A dash (–) indicates that the fractional abundance $< 1(-12)$.

3.4 Conclusions

The method described here offers a simple approach to the prediction of the appearance of important tracers in mixing zones between cold molecular gas and warm ionized gas. If the temperature remains low, then C, C^+ and CH are enhanced in the mixing zone. The enhancement is dramatic if the high ionization solution is a valid representation.

If there is an increase in temperature after mixing has occurred a different set of tracers would be needed to identify mixing in the gas. For instance CH would now not be a very good tracer of mixing, but OH, H_2O, HCO^+ and NH_3 are significantly enhanced because the higher temperature drives the H^+/O charge exchange reaction, which feeds the oxygen chemistry. Mixing is most likely accompanied by heating. Therefore, we might expect the results for the type E, 100ζ to be most typical for mixing layer chemistry. Our calculations indicate that such mixing zones should be deficient in species such as CH while the abundance of OH should increase.

CHAPTER 4

Polyatomic Species in Diffuse Cloud and Clump Interfaces

Dynamical effects may influence the physical conditions in *interfaces*, and hence affect the potential tracers of those interfaces. such tracers, therefore, may be useful in constraining the dynamical processes. Diffuse clouds embedded in a flowing intercloud medium will develop warm interface layers in which the thermal pressures should significantly exceed those within the cloud. We have investigated the gas–phase formation of polyatomic molecules within such warm interfaces. We find that if an interface layer occupies a few percent of the total molecular column density along that line–of–sight, then many polyatomic species in that interface should have detectable abundances.

4.1 Introduction

Lucas and Liszt (1993, 1996, 2000*a*,*b*) and Liszt and Lucas (1995, 1998, 2000) have observed a number of diatomic and polyatomic species in millimeter wavelength absorption against background extragalactic sources along lines–of–sight through

diffuse interstellar clouds. Liszt and Lucas (1999) recently presented a short summary of the results, while Lucas and Liszt (1997) gave a more detailed, review of their work. The low column densities of CO (in the range of 10^{14} cm^{-2} to 10^{16} cm^{-2}) and its fractionation constrain most of the CO to lie in cold diffuse material where much of the carbon is in the form of C^+. In addition to CO, the species detected in absorption include HCO^+, OH, CN, HCN, HNC, C_2H, H_2CO, C_3H_2, CS, SO, H_2S and SiO. Liszt and Lucas (1999) noted that the presence of many of these species in the detected abundances is a mystery similar to that of the high abundances measured for CH^+ in diffuse clouds.

The high abundance of CH^+ in diffuse clouds is a mystery because the main formation route of CH^+ in these regions (given by equation 4.1) is an endothermic reaction, and is therefore thought to be very slow. This is coupled with the fact that CH^+ can be rapidly destroyed via reaction with H, H_2 and electrons. Standard gas–phase models predict a CH^+ fractional abundance which is lower than observed values by at least one–two orders of magnitude.

$$C^+ + H_2 \longrightarrow CH^+ + H \tag{4.1}$$

A number of explanations, summarized by van Dishoeck (1998), have been offered as solutions to the CH^+ problem. van Dishoeck (1998) note that energetic processes are needed to stir up the gas and drive reaction 4.1. Elitzur and Watson (1978) propose that a shock wave in a diffuse cloud would cause a high temperature increase, thereby driving the endothermic CH^+ formation reaction (4.1). The gas may also be heated by the presence of a strong radiation field, although these models do have problems.

A more recent shock model was proposed by Flower and Pineau des Forêts (1998), who studied the propagation of a C–type shock through a diffuse cloud, although line profile data (e.g. Liszt and Lucas, 2000) present difficulty for these shock models. Liszt and Lucas (2000) provide observational data of HCO^+ and OH which show

no signatures indicative of shocks. One of the explanations examined by Duley *et al.* (1992) involves the possibility that CH^+ is abundant in the interface regions between cold clumps and more tenuous, hotter media flowing around them. Here we investigate the possibility that the polyatomic species detected by Liszt and Lucas are formed in such interface regions.

§ 4.2 describes briefly the physical properties likely to be obtained in the interfaces. § 4.3 contains a summary of the assumptions made in the construction of the chemical models and calculated fractional abundances for the models. § 4.4 presents a discussion of our results, and we make a short conclusion in § 4.5.

4.2 Turbulent Boundary Layers

The tenuous intercloud medium surrounding a diffuse cloud is almost certainly in motion around the cloud since stellar winds and supernovae drive flows throughout the intercloud medium. The flow may be of fairly moderate to low Mach number (M), in which case the cloud can be confined for a time substantially in excess of its fast–mode magnetosonic crossing time. However, even if the tenuous material flows at a fairly low Mach number relative to a cloud, the flow establishes pressure differences on the cloud surface as a consequence of the Bernoulli effect. Cloud material will move to the region of the surface where the pressure is lowest at a speed of order $M^2 c_f$, where c_f is the fast–mode speed in the cloud (e.g. Hartquist and Dyson, 1988) for all but very small values of M. Thus, H_2 will reach the surface of a diffuse cloud (Hartquist *et al.*, 1992). There it is heated due to the dissipation of waves generated by the Kelvin–Helmholtz instability occurring at the cloud–intercloud interface. As discussed by Duley *et al.* (1992), the heating may result in temperatures of many hundreds or even thousands of degrees in H_2–rich gas moving at speeds well below c_f with respect to the bulk of the cloud. The scenario is depicted in Fig. 4.1.

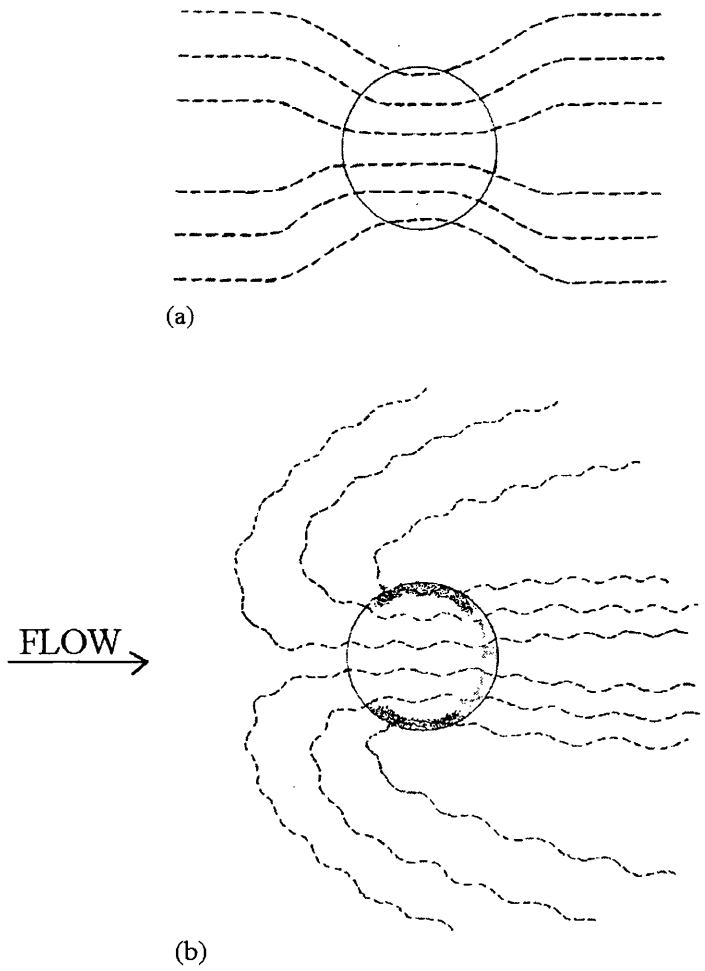

Figure 4.1: The magnetic field and thermal structures of a diffuse cloud. a) The intercloud medium is static. The magnetic field lines are somewhat bent as the field contributes to the support of the cloud against the pressure of the intercloud medium. b) A subsonic flow engulfs the cloud. Magnetic field lines are bent around the cloud by the flow. The existence of hydromagnetic waves is indicated by undulations in the field lines and is likely to be a consequence of the flowing intercloud medium with the cloud. The shaded regions are those to which H_2 flows most rapidly to the surface; the shading is darkest in those interface regions containing H_2 where the viscous heating rate is probably greatest.

Duley *et al.* (1992) assumed that the gas in the interface would be at a thermal pressure comparable to the thermal pressure of the cloud. In fact, if the motions giving rise to the broadening of spectral features in the cloud are very superthermal, the thermal pressure in some parts of the interface region may well substantially exceed the thermal pressure in the cloud. In the vicinity of a steady interface structure the sum of the wave and thermal pressures must be nearly constant along a largescale magnetic field line; within the WKB approximation (e.g. Barnes, 1992) the wave pressure goes up as $\rho^{1/2}$, where ρ is the density. If the superthermal motions in clouds are due to waves generated at their surfaces propagating into them (e.g. Coker *et al.*, 2000) the thermal pressure in the low density part of the interface regions will exceed the thermal pressure in the bulk of the cloud.

The fraction, f, of the total pressure acting along a large–scale magnetic field line, $P_{\rm tot}$, that is thermal pressure, $P_{\rm th}$, can be calculated from:

$$f \equiv \frac{P_{\rm th}}{P_{\rm tot}} \tag{4.2}$$

$$P_{\rm th} = \frac{k_{\rm B}\ \rho\ T}{\mu} \tag{4.3}$$

$$P_{\rm tot} = P_{\rm th} + U \tag{4.4}$$

where $k_{\rm B}$ is Boltzmann's constant, ρ is the density, T is the temperature, μ is the mean mass per particle, and U is the time–averaged energy density of the perturbation magnetic field (e.g. Martin *et al.*, 1997). Substituting $P_{\rm tot}$ from equation 4.2 into equation 4.4 and dividing through by $P_{\rm tot}$ gives,

$$\frac{U}{P_{\rm tot}} = 1 - f \tag{4.5}$$

If the wave is an Alfvén wave and V is its velocity amplitude, and subscript c indicates that the quantity is equivalent at the cold side of the interface,

$$U = \frac{1}{4}\ \rho_c\ V_c^2 \left(\frac{\rho}{\rho_c}\right)^{1/2} \tag{4.6}$$

Equation 4.6 is correct in the WKB–limit. Therefore substituting U and the corresponding U_c value from equation 4.6 into equation 4.5 gives,

$$\frac{1-f}{1-f_c} = \left(\frac{\rho}{\rho_c}\right)^{1/2} \tag{4.7}$$

Multiplying through by $(1 - f_c)/f_c$ gives,

$$\frac{f}{f_c} = \frac{1}{f_c} - \frac{(1-f_c)}{f_c}\left(\frac{\rho}{\rho_c}\right)^{1/2} \tag{4.8}$$

From the definition of f from equation 4.2 and the fact that $P_{\rm th}$ depends on $\rho\, T$ from equation 4.3 we get,

$$\frac{f}{f_c} = \frac{\rho\, T}{\rho_c\, T_c} \tag{4.9}$$

Substituting this into equation 4.8 and defining $X \equiv (\rho/\rho_c)^{1/2}$ gives,

$$\left(\frac{T}{T_c}\right) X^2 + \left(\frac{1-f_c}{f_c}\right) X - \left(\frac{1}{f_c}\right) = 0 \tag{4.10}$$

Solving this quadratic equation gives the following solution,

$$\left(\frac{\rho}{\rho_c}\right)^{1/2} = -\frac{(1-f_c)}{2f_c}\,\frac{T_c}{T} + \left[\frac{(1-f_c)^2}{4f_c^2}\,\frac{T_c^2}{T^2} + \frac{T_c}{f_c T}\right]^{1/2} \tag{4.11}$$

For $V_c = 3$ km s^{-1} and $T_c = 100$ K, then $f_c \simeq 0.13$, implying that the thermal pressure in warm regions of the interface is about 7 times that in the cooler regions.

Duley *et al.* (1992) limited their considerations to interface gas with thermal pressure comparable to the highest thermal pressures thought to be associated with diffuse molecular clouds observed with Copernicus. However, observations of those clouds showed evidence of superthermal motions. Consequently, we will consider here, interface region pressures substantially exceeding the thermal pressures of the diffuse molecular clouds, as well as more modest interface region pressures.

Table 4.1: Parameters set for the grid of models.

Parameter	Range of Values
Temperature, T (K)	700, 2000, 4000
Pressure, n_H T (cm^{-3} T)	4(03), 1(04), 4(04), 1(05), 4(05), 1(06)
Radiation Field, χ	0.1, 0.3, 1.0

Notation a(b) $\equiv$ a $\times$ 10^b.

4.3 Model Calculations

We argued in the previous section that H_2–rich gas will move to the vicinity of a cloud surface, where the pressure is lowest, rapidly enough that little of the H_2 in it will be photodissociated. Therefore, we assume that all hydrogen entering the interface is initially H_2 and that its photodissociation rate is negligible. This scenario was studied by running a grid of models, assuming a range of values for the parameters, density (n_H), pressure (n_H T) and χ, which is the measure of the incident radiation field, set to be unity for the standard interstellar background radiation field. The parameter range is given in Table 4.1. The number density of hydrogen nuclei, n_H, and T, were held constant. The assumed initial elemental abundances relative to that of hydrogen are those equivalent to a diffuse cloud (given in Table 1.2). All elements whose neutral atoms have ionization potentials less than that of hydrogen were assumed to be in the form of singly charged atomic ions initially (e.g. C^+ and S^+, etc.), while all other elements were taken to be in neutral atomic form. Integrations of the chemical rate equations were halted after about 10^4 yrs., by which time the abundances of all species of interest had reached steady–state. The model results for the fractional abundances of selected species relative to n_H are given in Tables 4.2-4.4.

4.4 Results and Discussion

Warm interface regions are likely to contain only a few percent of the column density of a cloud (Hartquist *et al.*, 1992). Therefore for a species i to have a column density of about 10^{12} cm^{-2} in a warm interface of a diffuse cloud it must have a fractional abundance, $X(i)$, relative to $n_{\rm H}$ of about 3×10^{-8}. A number of the models listed in Table 4.2 give fractional abundances of this magnitude and greater for a variety of the species observed by Liszt and Lucas in millimeter wave absorption. However, only a few models give abundance ratios of key polyatomic species similar to those measured.

We focus first on the C_2H to HCO^+ abundance ratio which Lucas and Liszt (2000*b*) have found to vary but often to have a value in the range 10 to 20. Models 11 and 18 are the only ones with values of that ratio in the observed range, while the values for models 12 and 17 are greater. Of these four models, only model 11 has an OH to HCO^+ abundance ratio within rough agreement with the measured values which are almost uniformly between about 20 to 30 (Lucas and Liszt, 1996). For models 12 and 17, as well as for models 11 and 18, $\chi = 0.1$, and the fact that χ must be somewhat lower than usually assumed is probably not a serious constraint. As the observations are made over a long line–of–sight, the locations of many of the absorbing diffuse clouds are most likely uncertain. In fact, the use of such background sources may well introduce selection effects favouring the detection of clouds in regions with low values of χ. Clouds in regions with large values of χ may well contain less than the lowest detectable column density of CO. It is likely that a number of the diffuse clumps may reside in or around Giant Molecular Clouds and that the material in such complexes at least partially shields the detected diffuse clouds from the general interstellar radiation field.

The values of $n_{\rm H}T$ for the models having C_2H to HCO^+ and OH to HCO^+ abundance ratios in rough agreement with the measured ratios are one to one and a half

orders of magnitude higher than the value of $n_{\rm H}T$ that Duley *et al.* (1992) suggested is compatible with a warm interface being the site of CH^+ and a component of CH observed by Lambert *et al.* (1990) towards the ζ Oph cloud. However, as CH^+ data do not exist for the lines–of–sight studied by Liszt and Lucas (since these do not have a background UV source), considerations of its production should not be used as too stringent a constraint in the discussion of the models for the polyatomic data. Optical and ultraviolet absorption studies, like those in which CH^+ is detected, are normally aimed at the investigation of somewhat isolated or "field" diffuse clouds. As mentioned above, along the line–of–sight to an extragalactic source, a fair fraction of the diffuse structures (for which the total visual extinction optical depths are unity or less) intercepted may be clumps associated with Giant Molecular Clouds (GMCs). Many of these GMCs have MHD wave "pressures" (e.g. Williams *et al.*, 1995) comparable to the thermal pressures required for the interface models to have C_2H/HCO^+ and OH/HCO^+ abundance ratios similar to those measured by Lucas and Liszt (1996, 2000*b*).

We now compare several other measured abundance ratios reviewed by Lucas and Liszt (1997) to those given by the models, with particular emphasis given to model 11. Lucas and Liszt (2000*b*) give a value of around 30 as the typical measured abundance ratio of C_2H to ortho–C_3H, a value close to that for model 18 but almost a factor of 5 lower than that of model 11. Of course, it should be noted that the reliability of the underlying chemical network becomes more uncertain as the number of atoms, particularly those other than hydrogen, contained in the species under consideration increases. C_3H in this sense is a rather complicated species, and a factor of 5 should not be considered a serious discrepancy. The values of the CN to HCN abundance ratio for models 11, 12, 17 and 18 are all much less than the measured values, as would be expected if CN is a molecule produced in abundance by cold gas–phase reactions. Therefore, much of the CN is contained

in the cold material. Likewise, interface model CO to HCO^+ abundance ratios are much smaller than measured values, a fact consistent with the great majority of the CO being in cold regions, as demanded by the observations of its extinction. The CS to HCO^+ abundance ratio for model 11 is somewhat lower than typically measured ratios. Better agreement would follow if elemental sulphur were undepleted, as X(CS) scales with the fractional abundance of sulphur (the sulphur abundance for diffuse clouds given in Table 1.2 and adopted here implies a depletion by a factor of 5 relative to solar).

The explanation of the millimeter absorption data in terms of the interface models faces some difficulties. Perhaps, the most severe one arises from the data for $X(H_2CO)/X(HCO^+)$. Although H_2CO has not been detected along all lines–of–sight on which HCO^+ is found, it commonly has an abundance ratio relative to HCO^+ that is over one order of magnitude larger than that of model 11 (Liszt and Lucas, 1995). However, it should be recalled that no gas–phase chemical model is able to account satisfactorily for diffuse cloud formaldehyde. Consequently, some authors (e.g. Viti and Williams, 1999*a*) have invoked surface reactions on dust to account for its formation. The values of $X(HCN)/X(HCO^+)$ for models giving reasonable values of the ratios $X(C_2H)/X(HCO^+)$ and $X(OH)/X(HCO^+)$ are over one order of magnitude higher than usually measured. Model values of the HNC to HCN abundance ratio are much lower than observed, a fact that may reflect an underlying incompleteness in the treatment of the HNC chemistry rather than a problem with the basic concept behind the models. For example, the reaction network adopted here allows the formation of HCN, but not HNC, from the reactants CH_3 and N.

We find that $X(C_2) \gtrsim 10^{-6}$ for many models. Though it is not detectable in millimeter wave absorption due to its symmetry, C_2 is detectable in absorption in the red against bright enough background stars, and observations of it have been used to constrain temperatures of diffuse molecular clouds to low values (van Dishoeck and

Black, 1986). Previously measured column densities have been several to many times 10^{13} cm^{-2}. Without more detailed analysis it is difficult to say how stringent the constraints C_2 data place on the properties of warm regions of diffuse clouds towards which it has been observed. χ is most likely greater than 0.3 for most nearby clouds through which C_2 absorption has been detected; that $X(C_2)$ falls with increasing χ in the interface models probably ensures that interface contributions to C_2 features already detected are not dominant.

The high NH abundances in some models are of great interest. The reaction $N + H_2 \rightarrow NH + H$ has a barrier of about 16,000 K (Millar *et al.*, 1997), and NH is not formed efficiently by low temperature gas phase chemistry. Its detection in some lines–of–sight through diffuse clouds has been interpreted as evidence of the importance of grain surface reactions (Wagenblast *et al.*, 1993; Crawford and Williams, 1997). Evidently, large amounts of NH may arise in warm interfaces. It is possible that the elevated temperature may promote the surface reaction.

4.5 Conclusions

Interface regions around a diffuse cloud embedded in a flowing intercloud medium should have thermal pressures that are significantly larger than those within the cloud. In this chapter we have explored the gas–phase chemistry arising in such warm interfaces. We have compared the results of interface models with observational data on polyatomic species obtained by Liszt and Lucas. Our results show that observable abundances of various polyatomic species can be produced if the warm interface layer occupies a few percent of the total molecular column density along that line–of–sight. Some models give results that are in harmony with measured ratios of several species including C_2H, HCO^+ and OH; these models have background radiation field intensities that are lower than the standard by an order of magnitude. The number densities of molecular hydrogen are of the order of 10^2

cm^{-3} in regions with temperatures of several thousand degrees. Such conditions in an interface do not conflict with the lower pressures inferred from CO data, as most of the CO is expected to be in the cold bulk of the material rather than in interfaces. The constancy of the sum of MHD wave "pressure" and thermal pressure implies higher thermal pressures in interfaces than in the cold cloud and cold clump material. For models in which the radiation field intensity is about one tenth of the mean interstellar radiation field intensity, then the agreement with observations of Liszt and Lucas is reasonable. Such conditions may be more likely in interfaces around diffuse clumps within Giant Molecular Clouds than those around the isolated "field" diffuse clouds observed in ultraviolet absorption. Some measured abundance ratios, the most notable of which is that of the abundances of H_2CO and HCO^+, are not well matched by model results, though on the basis of the models the relevant species would be expected to be observable in some cases. However, in some cases the results suggest that the gas–phase chemical network used may be too limited. Surface reactions may also contribute to molecular abundances in both warm interfaces and in the cold cloud gas.

Table 4.2: Results for selected species for models 1–54 at time 10^4 yrs.

Model	T (K)	n_H T (cm^{-3} K)	χ	X(CH)	X(CH$^+$)	X(CN)	X(OH)	X(H$_2$O)
1	7(02)	4(03)	0.1	9.92(−07)	6.95(−08)	1.20(−10)	1.69(−06)	4.37(−08)
2	7(02)	1(04)	0.1	2.41(−06)	5.91(−08)	6.33(−10)	3.93(−06)	2.23(−07)
3	7(02)	4(04)	0.1	6.12(−06)	4.02(−08)	1.02(−08)	1.15(−05)	1.94(−06)
4	7(02)	1(05)	0.1	6.73(−06)	2.37(−08)	3.59(−08)	1.91(−05)	6.37(−06)
5	7(02)	4(05)	0.1	3.25(−06)	7.26(−09)	8.23(−08)	2.94(−05)	3.27(−05)
6	7(02)	1(06)	0.1	1.07(−06)	2.47(−09)	1.31(−07)	3.51(−05)	1.28(−04)
7	2(03)	4(03)	0.1	1.22(−05)	6.41(−06)	2.92(−09)	1.32(−04)	2.98(−05)
8	2(03)	1(04)	0.1	2.06(−05)	3.15(−06)	9.74(−09)	2.00(−04)	1.10(−04)
9	2(03)	4(04)	0.1	2.42(−05)	6.98(−07)	5.69(−08)	1.65(−04)	3.52(−04)
10	2(03)	1(05)	0.1	2.06(−05)	2.03(−07)	1.09(−07)	9.21(−05)	4.79(−04)
11	2(03)	4(05)	0.1	1.13(−05)	2.30(−08)	7.81(−08)	3.00(−05)	5.63(−04)
12	2(03)	1(06)	0.1	6.62(−06)	4.86(−09)	4.09(−08)	1.49(−05)	5.82(−04)
13	4(03)	4(03)	0.1	1.18(−05)	2.21(−05)	8.70(−09)	2.88(−04)	1.46(−04)
14	4(03)	1(04)	0.1	2.53(−05)	1.08(−05)	2.60(−08)	2.37(−04)	2.83(−04)
15	4(03)	4(04)	0.1	2.83(−05)	2.08(−06)	4.61(−08)	1.22(−04)	4.56(−04)
16	4(03)	1(05)	0.1	1.91(−05)	4.98(−07)	3.69(−08)	7.81(−05)	5.11(−04)
17	4(03)	4(05)	0.1	1.37(−05)	6.29(−08)	2.99(−08)	7.13(−05)	5.19(−04)
18	4(03)	1(06)	0.1	4.33(−05)	8.49(−08)	9.59(−08)	1.59(−04)	3.88(−04)
19	7(02)	4(03)	0.3	2.91(−07)	9.32(−08)	2.60(−11)	5.82(−07)	5.90(−09)
20	7(02)	1(04)	0.3	8.18(−07)	7.21(−08)	8.95(−11)	1.42(−06)	3.08(−08)
21	7(02)	4(04)	0.3	3.01(−06)	5.52(−08)	1.07(−09)	5.02(−06)	3.59(−07)
22	7(02)	1(05)	0.3	5.26(−06)	4.22(−08)	5.53(−09)	1.00(−05)	1.45(−06)
23	7(02)	4(05)	0.3	5.11(−06)	1.99(−08)	2.37(−08)	2.00(−05)	7.66(−06)
24	7(02)	1(06)	0.3	2.49(−06)	8.61(−09)	3.30(−08)	2.62(−05)	2.28(−05)
25	2(03)	4(03)	0.3	3.00(−06)	1.03(−05)	7.01(−10)	5.56(−05)	4.23(−06)
26	2(03)	1(04)	0.3	9.67(−06)	6.81(−06)	2.15(−09)	1.14(−04)	2.10(−05)
27	2(03)	4(04)	0.3	2.14(−05)	2.26(−06)	1.13(−08)	2.03(−04)	1.39(−04)
28	2(03)	1(05)	0.3	2.40(−05)	8.77(−07)	3.38(−08)	1.78(−04)	2.87(−04)
29	2(03)	4(05)	0.3	2.02(−05)	1.71(−07)	1.08(−07)	8.15(−05)	4.68(−04)
30	2(03)	1(06)	0.3	1.59(−05)	5.11(−08)	7.28(−08)	4.31(−05)	5.27(−04)
31	4(03)	4(03)	0.3	1.65(−06)	2.75(−05)	1.56(−09)	2.23(−04)	3.78(−05)
32	4(03)	1(04)	0.3	8.19(−06)	2.23(−05)	6.20(−09)	2.77(−04)	1.09(−04)
33	4(03)	4(04)	0.3	2.93(−05)	8.36(−06)	3.71(−08)	2.29(−04)	2.78(−04)
34	4(03)	1(05)	0.3	4.04(−05)	3.26(−06)	6.99(−08)	1.78(−04)	3.62(−04)
35	4(03)	4(05)	0.3	4.76(−05)	7.41(−07)	8.16(−08)	1.65(−04)	3.76(−04)
36	4(03)	1(06)	0.3	4.27(−05)	6.72(−07)	2.01(−07)	2.14(−04)	1.81(−04)
37	7(02)	4(03)	1.0	4.82(−08)	1.31(−07)	-	1.77(−07)	8.25(−10)
38	7(02)	1(04)	1.0	2.01(−07)	1.02(−07)	1.85(−11)	4.37(−07)	3.38(−09)
39	7(02)	4(04)	1.0	9.74(−07)	6.86(−08)	1.17(−10)	1.68(−06)	4.24(−08)
40	7(02)	1(05)	1.0	2.25(−06)	5.66(−08)	5.49(−10)	3.89(−06)	2.18(−07)
41	7(02)	4(05)	1.0	4.18(−06)	3.55(−08)	3.92(−09)	1.09(−05)	1.75(−06)
42	7(02)	1(06)	1.0	3.25(−06)	2.14(−08)	7.86(−09)	1.69(−05)	5.09(−06)
43	2(03)	4(03)	1.0	1.91(−07)	8.19(−06)	9.66(−11)	1.82(−05)	4.32(−07)
44	2(03)	1(04)	1.0	1.59(−06)	9.93(−06)	4.29(−10)	4.19(−05)	2.34(−06)
45	2(03)	4(04)	1.0	9.23(−06)	5.22(−06)	2.12(−09)	1.19(−04)	2.37(−05)
46	2(03)	1(05)	1.0	1.47(−05)	2.54(−06)	5.39(−09)	1.74(−04)	7.80(−05)
47	2(03)	4(05)	1.0	1.30(−05)	6.59(−07)	1.81(−08)	1.59(−04)	2.32(−04)
48	2(03)	1(06)	1.0	9.79(−06)	2.47(−07)	4.27(−08)	1.09(−04)	3.31(−04)
49	4(03)	4(03)	1.0	6.10(−08)	1.48(−05)	1.66(−10)	1.03(−04)	5.38(−06)
50	4(03)	1(04)	1.0	6.76(−07)	2.27(−05)	8.48(−10)	1.83(−04)	2.19(−05)
51	4(03)	4(04)	1.0	6.98(−06)	1.69(−05)	6.51(−09)	2.58(−04)	9.13(−05)
52	4(03)	1(05)	1.0	1.63(−05)	9.76(−06)	2.00(−08)	2.48(−04)	1.40(−04)
53	4(03)	4(05)	1.0	2.39(−05)	3.85(−06)	7.23(−08)	2.13(−04)	1.17(−04)
54	4(03)	1(06)	1.0	8.25(−06)	2.37(−06)	7.29(−08)	1.27(−04)	2.53(−05)

Notation: a(b) $\equiv$ a $\times$ 10^b; A dash (-) indicates that the fractional abundance $< 1(-12)$.

Table 4.3: Results for selected species for models 1–54 at time 10^4 yrs.

Model	T (K)	n_H T (cm^{-3} K)	χ	X(CO)	X(NH)	X(C_2)	X(HCO^+)	X(H_2CO)
1	7(02)	4(03)	0.1	2.07(−08)	–	2.28(−08)	4.26(−08)	–
2	7(02)	1(04)	0.1	1.22(−07)	–	1.91(−07)	9.21(−08)	5.03(−11)
3	7(02)	4(04)	0.1	1.66(−06)	–	2.86(−06)	3.18(−07)	2.06(−09)
4	7(02)	1(05)	0.1	5.96(−06)	1.03(−11)	6.25(−06)	6.70(−07)	9.25(−09)
5	7(02)	4(05)	0.1	2.35(−05)	1.14(−11)	4.36(−06)	1.90(−06)	2.38(−08)
6	7(02)	1(06)	0.1	4.15(−05)	1.10(−11)	2.14(−06)	2.76(−06)	2.24(−08)
7	2(03)	4(03)	0.1	4.68(−07)	1.14(−07)	2.73(−07)	9.17(−06)	1.62(−09)
8	2(03)	1(04)	0.1	1.61(−06)	2.70(−07)	1.37(−06)	1.39(−05)	1.28(−08)
9	2(03)	4(04)	0.1	3.58(−06)	8.25(−07)	6.29(−06)	9.21(−06)	6.21(−08)
10	2(03)	1(05)	0.1	3.38(−06)	1.22(−06)	1.03(−05)	3.98(−06)	6.62(−08)
11	2(03)	4(05)	0.1	1.84(−06)	7.78(−07)	1.31(−05)	6.37(−07)	2.73(−08)
12	2(03)	1(06)	0.1	1.13(−06)	3.28(−07)	1.37(−05)	1.59(−07)	1.13(−08)
13	4(03)	4(03)	0.1	4.06(−07)	3.86(−06)	1.51(−07)	1.87(−05)	7.15(−09)
14	4(03)	1(04)	0.1	9.84(−07)	6.49(−06)	8.71(−07)	1.79(−05)	2.22(−08)
15	4(03)	4(04)	0.1	1.03(−06)	7.20(−06)	4.03(−06)	4.22(−06)	3.71(−08)
16	4(03)	1(05)	0.1	7.90(−07)	5.36(−06)	7.15(−06)	1.15(−06)	2.67(−08)
17	4(03)	4(05)	0.1	9.54(−07)	4.05(−06)	1.46(−05)	2.35(−07)	1.41(−08)
18	4(03)	1(06)	0.1	8.13(−06)	3.32(−06)	1.05(−05)	8.06(−07)	1.44(−08)
19	7(02)	4(03)	0.3	9.39(−09)	–	1.86(−09)	2.06(−08)	–
20	7(02)	1(04)	0.3	4.44(−08)	–	1.52(−08)	3.69(−08)	–
21	7(02)	4(04)	0.3	6.27(−07)	–	3.35(−07)	1.18(−07)	1.05(−10)
22	7(02)	1(05)	0.3	3.23(−06)	–	1.60(−06)	2.60(−07)	9.21(−10)
23	7(02)	4(05)	0.3	2.04(−05)	–	3.35(−06)	7.34(−07)	4.40(−09)
24	7(02)	1(06)	0.3	5.03(−05)	–	1.98(−06)	1.48(−06)	5.85(−09)
25	2(03)	4(03)	0.3	2.40(−07)	3.84(−08)	1.89(−08)	4.59(−06)	6.52(−11)
26	2(03)	1(04)	0.3	1.10(−06)	9.24(−08)	1.68(−07)	8.59(−06)	8.66(−10)
27	2(03)	4(04)	0.3	6.61(−06)	3.08(−07)	1.56(−06)	1.52(−05)	1.32(−08)
28	2(03)	1(05)	0.3	1.33(−05)	5.57(−07)	3.78(−06)	1.45(−05)	2.62(−08)
29	2(03)	4(05)	0.3	1.88(−05)	6.21(−07)	8.82(−06)	6.55(−06)	2.19(−08)
30	2(03)	1(06)	0.3	1.72(−05)	2.04(−07)	1.20(−05)	2.63(−06)	1.31(−08)
31	4(03)	4(03)	0.3	2.57(−07)	1.53(−06)	7.89(−09)	1.53(−05)	4.68(−10)
32	4(03)	1(04)	0.3	1.24(−06)	3.18(−06)	9.74(−08)	2.66(−05)	3.95(−09)
33	4(03)	4(04)	0.3	3.90(−06)	6.37(−06)	1.12(−06)	1.96(−05)	1.91(−08)
34	4(03)	1(05)	0.3	5.26(−06)	6.39(−06)	2.93(−06)	1.07(−05)	2.41(−08)
35	4(03)	4(05)	0.3	9.14(−06)	3.52(−06)	6.31(−06)	4.41(−06)	1.78(−08)
36	4(03)	1(06)	0.3	3.09(−05)	1.72(−06)	4.72(−06)	6.82(−06)	4.31(−09)
37	7(02)	4(03)	1.0	4.74(−09)	–	8.28(−11)	1.10(−08)	–
38	7(02)	1(04)	1.0	1.98(−08)	–	9.32(−10)	1.77(−08)	–
39	7(02)	4(04)	1.0	2.04(−07)	–	2.24(−08)	4.20(−08)	–
40	7(02)	1(05)	1.0	1.13(−06)	–	1.58(−07)	8.88(−08)	4.04(−11)
41	7(02)	4(05)	1.0	1.16(−05)	–	1.00(−06)	2.80(−07)	5.33(−10)
42	7(02)	1(06)	1.0	3.91(−05)	–	1.24(−06)	5.42(−07)	1.03(−09)
43	2(03)	4(03)	1.0	8.10(−08)	1.16(−08)	2.73(−10)	1.57(−06)	–
44	2(03)	1(04)	1.0	4.75(−07)	2.81(−08)	6.71(−09)	3.60(−06)	2.18(−11)
45	2(03)	4(04)	1.0	4.39(−06)	9.65(−08)	1.63(−07)	8.37(−06)	8.39(−10)
46	2(03)	1(05)	1.0	1.54(−05)	1.88(−07)	6.03(−07)	1.33(−05)	3.61(−09)
47	2(03)	4(05)	1.0	5.21(−05)	3.36(−07)	1.81(−06)	1.61(−05)	5.62(−09)
48	2(03)	1(06)	1.0	7.54(−05)	3.79(−07)	3.12(−06)	1.15(−05)	3.87(−09)
49	4(03)	4(03)	1.0	9.28(−08)	4.93(−07)	7.33(−11)	6.51(−06)	–
50	4(03)	1(04)	1.0	7.16(−07)	1.11(−06)	2.25(−09)	1.82(−05)	1.34(−10)
51	4(03)	4(04)	1.0	5.00(−06)	2.90(−06)	7.67(−08)	2.74(−05)	2.52(−09)
52	4(03)	1(05)	1.0	1.21(−05)	4.09(−06)	3.50(−07)	2.71(−05)	4.99(−09)
53	4(03)	4(05)	1.0	3.09(−05)	3.60(−06)	1.14(−06)	2.01(−05)	2.75(−09)
54	4(03)	1(06)	1.0	4.07(−05)	1.62(−06)	4.57(−07)	7.95(−06)	1.62(−10)

Notation: a(b) $\equiv$ a $\times$ 10^b; A dash (–) indicates that the fractional abundance $< 1(-12)$.

Table 4.4: Results for selected species for models 1–54 at time 10^4 yrs.

Model	T (K)	n_H T (cm^{-3} K)	χ	X(HCN)	X(HNC)	X(C_2H)	X(C_3H_2)	X(CS)
1	7(02)	4(03)	0.1	2.55(−11)	2.88(−11)	1.17(−08)	–	9.37(−11)
2	7(02)	1(04)	0.1	2.36(−10)	8.33(−11)	9.60(−08)	2.16(−11)	6.36(−10)
3	7(02)	4(04)	0.1	6.64(−09)	3.68(−10)	1.39(−06)	1.18(−09)	1.06(−08)
4	7(02)	1(05)	0.1	3.45(−08)	6.55(−10)	3.10(−06)	6.01(−09)	4.07(−08)
5	7(02)	4(05)	0.1	2.18(−07)	1.98(−09)	2.89(−06)	1.80(−08)	8.53(−08)
6	7(02)	1(06)	0.1	9.83(−07)	1.82(−08)	1.97(−06)	2.35(−08)	7.65(−08)
7	2(03)	4(03)	0.1	3.30(−09)	9.32(−10)	1.54(−07)	1.24(−10)	3.66(−10)
8	2(03)	1(04)	0.1	2.57(−08)	2.55(−09)	8.22(−07)	2.06(−09)	2.37(−09)
9	2(03)	4(04)	0.1	5.47(−07)	8.66(−09)	4.15(−06)	2.87(−08)	1.69(−08)
10	2(03)	1(05)	0.1	2.49(−06)	1.61(−08)	7.19(−06)	7.84(−08)	4.35(−08)
11	2(03)	4(05)	0.1	6.56(−06)	2.60(−08)	9.90(−06)	1.90(−07)	1.12(−07)
12	2(03)	1(06)	0.1	7.64(−06)	3.47(−08)	1.07(−05)	2.78(−07)	1.66(−07)
13	4(03)	4(03)	0.1	5.14(−08)	1.75(−09)	8.74(−08)	4.36(−11)	1.61(−10)
14	4(03)	1(04)	0.1	3.65(−07)	5.07(−09)	5.50(−07)	1.26(−09)	1.65(−09)
15	4(03)	4(04)	0.1	2.30(−06)	1.21(−08)	3.02(−06)	2.06(−08)	1.36(−08)
16	4(03)	1(05)	0.1	3.86(−06)	1.38(−08)	5.74(−06)	5.95(−08)	2.58(−08)
17	4(03)	4(05)	0.1	5.39(−06)	2.14(−08)	1.36(−05)	2.07(−07)	4.37(−08)
18	4(03)	1(06)	0.1	7.10(−06)	5.09(−08)	1.52(−05)	3.57(−07)	9.69(−08)
19	7(02)	4(03)	0.3	–	–	9.61(−10)	–	–
20	7(02)	1(04)	0.3	1.72(−11)	2.33(−11)	7.80(−09)	–	6.37(−11)
21	7(02)	4(04)	0.3	4.51(−10)	1.11(−10)	1.67(−07)	4.89(−11)	1.12(−09)
22	7(02)	1(05)	0.3	3.18(−09)	2.48(−10)	7.74(−07)	5.26(−10)	6.31(−09)
23	7(02)	4(05)	0.3	2.41(−08)	4.61(−10)	1.59(−06)	3.41(−09)	3.26(−08)
24	7(02)	1(06)	0.3	6.85(−08)	9.20(−10)	1.12(−06)	5.57(−09)	4.11(−08)
25	2(03)	4(03)	0.3	3.36(−10)	1.97(−10)	1.01(−08)	–	2.90(−11)
26	2(03)	1(04)	0.3	2.03(−09)	6.79(−10)	9.31(−08)	7.27(−11)	3.22(−10)
27	2(03)	4(04)	0.3	3.63(−08)	2.75(−09)	9.15(−07)	2.54(−09)	3.54(−09)
28	2(03)	1(05)	0.3	2.50(−07)	5.58(−09)	2.27(−06)	1.13(−08)	1.13(−08)
29	2(03)	4(05)	0.3	2.85(−06)	1.63(−08)	5.47(−06)	5.55(−08)	4.41(−08)
30	2(03)	1(06)	0.3	4.27(−06)	2.00(−08)	7.73(−06)	1.14(−07)	8.17(−08)
31	4(03)	4(03)	0.3	3.26(−09)	3.05(−10)	4.23(−09)	–	–
32	4(03)	1(04)	0.3	2.92(−08)	1.22(−09)	5.38(−08)	4.47(−11)	1.85(−10)
33	4(03)	4(04)	0.3	5.91(−07)	6.12(−09)	6.89(−07)	2.56(−09)	3.50(−09)
34	4(03)	1(05)	0.3	2.25(−06)	1.14(−08)	1.97(−06)	1.34(−08)	1.12(−08)
35	4(03)	4(05)	0.3	4.50(−06)	1.74(−08)	4.79(−06)	6.46(−08)	3.01(−08)
36	4(03)	1(06)	0.3	5.04(−06)	3.04(−08)	4.28(−06)	6.60(−08)	5.61(−08)
37	7(02)	4(03)	1.0	–	–	4.29(−11)	–	–
38	7(02)	1(04)	1.0	–	–	4.82(−10)	–	–
39	7(02)	4(04)	1.0	2.47(−11)	2.81(−11)	1.15(−08)	–	9.21(−11)
40	7(02)	1(05)	1.0	1.91(−10)	7.43(−11)	7.95(−08)	1.74(−11)	5.83(−10)
41	7(02)	4(05)	1.0	2.08(−09)	1.85(−10)	4.74(−07)	3.45(−10)	5.48(−09)
42	7(02)	1(06)	1.0	6.18(−09)	2.75(−10)	5.68(−07)	8.86(−10)	1.23(−08)
43	2(03)	4(03)	1.0	2.74(−11)	2.01(−11)	1.45(−10)	–	–
44	2(03)	1(04)	1.0	1.72(−10)	1.10(−10)	3.58(−09)	–	1.31(−11)
45	2(03)	4(04)	1.0	2.15(−09)	6.43(−10)	8.94(−08)	6.35(−11)	3.61(−10)
46	2(03)	1(05)	1.0	1.15(−08)	1.43(−09)	3.33(−07)	4.96(−10)	1.57(−09)
47	2(03)	4(05)	1.0	1.23(−07)	3.54(−09)	1.00(−06)	3.19(−09)	6.83(−09)
48	2(03)	1(06)	1.0	6.33(−07)	7.38(−09)	1.74(−06)	9.17(−09)	1.57(−08)
49	4(03)	4(03)	1.0	1.29(−10)	2.97(−11)	3.90(−11)	–	–
50	4(03)	1(04)	1.0	1.31(−09)	1.57(−10)	1.20(−09)	–	–
51	4(03)	4(04)	1.0	2.93(−08)	1.16(−09)	4.18(−08)	3.17(−11)	2.41(−10)
52	4(03)	1(05)	1.0	1.67(−07)	3.12(−09)	1.95(−07)	3.50(−10)	1.21(−09)
53	4(03)	4(05)	1.0	8.97(−07)	7.88(−09)	6.63(−07)	2.35(−09)	6.14(−09)
54	4(03)	1(06)	1.0	4.05(−07)	6.09(−09)	2.90(−07)	3.41(−10)	5.68(−09)

Notation: a(b) $\equiv$ a $\times$ 10^b; A dash (–) indicates that the fractional abundance $< 1(-12)$.

CHAPTER 5

X–ray Ionization and the Formation of Doubly Ionized Atoms

X–rays have a rather localized influence, but may affect the chemistry in interfaces occurring near stars and other radiation sources, which necessarily, have a relatively small spatial extent. It would be valuable to identify a specific tracer indicating that X–rays were present in a particular *interface* region. Therefore, in this chapter we simulate the effects of a nearby or embedded x–ray source on a cloud by modelling a dark cloud, assuming an enhanced temperature and an ionization rate greater than that attributed to cosmic–rays alone. We also include the production of C^{++} in the chemistry network. We find that the detection of large enhancements in the abundances of species such as CH, CN, OH and NO would provide evidence for the presence of a x–ray source not directly detectable. We also predict that the formation of C^{++} would significantly enhance the production rate of CH^{+}.

5.1 Introduction

There are a number of x–ray sources in the galaxy, and these sources have been observed to lie within or adjacent to interstellar molecular clouds. Examples of

observed sources include the Orion Nebula (Long and White, 1980) and Eta Carinae (Seward and Chlebowski, 1982). X–rays are also produced within clouds from shocks with velocities greater than 100 kms^{-1}, stellar winds, a supernova explosion or from the degradation of gamma rays emitted from radioactive decaying material. The presence of x–rays can have a number of effects on the ambient gas, including heating and ionizing, which can lead to the detection of x–ray signatures in the cloud.

Dalgarno (1976*a*) was the first to suggest that the presence of x–rays near or in a cloud could have an effect on its chemistry. He proposed an alternative method to the production of CH^+, thereby enhancing the fractional abundance of the molecule and providing a possible solution to the CH^+ problem (as discussed in Chapter 4). Dalgarno (1976*a*) noted that in the vicinity of a x–ray source, doubly charged ions could be formed.

The doubly charged ion is formed when a high energy x–ray ionizes an atom by removing one of the inner shell electrons. The ionized atom, now in an excited state, would rapidly decay when an electron moves into the ground state, while at the same time emit one or more electrons (Lepp and Tiné, 1998). This process is known as the Auger Process.

Once the C^{++} forms, it would readily react with H_2 and form CH^+ via the reaction sequence,

$$C^+ + \text{cosmic} - \text{ray} \longrightarrow C^{++} + e^- \tag{5.1}$$

$$C^{++} + H_2 \longrightarrow CH^+ + H^+ \tag{5.2}$$

In many of the studies made to date, the presence of x–rays is simulated by artificially and simultaneously enhancing the ionization rate and gas temperature above the standard values. Krolik and Kallman (1983) made a study of the dependence of the fractional abundance of different molecules on the ionization rate. They found that an enhanced ionization rate attributed to the presence of x–rays could cause

high abundances, not seen in standard models, in species such as CN, C_2H and HC_3N. They argue that their abundances are so sensitive on the ionization rate that their presence could be due largely on the presence of x–rays, although an enhanced ionization rate does not have a positive effect on the abundance of all species. For example, the abundance of molecules such as CO and HCO^+ are seen to decline as ionization rate increases.

A more recent study of the effects of x–ray ionization on the cloud chemistry was made by Lepp and Dalgarno (1996), who made steady state chemical calculations over a wide range of ionization rates. They predict high fractional abundances of CN and NO and a sharp decline in the abundance of HCO^+. Other molecules which are enhanced by x–rays include OH, CH and HCN. Lepp and Dalgarno (1996) found a correlation of the species abundances with the $n_H/n(H)$ ratio. The steady–state abundances of the enhanced species are seen to fall off rapidly after the value of ζ/n_H (ζ is the ionization rate where $1\zeta = 1.3 \times 10^{-17}$ s^{-1} is the standard interstellar value) reaches a value of approximately 2×10^{-18} cm^{3}s^{-1}. It is around this point that the $n_H/n(H)$ ratio falls through unity.

In molecular clouds, H_3^+ drives the chemistry and is formed from the ionization of H_2, producing $H_2{}^+$ which reacts with another H_2 molecule to form H_3^+ (see in equations 1.3 and 1.4). Therefore as the chemistry proceeds there is a constant removal of H_2 from the gas. This effect is accentuated by x–rays due to the increased ionization rate, producing a gas which is mainly atomic rather than molecular. This situation favours the production of simple molecules. As the abundance of H_2 decreases, the formation reactions requiring H_2 becomes less efficient. The dissociative effect of x–rays also causes the enhancement in abundance seen in some of the molecules (e.g. OH and CH). CO and N_2 become dissociated more rapidly under these conditions, producing free atoms which are used in the formation of these simple diatomic molecules.

Table 5.1: Parameter set for grid of models.

Parameter	Range of Values
ζ (s^{-1})	1, 10, 100, 10^3, 10^4, 10^5, 10^6
T (K)	250, 500

The predicted decline in HCO^+ abundance has been inferred from observations made by Phillips and Lazio (1995). Using the Owens Valley mm–wave interferometer, they made observations of the x–ray source 1E1740.7-2942, which showed that the HCO^+ (1-0) line intensity was lower than expected. The authors suggested that the observed enhanced destruction or suppressed formation of HCO^+ was due to its proximity to the ionizing flux produced from the x–ray source.

It is hoped that from the modelling, tracers of x–ray ionization may be identified and used as a signal of stellar x–ray emission, which would otherwise be too faint or too deeply buried in clouds to be detected using x–ray telescopes. In this chapter, we describe the modelling of x–ray ionization and include the formation of doubly ionized carbon. In §5.2 we describe the different model conditions studied. The results are given in §5.3 and conclusions are made in §5.5.

5.2 Model Calculations

In order to study the effects of x–ray ionization on the gas chemistry, we made a grid of 21 calculations assuming varying physical conditions. The calculations were halted once the fractional abundances of the species reached a steady–state value. We assumed initial elemental abundances appropriate to dark clouds (taken from Table 1.2), the number density of H nuclei, $n_{\rm H}$, is assumed to be 10^4 cm^{-3} and the visual magnitude is assumed to be 10. The varying parameter set for the grid of models is given in Table 5.1.

5.3 Results and Discussion

To ease the comparison of results obtained with those from previous studies, the results from the seven different models (for a given temperature) were compiled together and put in the form of of $\log(X_i)$ vs. $\log(\zeta/n_{\rm H})$ plots. (N.B. when considering the effects of x–rays, plots of molecular abundance are generally of the form $\log(X_i)$ vs. $\log(\zeta/n_{\rm H})$. This is because the main reactions are either x–ray ionization reactions, with rates proportional to $n_{\rm H}\zeta$ or are two particle reactions with rates proportional to ${n_{\rm H}}^2$. Division of $n_{\rm H}\zeta$ by ${n_{\rm H}}^2$ leaves $\zeta/n_{\rm H}$ as the only free parameter (Lepp and Tiné, 1998)). Steady–state fractional abundances of the models for a selection of species are given in Fig. 5.1 and 5.2 for $T = 250$ K and Fig. 5.3 and 5.4 for a gas temperature of 500 K.

Firstly consider the results for models at $T = 250$ K. The results seem to follow previous predictions. The abundances of a number of different species are seen to be significantly enhanced by the increased ionization rate. There is a large 'bump' in the fractional abundance plots for species including C, CH, CH^+, CN, OH, C_2H, NH and NH_2. The abundances are predicted to be enhanced by at least two orders of magnitude. X–rays are seen to also enhance the abundances of NO, HCN, HC_3N and C_2H_2, although not to the same extent.

However, the presence of x–rays has a counterproductive effect on the abundances of species including CO and N_2, which are readily dissociated due to the higher ionization rates. The free atoms C, O and N are used to produce simple molecules, thereby causing the enhancement in abundances seen in species such as CN and NO.

As noted by Lepp and Dalgarno (1996), the abundances of all species are seen to rapidly decrease once the $n_{\rm H}/n({\rm H})$ ratio falls below unity. This occurs at a $\zeta/n_{\rm H}$ value of $\sim$ few$\times$ 10^{-17} $\rm cm^3 s^{-1}$. This is due to the dramatic reduction in the ion, H_3^+, which is normally used to drive the chemistry in dark clouds (as described in §1.4.1.1). As expected, the abundance of H_3^+ drops dramatically in correlation with

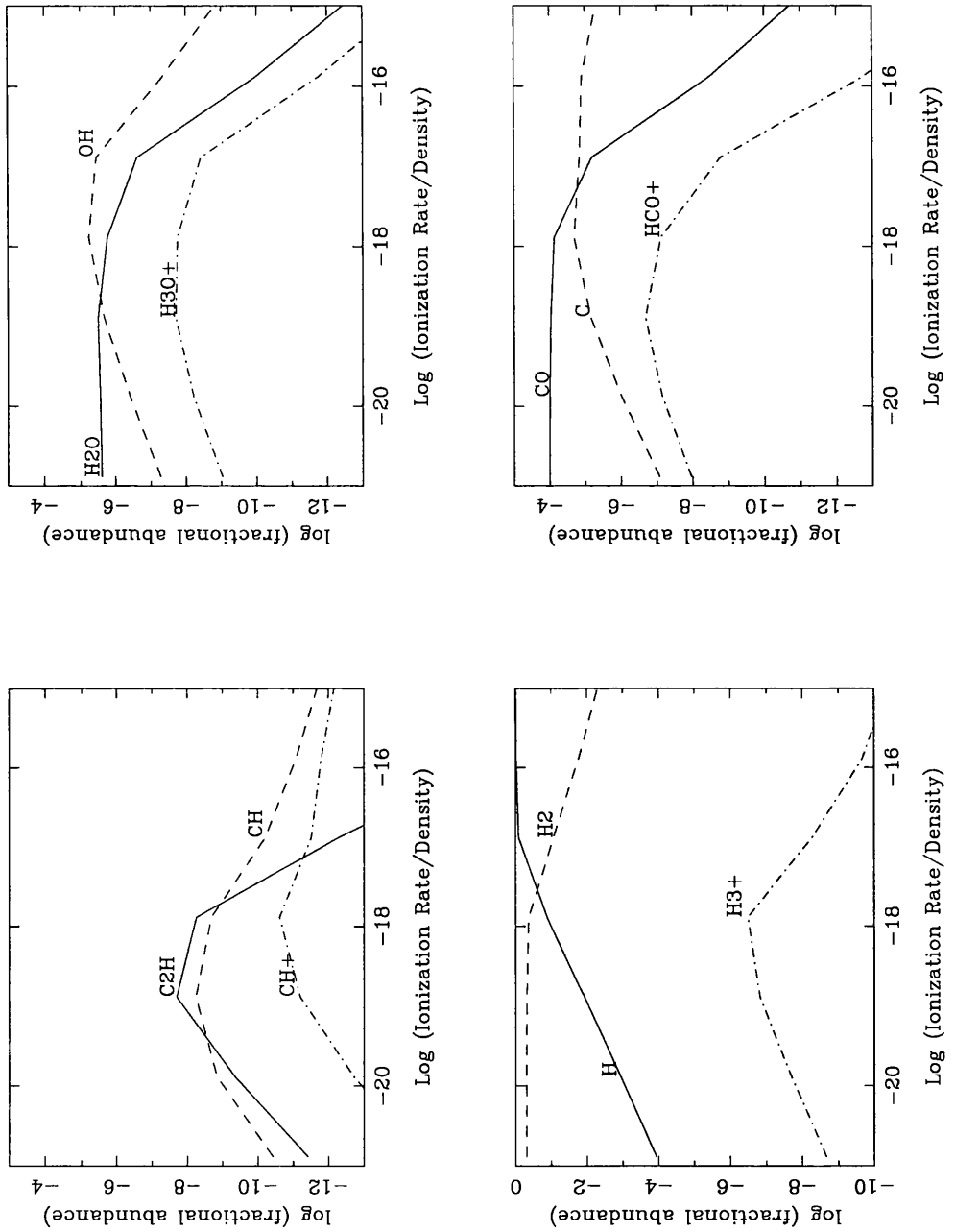

Figure 5.1: Variation in fractional abundance for a selection of species with $\zeta/n_{\rm H}$ (cm^3 s^{-1}) for models with $T = 250$ K

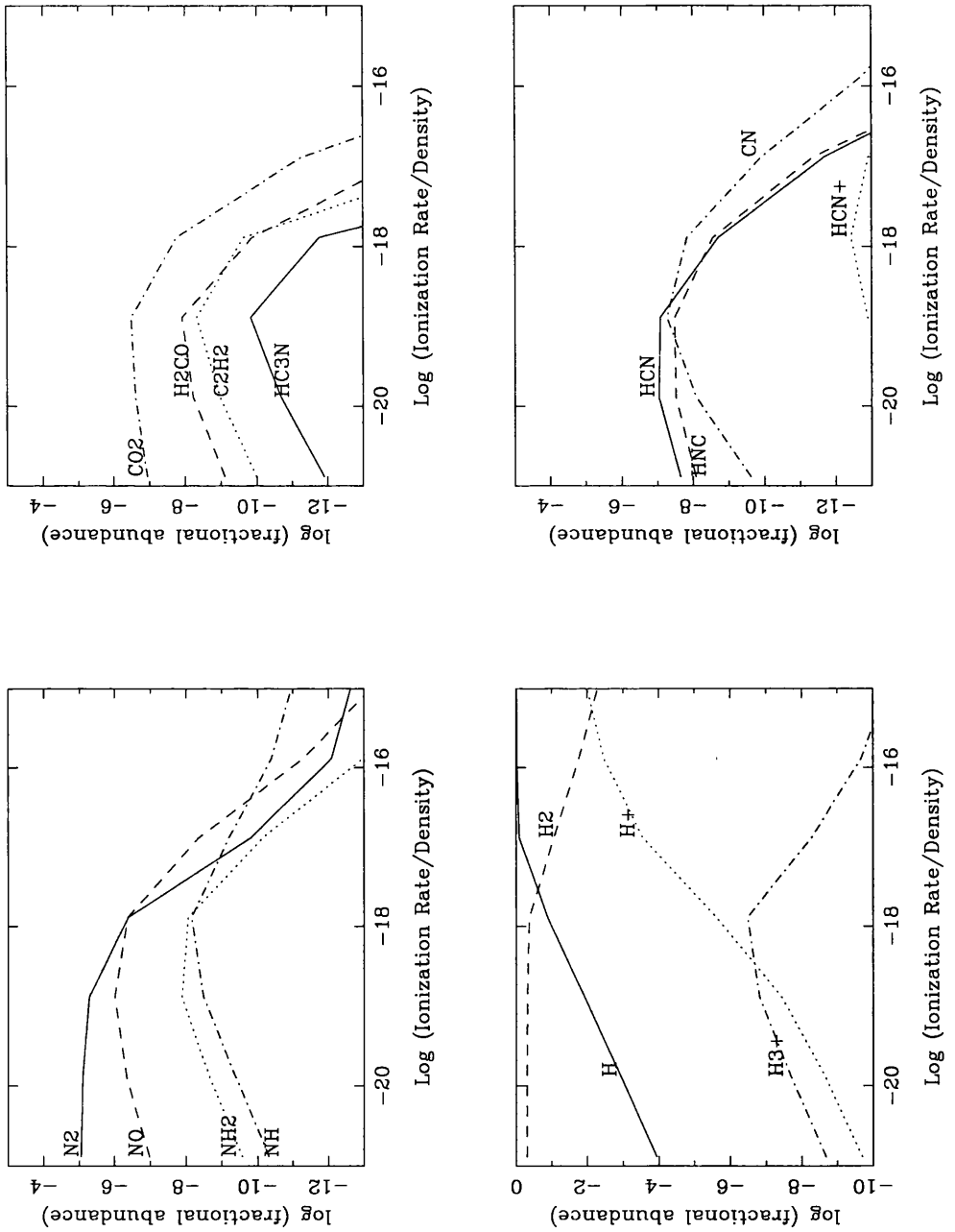

Figure 5.2: Variation in fractional abundance for a selection of species with $\zeta/n_{\rm H}$ (cm^3 s^{-1}) for models with $T = 250$ K

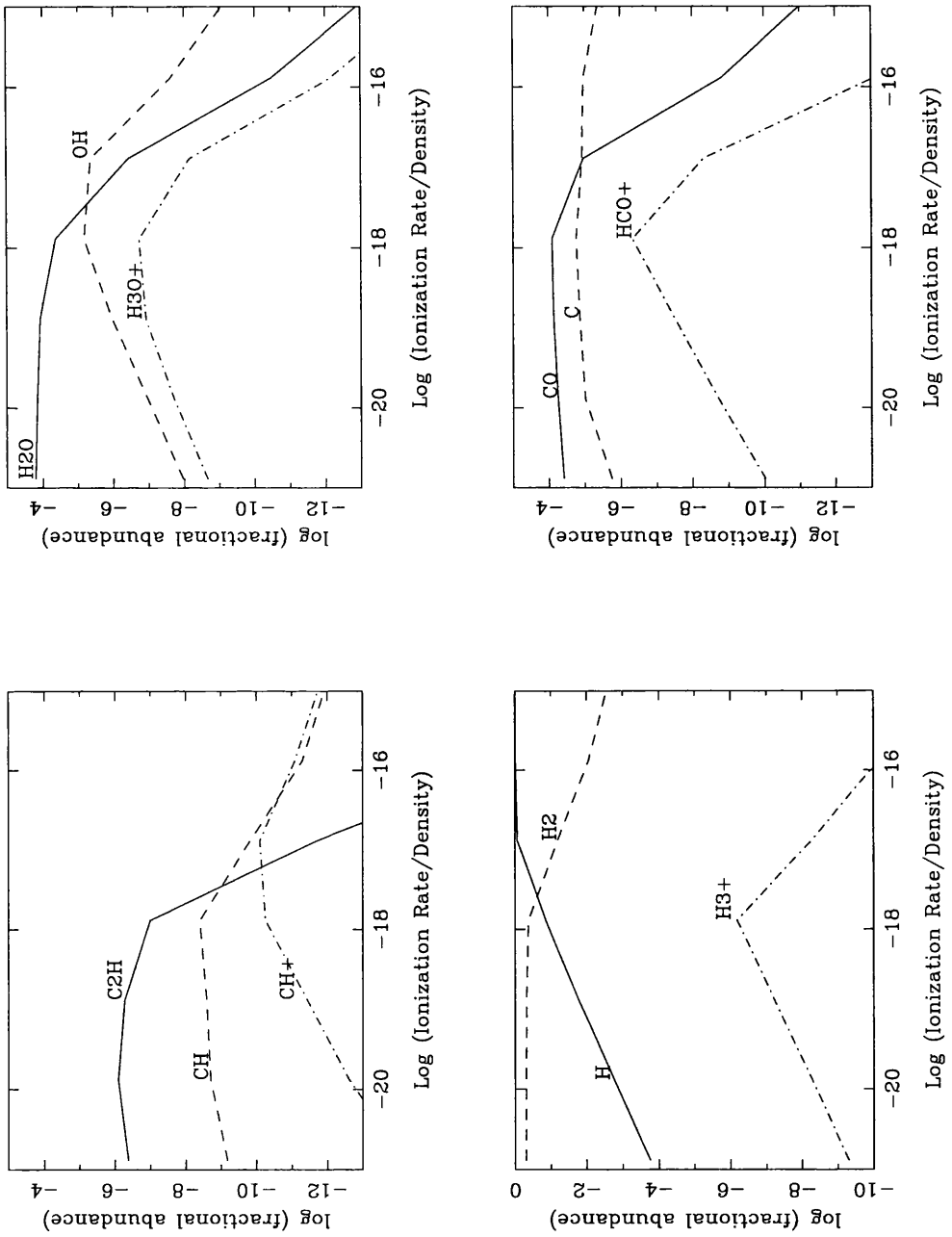

Figure 5.3: Variation in fractional abundance for a selection of species with $\zeta/n_{\rm H}$ (cm^3 s^{-1}) for models with $T = 500$ K

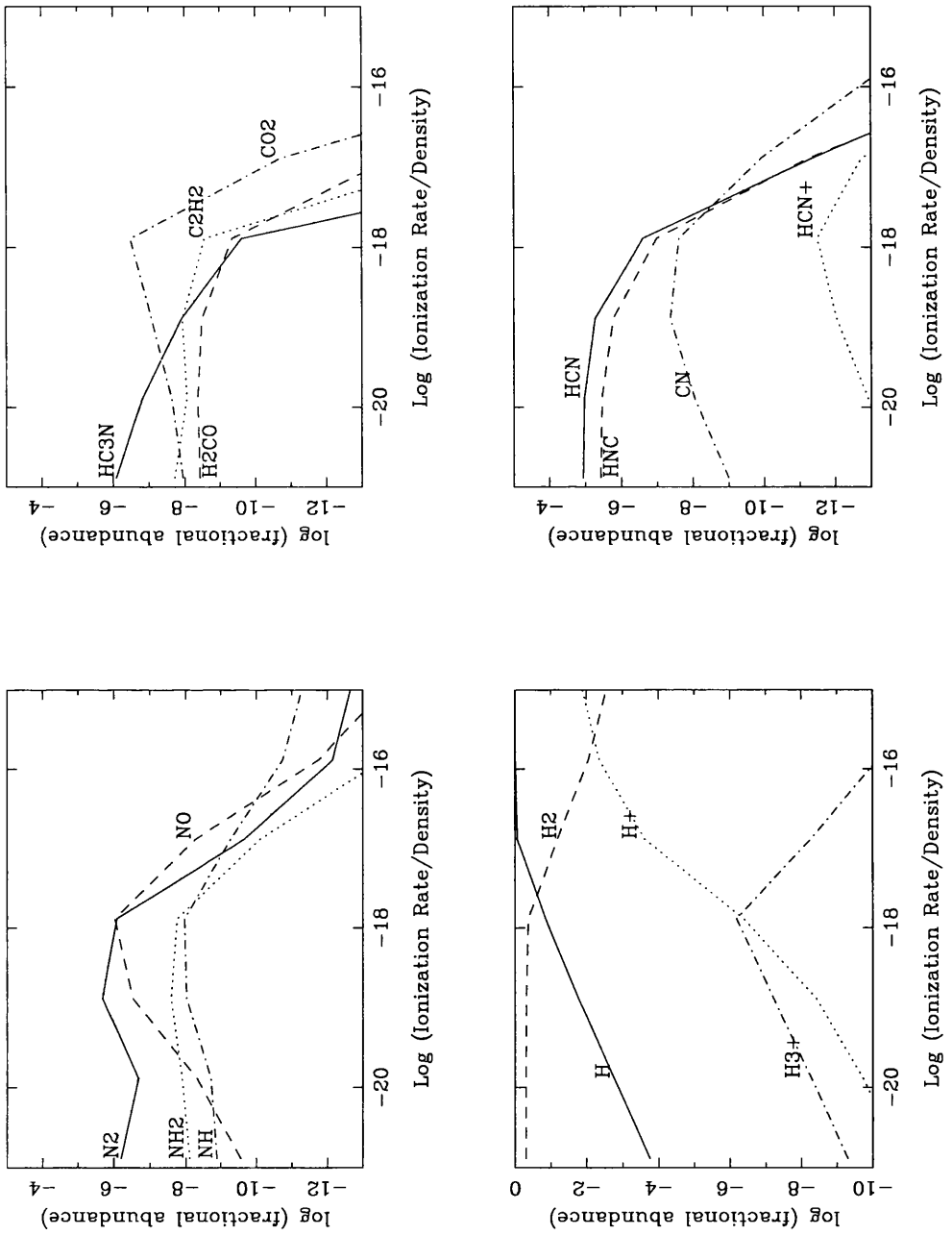

Figure 5.4: Variation in fractional abundance for a selection of species with $\zeta/n_{\rm H}$ (cm^3 s^{-1}) for models with $T = 500$ K

the reduction in the $n_H/n(H)$ ratio.

For the $T = 500$ K case, the tracers of x–ray ionization identified for the 250 K case are no longer appropriate. For temperatures of 500 K, CH does not show the predicted pronounced bump in the abundance profile seen in the 250 K case. The enhancement in abundance of CN has also fallen slightly. We now find that suitable tracers are NO, OH and CH^+. NO is enhanced by almost four orders of magnitude and OH is increased by almost three orders. There is also a large enhancement in the abundance of HCN^+, but this species would not be a valuable tracer as the enhanced abundance is not great enough to make it easily observable. At higher temperatures, very few species show the bump in abundance profile that indicates an enhancement due to the increased ionization rate, but many species do show an overall increase in abundance at low ionization rates compared to the models at 250 K. Such species include C_2H, HCN and HNC, which all show significantly larger fractional abundances at low ζ values. This is due to the higher temperatures driving endothermic reactions, which are inefficient at low temperatures. Another effect of the increased temperature is that the $n_H/n(H)$ ratios falls below unity at a lower value of ζ/n_H than for the 250 K models, therefore the fractional abundances of all species, regardless of their robustness, will also fall off at a lower value of ζ/n_H.

One surprising result from the models, is the fact that HCO^+ is seen to be significantly enhanced at high ionization rates. In all previous models, x–rays are predicted to have a destructive effect on the abundance of HCO^+. However, it should be noted that previous models assumed lower gas temperatures, and the 500 K case has not been modelled before. The heating produced from the x–rays may not in fact increase the temperature of the gas to such high levels.

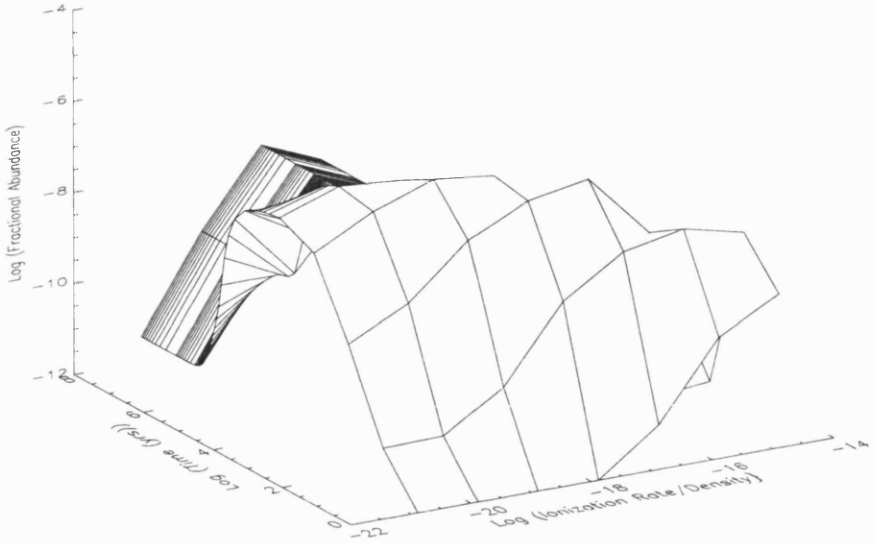

Figure 5.5: Variation in fractional abundance of C_2H with ζ/n_H ($cm^3\ s^{-1}$) and time for models with $T = 250$ K

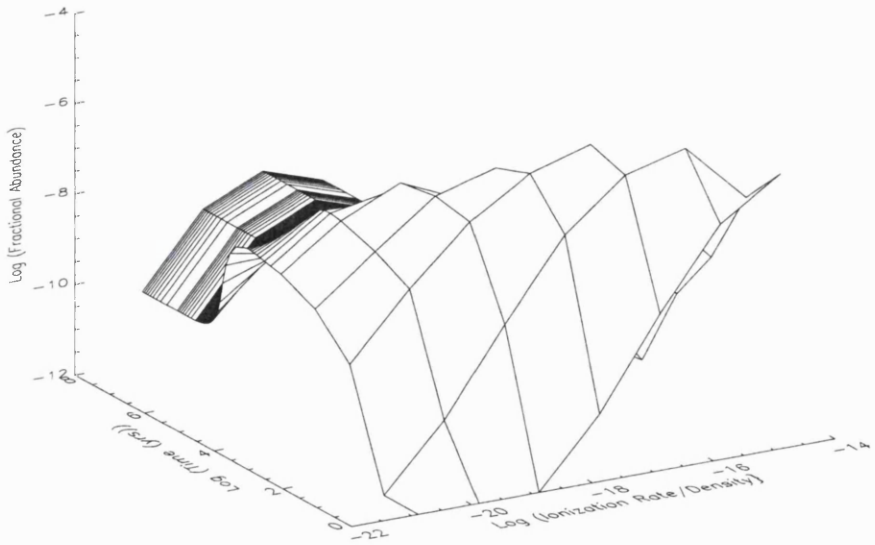

Figure 5.6: Variation in fractional abundance of CH with ζ/n_H ($cm^3\ s^{-1}$) and time for models with $T = 250$ K

5.3.1 Time–dependent Effects

We also studied the time–dependent effects of x–rays on the abundances of species. Three–dimensional plots of the variation of fractional abundances of C_2H and CH, with $\log(\zeta/n_H)$ and time are given in Fig. 5.5 and 5.6 respectively. From the figures, it can be seen that there is an early time peak in abundances at a time of about 10,000 years.

We discuss only the case of C_2H and CH, as an example of the kind of results obtained. In these two cases, the predicted early time peak can be explained by considering the destruction routes of the species. The main destruction route involves reactions with H^+, H_2^+, H_3^+ and C^+, but at early times hydrogen is molecular and carbon is mainly neutral. The destruction routes of C_2H and CH are suppressed until the abundances of the destructive ions reaches a sufficient level that the destruction processes become efficient.

For C_2H, the early time fractional abundance is $\sim 4 \times 10^{-7}$, whereas the steady–state value is 2×10^{-8}. For CH, the early time fractional abundance is $\sim 2 \times 10^{-7}$, and the steady–state value is 5.5×10^{-9}. This early time peak is not seen in many species, although an enhancement is also predicted to occur for CH^+, with an early time abundance $\sim 3 \times 10^{-10}$, and steady–state value being 2.5×10^{-11}. If detections of these very high fractional abundances are made, the results could be used as a chronometer for the age of the region.

5.4 Formation of Doubly Ionized Carbon

As previously discussed, x–rays are predicted to produce doubly ionized atoms. In this section, we have included five new formation and destruction routes for C^{++} into the chemical reaction ratefile. The new reactions are given in equations 5.4-5.7. The same grid of models as before (given in Table 5.1) were calculated. We will concentrate our discussion of the effect which the presence of X–rays and C^{++} has

on the fractional abundance of CH^+.

$$C^+ + \text{cosmic} - \text{ray} \longrightarrow C^{++} + e^- \qquad \alpha = 2.3(-16); \beta = 0.00 \tag{5.3}$$

$$C^{++} + H_2 \longrightarrow CH^+ + H^+ \qquad \alpha = 1.0(-09); \beta = 0.00 \tag{5.4}$$

$$C^{++} + e^- \longrightarrow C^+ + h\,\nu \qquad \alpha = 1.0(-11); \beta = -0.61 \tag{5.5}$$

$$C^{++} + H_2 \longrightarrow C^+ + H_2^+ \qquad \alpha = 2.0(-09); \beta = 0.00 \tag{5.6}$$

$$C^{++} + H_2 \longrightarrow C^+ + H^+ + H \qquad \alpha = 2.0(-09); \beta = 0.00 \tag{5.7}$$

The notation $a(b) \equiv a \times 10^b$.

We find that at low ζ values, there is no change in the abundance of CH^+ because the ionization level is insufficient to produce a large enough abundance of C^{++} to significantly alter the production of CH^+, whereas at higher ζ values the effects become quite noticeable. The fractional abundance values of CH^+, using the original chemistry ratefile (at 250 and 500 K), and the corresponding values for the modified chemistry ratefile are given in Table 5.2. From the results it can be seen that at very high ionization rates, the fractional abundance of CH^+ is enhanced by at least two orders of magnitude. Although the CH^+ abundances are low in this scenario, there will be few other species with significant abundances.

However, it should be noted that the reaction network involving C^{++} included into the ratefile is far from complete and a more thorough examination of the network could provide more realistic results. Even from this crude model, it is found that the formation of doubly charged atoms can have a significant effect on the cloud chemistry and therefore must be more carefully studied and included into future models of regions with high ionization levels. As was proposed by Dalgarno (1976*a*), the presence of C^{++} does enhance the production rate of CH^+, and a more detailed study of x–ray ionization in diffuse regions might provide a solution to the CH^+ problem described in Chapter 4.

Table 5.2: Variation in the fractional abundance of CH^+ due to the formation of C^{++}

	Steady–state fractional abundance values of CH^+			
ζ (s^{-1})	T = 250 K		T = 500 K	
	Standard Model	C^{++} Included	Standard Model	C^{++} Included
10(4)	3.1(−12)	6.7(−12)	7.9(−11)	8.4(−11)
10(5)	1.6(−12)	2.6(−11)	8.3(−12)	3.8(−11)
10(6)	6.1(−13)	1.6(−10)	1.5(−12)	1.8(−10)

The notation a(−b) ≡ a × 10^{-b}.

5.5 Conclusions

From the models, it has been determined that certain molecules including CH, CN, OH, NO, NH and NH_2 could be used as signatures for the presence of a nearby or embedded x–ray source in the cloud. The large enhancement in their abundances caused by x–rays would make them easily observable. A few species such as HCN^+ also show significant abundance increases with ζ values, but even at their enhanced values, the predicted fractional abundances would make their detection still difficult.

We also find that the abundances are very sensitive to the temperature of the gas. At higher temperatures, the tracers for x–ray emissions are different from those for the 250 K case. At these higher temperatures, there is a smaller selection of molecules which show large enough abundances and a sufficient enhancement to make them suitable tracers, but these do include NO, OH and CH^+.

For a small selection of molecules (e.g. CH, CH^+ and C_2H) the variation of their fractional abundance with time could provide a useful chronological tool in determining the age of the region being studied. We find a large increase in the abundance values of these molecules at a time of approximately 10^4 yrs., compared to their steady–state values. The enhancement can be up to two orders of magnitude.

Finally, when we include the formation and destruction of C^{++} into the reaction

network, we find that there is a significant effect on the CH^+ abundance at high ζ values. The abundance of CH^+ can be enhanced by over two orders of magnitude, although from a very low level. Further work into this area would need to consist of a more comprehensive network of formation and destruction routes of doubly ionized atoms and a more detailed study of the temperature effects would also produce a more accurate model of x–ray ionization.

CHAPTER 6

Photodissociation Region in the Vicinity of a Circumstellar Disk

Circumstellar disks around newly–formed stars are well defined regions of cold and very dense gas. The chemistry of such disks has been well studied in theoretical models. However, the *interface* of such disks with the high radiation environment in which they are embedded creates an interesting region which could potentially provide information about the lifetime of the disk. Material evaporating from the disk can be gravitationally trapped so that a kind of photon–dominated region (a PDR, also known as a photodissociation region) can arise. In this chapter we explore the chemistry in a PDR/disk system to examine the contribution that a PDR may make to the molecular species that may be observed. We compute the column densities of species through the PDR/disk system, averaged over the disk. For the case where the central star has a high stellar mass, our results are in good agreement with the observations which are available, and we predict that detectable species should include CO, C_2H_2, CH_4, HCN, NH_3 and CS. We find that potential tracers of disks around low mass stars irradiated by nearby massive stars include OH, CH_3 and C_2H. We note that the detection in a disk of PDR–type chemistry would be a

clear signature that the disk is undergoing erosion. Its duration would therefore be limited, with consequences for planet formation.

6.1 Introduction

Circumstellar disks around young stars, the new material of future planetary systems, have been the subject of much research in recent years. However, observations of these disks are not easy due to confusion with foreground and background gas and their complex geometry. Nevertheless, the Hubble Space Telescope (HST) has provided strong dynamical evidence of the existence of extended circumstellar disks around many low mass young stars (e.g. Bally *et al.*, 1998), and there is also evidence that disks are present in OB associations (O'Dell, 1998, and references therein) as well as around massive stars (Mitchell *et al.*, 1989; Carr *et al.*, 1995).

Radio and IR observations of molecular abundances in circumstellar disks can reveal the chemical connection between planetary and interstellar matter. Furthermore, the sizes of disks are still not well determined: the knowledge of the molecular abundances at different radii of a disk may be helpful in determining its geometry. Dutrey *et al.* (1997) reported molecular emissions from disks around the low mass T–Tauri stars DM Tau and GG Tau and inferred that the disk may extend to $\sim$ 800-1000 AU. They also find diversity in the chemistry: some of the detected species are under abundant with respect to dark cloud abundances by factors of 5 to 30, indicating that depletion on to grains is occurring, while large ratios of C_2H/HCO^+ and CN/HCN are indicative of photo–dominated chemistry.

It is likely that disks are flared, allowing them to absorb more of the radiation from the central star at large radii than possible for a flat disk. This would result in the formation of a layer of warm gas and dust at the surface of the disk (Chiang and Goldreich, 1997). Goldsmith *et al.* (1999) also noted that some emission must occur from the surface layers of flared disks: from observations of methanol, they

infer that gas species are desorbed from the grains in these layers while retained on the icy mantles in the midplane region of the disk. Such observations indicate that substantial chemical processing, desorption and depletion, occurs in the evolution of disks surrounding low mass stars.

Extended radio emission has been observed in the Trapezium region of the Orion OB association. This emission is thought to be produced by photo–evaporation of the surface of disks surrounding low mass stars (Johnstone *et al.*, 1998). Photo–evaporation via ultraviolet photons could be a very efficient mechanism for the removal of disks and an important factor in any subsequent planetary formation. Given a strong enough UV field, the disk surface can be heated to temperatures in excess of 1000 K, and over most of the disk the gas material becomes gravitationally unbound. Even if the central star is of low mass a disk may be exposed to a strong UV radiation field from an external nearby massive star. External radiation from an OB association in the vicinity of the disk would evaporate circumstellar disks much faster than the radiation field of the central low mass star, consistent with the timescales required for solar–type systems (Johnstone, 2000). However, disk material sufficiently close to the central star in either case will remain gravitationally bound to the system. The radius at which the heated material is no longer bound by gravity is called the critical gravitational radius, r_g. Within this radius the evaporated but gravitationally bound material creates an extended photon–dominated zone, i.e. a PDR. The potential chemical role of this PDR is the subject of this chapter.

Although disks surrounding low mass stars are more common, there is evidence that disks can also survive around young massive stars. Mitchell *et al.* (1989) reported detection of circumstellar CO from the infrared source GL 2591, a $10M_{\odot}$ young stellar object (YSO) (van der Tak *et al.*, 1999). This object is thought to have an optically thick dust shell. The CO detected by Mitchell *et al.* (1989) shows a

variety of structures and gas properties, and in particular they deduce the presence of a hot gas (T $\sim$ 1000K) at the surface of the disk. Carr *et al.* (1995) extended the study of GL 2591 to include other species. Their analysis indicates that most of the emission arises in gas at $\sim$ 200 and 1000 K, corresponding to the components observed by Mitchell *et al.* (1989). They propose a scenario where grains play a passive role. During the star formation process, molecules freeze on to grains, which are then released after the star is formed, by direct heating of the dust by the star, by photo–desorption or other mechanism.

From this limited, yet convincing, set of observations, it is clear that disks may extend up to $\sim$ 1000 AU, still moving in Keplerian motion around the central star and that molecular emission may arise from different components of the disk.

Detailed chemical models are required to help interpret these results. Although the majority of the early models dealt only with the midplane region (Aikawa *et al.*, 1997, 1998), recent models by Aikawa and Herbst (1999) and Willacy and Langer (2000) have taken into consideration the chemical distribution in all layers of the disk from the midplane to the surface layers. Willacy and Langer (2000) find that the UV radiation from the central source is important in driving the chemistry. They also infer that the observed emission comes from a layer below the surface where UV photons can still penetrate sufficiently to drive desorption but molecules are shielded to a certain extent from photodissociation. However, their models do not incorporate an extended PDR within the critical gravitational radius created from evaporated yet gravitationally bound gas. Two–dimensional models of a low stellar mass system have also been made by van Zadelhoff *et al.* (2001). The authors modelled their molecular line emissions in order to derive the density and temperature structures of the disk.

In this chapter we investigate a model in which a circumstellar disk is being heated by a strong radiation field from a massive star that may be the central object

in the disk, or nearby. Within the critical radius, r_g, the heated gas is trapped at the surface of the disk (Johnstone, 2000), in effect creating a photon dominated region (a PDR), while outside this region the disk is being photo–evaporated. PDRs have a characteristic chemistry caused by the influence of the radiation field on the dense and warm molecular gas. We shall explore the chemistry in a PDR associated with a circumstellar disk undergoing photo–evaporation. Our intention is to identify molecular tracers of disks in this destructive phase of their evolution, from the gas that is trapped in the PDR. The model predictions will be compared with the rather limited observational data for GL 2591, a candidate high mass object for a photo–evaporating object that should include a PDR. Predictions of potentially observable species, as yet undetected, arising in the eroding PDR/disk system are also made.

Disks around low mass stars are much more numerous than those associated with high mass stars. Such disks will incorporate a PDR when irradiated by a nearby massive star. In such a case, the PDR may provide molecular signatures of the late evolutionary stage of a disk around a low mass object. Therefore, we shall also consider PDRs arising in disks around a low mass star, where the radiation source is assumed to be a nearby massive star. Such systems have been proposed by Johnstone *et al.* (1998), and in this study we show that potential molecular tracers can be identified.

A brief discussion of methods for disk dispersal is given in §6.2. The model is described in § 6.3. A comparison with observational results for GL 2591 is given in § 6.4, and some predictions of other potentially detectable species in disks around massive stars are given in § 6.5. Predictions of molecular tracers of eroding disks around low mass stars are given in § 6.6. A brief conclusion is presented in § 6.7.

6.2 Disk Dispersal

Strom (1995) deduced that the dust in the inner disks around low mass stars is dispersed in about 10^7 yrs., whereas for intermediate mass stars, this timescale is somewhat shorter. In this section we will concentrate on the possible methods for the dispersal of such disks.

Four different methods for disk dispersal have been proposed, (i) accretion of material onto the central source (ii) stripping of material due to close encounters (iii) removal of material from stellar or disk winds and (iv) photoevaporation of disks from a UV radiation source (Hollenbach *et al.*, 1994; Johnstone *et al.*, 1998; Storzer and Hollenbach, 1999; Hollenbach *et al.*, 2000).

6.2.1 Disk Accretion

The transport of angular momentum radially outwards allows disk material to flow inwards, onto the central object. The angular momentum transport can be transported by, for example, turbulence or magnetic fields. Considering viscous disks, the viscosity timescale is given by,

$$t_\nu = \frac{r^2}{\nu} \tag{6.1}$$

where ν is the viscosity parameter (Shakura and Sunyaev, 1973). It is found that as the viscosity spreads radially outwards (by the conservation of angular momentum), the accretion rate onto the central object decreases and accretion becomes an inefficient mechanism for disk dispersal (Johnstone, 2000).

6.2.2 Close Encounters by Nearby Stars

Extensive studies have been made to determine the effect that a close encounter of a star would have on a disk (Clarke and Pringle, 1993; Heller, 1995; Hall and Clarke, 1996). It was found that only very large disks would be significantly dispersed on the timescales being considered.

6.2.3 Stellar and Disk Winds

During and after the collapse phase of a cloud, which builds up the disk mass, the disk accretes material onto the central object and creates a strong wind. This strong wind is produced by the interaction of the rotating magnetic field with the inner disk (Shu *et al.*, 1988; Konigl, 1995). This method of disk dispersal was proposed by Cameron (1973) and Horedt (1978, 1980). Johnstone (2000) calculated the effectiveness of this method and found that it was only efficient for very thin disks.

6.2.4 Photoevaporation

The surface of a disk can be efficiently evaporated if it is heated to temperatures such that the average thermal speeds of atoms or ions are comparable to the escape speed of the gravitational potential. Present theories predict that the UV radiation from a massive central object in a disk/star system or from a nearby massive star would be sufficient to evaporate the disk material.

6.2.4.1 Photoevaporation by a Central Star

The UV flux from the central star of a massive star/disk system would be able to heat the disk surface to temperatures of the order 100-3000 K depending on the magnitude of the flux and the density of the gas. Two main scenarios have been described for such a system: (i) a weak stellar wind case and (ii) a strong stellar wind case (Johnstone, 2000).

For the weak stellar wind case, the UV radiation would create a bound envelope above the disk surface for $r < r_g$, where the height of the envelope is equivalent to the scale height. In the strong wind case, the ram pressure from the stellar wind would be too high for the envelope to achieve a full scale height above the disk. The stellar wind suppresses the height of the PDR envelope.

In both cases, for $r > r_g$ the material becomes unbound and the material evaporates off the disk surface as a disk wind, which gives the required photoevaporative mass loss.

6.2.4.2 Photoevaporation by an External Source

Low mass stars have insufficient UV flux to cause a photoevaporative flow. Instead, the low mass star must lie near massive stars, which would illuminate the disk surface with the required intense radiation. In contrast to photoevaporative flows caused by a central star, where the mass loss is concentrated in the inner regions ($r \sim r_g$, i.e. the region closest to the UV radiation source), the photoevaporative flow for an externally illuminated disk is concentrated in the outer region ($r \sim r_d$, where r_d is the disk radius), where most of the surface area lies.

The overall effectiveness of each dispersal method depends on the region of the disk. The viscous timescale is seen to be dominant in the inner region, whereas the stellar encounter lifetime is clearly only important in the outer regions. The photoevaporation timescale is dominant in the intermediate regions and stellar wind stripping is found to be not effective at all (Hollenbach *et al.*, 2000).

6.3 Model Calculations

Our model follows the time–dependent chemical evolution of the envelope of a disk at different radii (r) from the central object out to a critical radius, r_g. Beyond r_g, the envelope is no longer gravitationally bound, and we do not consider the chemistry in that zone. Our model is two–dimensional in that we compute the time–dependent chemical evolution as a function of r and of z, the distance from the central plane of the disk. The driving source of the PDR envelope is either from the central star, in the case of a massive YSO, or from an external massive star or stars, as in the

case of disks surrounding low mass stars in OB association, such as the Trapezium in Orion.

The radiation field from a central massive star is taken to be 4×10^5 G_o at r = 20 AU (where G_0 represents the mean interstellar radiation field intensity), ranging down to 10^4 G_o at r_g (where r_g is given by equation 6.2)

$$r_g = GM_* \frac{\mu m_H}{kT} \tag{6.2}$$

The interstellar radiation field is taken to be ambient and is therefore negligible.

This strong UV field will determine the temperature of the gas at each point in the envelope. The gas in the upper layer of the PDR is assumed to be heated to a temperature of 1000 K (e.g. Carr *et al.*, 1995), while subsequent lower layers, due to shielding and cooling effects, are assumed to be at a temperature corresponding to the midplane disk temperature at that given radii. The temperature of the midplane of the disk is calculated using equation 6.3 (Aikawa *et al.*, 1997),

$$T(r) = 28 \left(\frac{r}{100 \text{ AU}}\right)^{-1/2} \left(\frac{L_*}{L_\odot}\right)^{1/4} \text{ K} \tag{6.3}$$

where L_* (GL 2591) = 9×10^4 $L_\odot$ (Lada *et al.*, 1984), and the scale height, *H(r)* is calculated from equation 6.4 (Hollenbach *et al.*, 1994)

$$H(r) = r_g \left(\frac{r}{r_g}\right)^{3/2} \tag{6.4}$$

The values for the physical and chemical parameter set employed for the grid models is summarized in Table 6.2 and the dependence of number density on z is assumed to be given by equation 6.5,

$$n(r,z) = n(r,z=0) exp\left(\frac{-z^2}{H(r)^2}\right) \tag{6.5}$$

Table 6.1: Parameters for each radial point studied for a $10M_{\odot}$ star.

Radius (AU)	$n(r, z = 0)$ (cm^{-3})	$T(r)$ at midplane (K)	$H(r)$ (AU)
40	2.59(10)	767	6.86
60	8.51(09)	626	12.60
80	3.86(09)	542	19.40
100	2.09(09)	485	27.12
200	3.10(08)	343	76.70
300	1.02(08)	280	140.90
400	4.61(07)	242	216.93
600	1.51(07)	198	398.53
800	6.85(06)	171	613.57
1000	3.71(06)	153	857.49
1200	2.24(06)	140	1127.20
1360	1.59(06)	132	1360.00

The notation a(b) implies a $\times$ 10^{b}.

where $n(r, z = 0)$ and $\rho(r, z = 0)$ are given by equations 6.6 and 6.7 respectively.

$$n(r, z = 0) = \frac{\rho(r, z = 0)}{\mu \ m_{\rm H}} \tag{6.6}$$

$$\rho(r, z = 0) = 1.4 \ \times \ 10^{-9} \ r^{-2.75} \tag{6.7}$$

YSOs are considered to be strong sources of x–rays which may significantly affect the chemistry of the disk. Igea and Glassgold (1999) predict that stellar x–rays can penetrate the entire disk. In some models therefore, we simulate the presence of x–ray ionization (as in Chapter 5) by enhancing the ionization rate, ζ, above the standard cosmic–ray rate of 1ζ up to $10^{5}\zeta$ (standard cosmic–ray rate = $1\zeta = 1.3 \times 10^{-17}$ s^{-1}).

Our model is a two–phase calculation. In the first Phase, we consider a single–point collapse for a cloud forming a star–disk system. This calculation is required

in order to derive the initial atomic and molecular abundances in the disk. The collapsing model takes into account freeze–out and surface hydrogenation (as in Viti and Williams, 1999*a*). The initial elemental fractional abundances are those appropriate for a dark cloud (as given in Table 1.2). The chemistry includes 337 species in a network of 2950 chemical reactions taken from the UMIST database (Millar *et al.*, 1997). The initial and final number densities adopted in this phase are 10^4 and 10^7 cm^{-3} and the collapse is assumed to be free–fall.

We also made an alternative calculation of initial molecular abundances for the second phase. In the first phase of our calculations, instead of assuming that at late times the gas–phase species accreted onto grain surfaces, which subsequently underwent hydrogenation reactions, we suppressed freeze–out so that all species remained in the gas–phase. This purely gas–phase description was then used as the initial composition of the disk at the start of Phase 2.

The UV radiation field from the central object (or from an external OB source) is assumed to be switched on at the start of Phase 2, and irradiates the two–dimensional disk. When the UV field is switched on, the icy mantles are assumed to be instantaneously evaporated. The chemical evolution of the envelope of the disk is followed at 12 different radii (as specified in Table 6.1) and at each radius the envelope, treated as a PDR, is represented by a slab subdivided into 5 shells represented by 5 depth points of increasing visual extinction, density and decreasing temperature from the edge of the disk (where the temperature is 1000 K) towards the midplane.

For each radius, we have computed a grid of models (see Table 6.2) in which we vary the ionization rate and temperature within the envelope. This is done in order to investigate the effect of the x–ray ionization on the disk. The column densities for each species in the PDR was then calculated for each model.

Table 6.2: Parameter set for grid of models.

Model	Scenario	Temperature of Lower Layers (K)	Mass of Central Star
A	PDRE with 1ζ	midplane value	$10M_\odot$
B	PDRE with $1(03)\zeta$	midplane value	$10M_\odot$
C	PDRE with $1(05)\zeta$	midplane value	$10M_\odot$
D	PDRE with 1ζ	1000 K	$10M_\odot$
E	PDRE with $1(03)\zeta$	1000 K	$10M_\odot$
F	PDRE with $1(05)\zeta$	1000 K	$10M_\odot$
G	No PDRE present and 1ζ	midplane value	$10M_\odot$
H	PDRE with 1ζ	midplane value	$1M_\odot$
I	PDRE with 1ζ	100 K	$1M_\odot$
J	No PDRE present and 1ζ	midplane value	$1M_\odot$

The notation a(b) implies a $\times$ 10^b and abbreviation PDRE - Photon Dominated Region Envelope

6.4 Results and Discussion

The results for Models A–G are given in Table 6.3. The table contains the averaged weighted column densities over the entire area of the PDR above the disk for $r < r_g$. Table 6.3 also compares the model results with all known molecular observations of GL 2591, the best candidate for the high stellar mass scenario being studied here. As stated in § 6.1, GL 2591 has been observed by Carr *et al.* (1995) to have hot gas at the surface of the disk. Five separate observations have been made to date by Mitchell *et al.* (1989); Carr *et al.* (1995); Helmich *et al.* (1996); Lahuis and van Dishoeck (2000) and Boonman *et al.* (2000).

We found the models using purely gaseous initial abundances produced column densities in the PDR of the disk lower than observed. This mainly affected species

such as NH_3, CH_4, HCN and H_2O which are further produced in the collapse phase via hydrogenation reactions of the grain surfaces. Therefore, we chose to use the models in which freeze–out occurs in Phase 1, followed by evaporation in the second phase. This scenario has also been predicted by Carr *et al.* (1995) who show that their observations can be explained by models in which gas–phase species are preserved on grain mantles and later released at high temperatures.

We discuss first the sensitivity of the model to the parameter changes representing the ionization rate and the assumed temperature of the inner layers of the PDR. Models A, B and C represent the effect of changing the ionization rate by factors of 1, 10^3, and 10^5 respectively for a given temperature structure. It has previously been shown (Lepp and Dalgarno, 1996) that the presence of x–rays causes an enhancement in certain species, including NO, CN, HCN and CH, although this enhancement in abundance is not seen in all species (for a more detailed discussion see Chapter 5). Molecules such as CO and N_2 are more readily dissociated due to the enhanced ionization rate, and this dissociation produces free atoms, which are then used in the formation of simple molecules such as HCN and NH_3. For models A, B and C, changes in our computed column densities arising from changes in the ionization rate are always by less than a factor of five, and often less than a factor of two. Evidently, as the ionization rate changes, at the high number densities of the gas considered here the formation and destruction processes are more or less equally affected. This conclusion is also evident in the results from models D, E and F, which also show the effect of changing the ionization rate in a PDR with a different temperature structure.

The effects of temperature are more pronounced. We may compare the pairs A and D, B and E, and C and F, each pair having the same ionization rate, but a different temperature structure. In models D, E and F (which are probably less realistic than models A, B and C), the higher temperature layers are assumed to

penetrate deeper than in models A, B and C. Apart from the case of CO, the models with higher temperatures at greater depths show greater column densities, in several cases - notably NH_3 - by more than one order of magnitude. This result simply reflects the effect of temperature increases on mildly endothermic reactions included in the chemical network. The increased abundances of HCN, CH_4 and NH_3 can be explained by considering their main formation routes: H_2 + CN, H_2 + CH_3 and H_2 + NH_2 for the formation of HCN, CH_4 and NH_3 respectively. These reactions have energy barriers, therefore making them more significant in the high temperature regimes studied here. C_2H_2 also shows a sharp increase in abundance which is also due to the increased temperatures. At high temperatures, oxygen atoms become locked into H_2O and it is this increase in water abundance which produces the increase in C_2H_2 column densities via the reaction $C_2H_3^+$ + H_2O. No significant increase in abundance is seen for either CS or SiO. This is because neither their main formation or destruction mechanisms have energy barriers and therefore remain unaffected by the increase in temperature.

The chemical effect of including the PDR may be estimated by comparing results of Model G with those of Models A–F. Model G conditions consisted of only a cold, dense disk, without the corresponding PDR envelope above the surface of the inner disk. For consistency, in this case (G) we have assumed only an ambient interstellar radiation field, and therefore the temperatures of the entire disk remain relatively low. The results are given in Table 6.3. The PDR clearly contributes very significantly to the predicted column densities of all the species listed, most notably so in the case of C_2H_2 which is increased in the case of models A–C by about two orders of magnitude and for models D–F by over three orders.

It is of interest to compare the model results with the column densities inferred from observations. It should, however be noted that the models have not been designed to "fit" any particular object, rather to illustrate the contribution of a

PDR and to explore its sensitivity to ionization rate and temperature structure. We do not, therefore, expect to find a perfect match. Nevertheless, the results shown in Table 6.3 are very encouraging for the small list of molecules for which detections or upper limits are available. In general, model A provides reasonable agreement, apart from the case of C_2H_2. As we have seen, the temperature sensitivity of this species is much greater than that of other species, so a modest increase in a PDR temperature distribution in the envelope should provide enough C_2H_2 to give a reasonable match. This is in contrast to the results of Millar *et al.* (1991) and Charnley and Tielens (1992) who argued that a hot gas–phase chemistry was unable to produce observed quantities of C_2H_2. It has since been proposed that if sufficient abundances of C_2H_2 are to be produced, the molecule must be present in ice mantles on grain surfaces, and an abundance of 0.1-0.5 % of water ice is needed (Lahuis and van Dishoeck, 2000). The subsequent sublimation of the ice is predicted to produce the high abundances observed. Although there are no grain surface reactions in the rate file used in this work, a number of reactions to generate C_2H_2 are known, including reactions 6.8-6.11 which have been taken from the Ohio ratefile (Ruffle and Herbst, 2000).

$$GH_2 + GC_2H \longrightarrow GC_2H_2 \tag{6.8}$$

$$GCH_2CO \longrightarrow GC_2H_2 + GO \tag{6.9}$$

$$GC_2H_4 \longrightarrow GC_2H_2 + GH_2 \tag{6.10}$$

$$GH_2C_3N \longrightarrow GC_2H_2 + GCN \tag{6.11}$$

where GX_i represents species X_i on a grain surface. The surface formation of C_2H_2 may be especially efficient for reactions 6.8 and 6.9 due to the fact that the grain surface fractional abundances of C_2H and CH_2CO are sufficiently high ($\sim 10^{-7}$ and 10^{-8} respectively).

Table 6.3: Comparison of observed column densities of species towards GL 2591 with weighted averaged column densities over the entire disk, for models A–G for the same selection of species. Observations taken from: *i* - Mitchell *et al.* (1989); *j* - Carr *et al.* (1995); *k* - Lahuis and van Dishoeck (2000); *m* - Boonman *et al.* (2000); *n* - Helmich *et al.* (1996).

	Column Densities (cm^{-2}) for Models							
Species	Observed (10^{16})	A	B	C	D	E	F	G
CO^i	560 ± 110	4.14(18)	4.10(18)	3.03(18)	6.54(17)	4.80(17)	4.77(17)	2.21(17)
HCN^j	1.6 ± 0.5							
HCN^k	4.0 ± 0.6	6.64(16)	7.13(16)	7.18(16)	2.18(17)	2.81(17)	4.79(17)	1.86(16)
HCN^m	6.6							
$C_2H_2{}^j$	1.05 ± 0.16	2.74(14)	3.44(14)	2.91(14)	1.17(16)	0.51(16)	0.48(16)	4.29(12)
CH_4^j	< 130	1.44(17)	2.88(16)	8.51(16)	2.57(18)	1.43(18)	1.25(18)	6.40(16)
NH_3^j	< 0.7	3.91(16)	1.66(16)	1.66(16)	1.59(17)	3.97(17)	1.18(17)	6.93(14)
CS^j	< 0.9	1.1(14)	2.78(14)	2.16(14)	2.67(14)	7.40(14)	7.84(14)	2.36(13)
SiO^j	< 2.5	4.56(14)	4.30(14)	1.73(14)	3.16(14)	7.25(12)	2.36(12)	2.43(13)
H_2O^n	200	2.22(18)	1.90(18)	1.55(18)	8.50(18)	8.67(18)	8.62(18)	3.20(17)

Notation a(b) $\equiv$ a $\times$ 10^b.

6.5 Other Potentially Detectable Molecules in Disks Around Massive Stars

So far, only four molecules (see Table 6.3) have been detected in disks around isolated massive stars, while upper limits have been estimated for a further four species. In this section we investigate the chemistry of some other species previously observed in other regions, also predicted by our models to be abundant in disks around massive stars. Table 6.4 lists these species for models A, B and C. We list only those species that are sufficiently abundant to be detectable and which have been observed elsewhere in the interstellar medium and/or in comets.

Comparing the predicted abundances shown in Table 6.4 with those found in dark clouds (e.g. in the particularly molecular rich object, TMC–1), we find that, in general, many species, including H_2CS, NH_3, CH_2CN, and HC_3CN, should be enhanced in disks around massive stars. We also notice that some species vary in fractional abundance with the ionization rate; examples are CH, C_2H, and HCO^+. By investigating and understanding the above behaviours, we can divide species into 'classes' which may allow us to use different molecules as tracers of different properties of the disks. Enhanced abundances with respect to dark clouds for some of the species, such as NH_3 and H_2CS, may be easily explained: our initial abundances (as derived from Phase 1 of our calculations) are the result of the collapse of a cloud with subsequent freeze–out and hydrogenation on to grains. Once the UV radiation field is 'switched on' (Phase 2), the mantle evaporates, injecting in the gas a high abundance of hydrogenated species such as NH_3 and H_2CS. By detecting these species it may be possible to determine the degree of depletion and hydrogenation in disk environments.

The abundance of HCO^+ increases by about two orders of magnitude when the ionization rate is increased by a factor of 10^5. The main route of formation of HCO^+

Table 6.4: Predicted column densities of a selection of observable species for high stellar mass case.

	Column Densities (cm^{-2})			
Species	Model A	Model B	Model C	TMC–1†
OH	5.92(16)	6.19(16)	9.89(16)	3.00(15)
CH	1.27(12)	2.04(13)	1.57(15)	2.00(14)
CH_3	1.06(14)	2.82(14)	4.85(15)	—
C_2	4.04(14)	3.25(15)	7.01(15)	—
C_2H	1.19(12)	2.39(14)	9.04(14)	5-10(14)
HCO	1.37(12)	5.57(12)	2.10(12)	—
HCO^+	2.79(13)	2.70(14)	3.34(15)	8.00(13)
H_2CO	2.65(14)	1.35(14)	1.54(14)	2.00(14)
H_2S	7.72(13)	1.64(13)	5.99(12)	< 5.00(12)
OCS	1.96(14)	3.47(13)	—	2.00(13)
CS	1.10(14)	2.78(14)	2.16(14)	1.00(14)
HCS	3.80(13)	5.83(13)	4.60(13)	—
H_2CS	1.68(14)	2.54(13)	2.03(13)	3.00(13)
SO	3.61(14)	4.48(14)	6.22(13)	5.00(13)
SO_2	6.83(14)	2.17(14)	1.82(13)	< 1.00(13)
NH	1.97(13)	3.35(13)	1.23(14)	—
NH_2	1.06(13)	4.22(13)	2.27(14)	—
NH_3	6.49(15)	3.91(16)	1.66(16)	2.00(14)
CN	1.24(12)	3.25(13)	7.47(14)	3.00(14)
H_2CN	1.53(12)	—	1.05(12)	—
CH_2CN	2.30(16)	1.81(16)	2.12(16)	5.00(13)
HC_3N	5.66(15)	1.29(16)	3.03(15)	6.00(13)
C_2H_3	1.21(12)	—	1.52(12)	—
C_2H_4	1.57(14)	1.15(13)	5.14(13)	—
C_3	1.13(14)	2.09(14)	1.22(15)	—
HNC	3.12(16)	2.67(16)	2.16(16)	2.00(14)
HC_5N	2.01(15)	5.63(14)	2.97(14)	3.00(13)
C_3H_4	3.69(12)	2.91(12)	5.52(12)	—
CH_3CN	2.23(14)	1.34(14)	1.45(14)	1.00(13)
CH_3OH	1.08(13)	2.95(12)	2.79(12)	2.00(13)
CH_3CO	5.73(12)	1.32(12)	—	—

Notation a(b) $\equiv$ a $\times$ 10^b. † - TMC–1 column densities were taken from Ohioshi *et al.* (1992). A dash (—) indicates that the column density < 10^{12} cm^{-2}.

is:

$$H_3^+ + CO \rightarrow HCO^+ + H_2 \tag{6.12}$$

Moreover, its abundance is in any case enhanced with respect to the observed abundances in dark or dense clouds (Liszt and Lucas, 2000; Scappini *et al.*, 2000). This situation resembles the one found in Herbig–Haro (HH) objects (e.g. Girart *et al.*, 1994) where an enhancement of HCO^+ is indirectly due to the high UV radiation field generated in the shock (Viti and Williams, 1999*b*). This enhancement arises from the rapid creation of C^+ by photo–processing of CO and the reaction of C^+ with abundant H_2O released from grains. A similar process may be occurring in circumstellar disks. The UV radiation field is much higher than the one assumed to be present in the HH clumps; this is consistent with the larger abundance of HCO^+. In fact, HCO^+ is potentially a 'multiple' tracer. Firstly, it may trace high radiation field environments where depletion, hydrogenation and subsequent evaporation have occurred. Secondly, it can be used to determine the level of x–ray ionization coming from the central star; and, thirdly, it can be a tracer of the disk evolution: the column densities in Table 5 are derived at steady–state, which is reached $\sim 10^4$ years after the disk envelope is formed. However, HCO^+ abundance is much higher at earlier stages of the disk evolution, due to the higher abundance of H_3^+. An accurate determination of HCO^+ abundance could, therefore provide useful clues to the disk evolutionary stage.

6.6 Disks Around Low Mass Stars

So far, we have only considered an isolated system of a disk around a massive star. A PDR envelope above a disk around a low mass star may also form by the illumination from a nearby OB association. In this scenario we have assumed a geometry with a OB association illuminating the disk surface with a uniform

Table 6.5: Predicted column densities of a selection of observable species in the PDR around a solar mass stellar system.

	Column Densities (cm^{-2})		
Species	Model H	Model I	Model J
CO	1.54(20)	1.73(20)	1.39(19)
HCN	5.67(16)	5.45(16)	2.03(15)
C_2H_2	3.59(14)	2.21(15)	4.46(11)
CH_4	1.32(18)	1.34(18)	4.07(14)
NH_3	1.49(16)	2.10(16)	8.20(13)
CS	1.67(13)	7.47(14)	4.05(14)
SiO	2.94(16)	2.86(16)	2.05(15)
H_2O	3.36(19)	3.34(19)	1.17(16)

Notation a(b) $\equiv$ a $\times$ 10^b.

enhanced UV field of 10^4 G_0. The physical properties of a disk around a low mass star are very different, and the critical gravitational radius, r_g, for an assumed $1M_\odot$ star will be significantly smaller than that previously considered for a disk around a $10M_\odot$ object. The predicted column densities for Models H–J are given in Table 6.5 for those species previously listed in Table 6.3, for which detections or observational upper limits exist.

Models H and I include a PDR, while model J excludes it. In model I, the region inside the PDR is warmer than in model H. None of these models includes an enhanced ionization rate. The general conclusions for Table 6.3 also apply here. It is remarkable that the averaged molecular column densities predicted for these species in this system are generally comparable to those in the disk around a massive star. The implication of Table 6.5 is, therefore, that the detections made for GL 2591, might be repeated for disks around low mass stars illuminated by an OB association,

for example in Orion.

We complete this discussion by showing in Table 6.6 a list of species predicted to be abundant, and potentially detectable in disks around low mass stars illuminated by a nearby OB association (Models H and I). In general, as indicated in Table 6.4, the averaged weighted column densities predicted for models H and I are comparable to those for models A, B and C. However, there are several exceptions; for example HCO^+ is much less abundant, while CH_3, CH_2CN, SO_2 and HCS are much more abundant in the low mass case. The carbon chain HC_5N and the radical H_2CN are probably undetectable in the low mass case. Nevertheless, it is clear that there is a wide range of molecules with potentially detectable abundances in disks around low mass stars, assuming that the disks fill a reasonable fraction of the telescope beam.

At present there are no known observational data for gas of a suitably high temperature to make an accurate comparison with our model results. It should be noted that there is a significant difference in the results between the $1M_\odot$ and $10M_\odot$ case for molecules CO and CS. This is due to the very different lower layer temperatures in the PDR envelope between the high mass and low mass regions. The cooler temperatures of the $1M_\odot$ disk greatly enhances the formation of CO and vice versa for CS.

As with the high mass case, a stellar–disk region without an enhanced UV produces vastly differing model results. This can be seen when comparing the Model J results with the other two models (see Table 6.5).

6.7 Conclusions

Disks around massive young stellar objects, and disks around low mass stars irradiated by nearby OB associations, are eroded by photo–evaporation. In the latter case, this erosion may be an important factor in planet formation. As Johnstone *et al.* (1998) have shown, photo–evaporating material is gravitationally retained within

Table 6.6: Predicted column densities of a selection of observable species, for the low mass case.

	Column Densities (cm^{-2})	
Species	Model H	Model I
OH	4.14(16)	4.14(16)
CH	5.26(13)	5.29(13)
CH_3	7.52(16)	7.52(16)
C_2	5.18(15)	5.18(15)
C_2H	1.82(15)	1.82(15)
HCO	3.61(12)	1.70(13)
HCO^+	—	1.04(12)
H_2CO	6.53(14)	5.13(14)
H_2S	1.12(13)	1.11(13)
OCS	6.24(12)	—
CS	7.47(14)	1.69(13)
HCS	1.13(16)	1.13(16)
H_2CS	9.63(12)	7.68(12)
SO	7.43(13)	5.52(14)
SO_2	8.67(16)	8.89(16)
NH	4.81(12)	4.87(12)
NH_2	7.74(12)	7.84(12)
NH_3	2.10(16)	1.49(16)
CN	1.01(13)	1.01(13)
CH_2CN	4.56(18)	4.56(18)
HC_3N	1.48(13)	2.10(12)
C_2H_3	7.68(12)	7.68(12)
C_2H_4	7.29(13)	7.24(13)
C_3	7.15(12)	7.15(12)
HNC	2.02(16)	2.11(16)
C_3H_4	3.13(12)	2.26(12)
CH_3CN	3.37(13)	3.00(13)
CH_3OH	1.70(13)	5.36(12)
CH_3CO	2.71(13)	2.90(12)

Notation a(b) $\equiv$ a $\times$ 10^b. A dash (—) indicates that the column density $< 10^{12}$ cm^{-2}.

a critical radius from the star, and constitutes an envelope similar to a Photon–Dominated Region (PDR) that normally arises at the edge of a molecular cloud irradiated by a massive star. We have explored the chemistry in a disk/PDR system and have compared it to a similar system without a PDR.

This was accomplished by calculating a two phase model; firstly, a collapse from low density to a high density appropriate for a disk; and, secondly, a two–dimensional calculation of the irradiation of disk material by the radiation field of the central massive star or nearby OB association. The model follows the chemistry self–consistently through both phases.

For the case of a massive central star, we predict that the disk/PDR system generates many abundant molecular tracers. These are generally insensitive to the adopted ionization rate, but do depend on the temperature structure that is adopted within the disk/PDR. Results of models are compared with the rather limited observational data for one disk around a massive star, GL 2591. Although the models are not intended as a "fit" to the data, the agreement is reasonably satisfactory. The contribution of the PDR to the chemistry is clearly significant, and we predict several as yet unobserved molecules to be detectable in disks with a central massive star.

Disks around low mass stars are much more common, and our models show that if irradiated by nearby OB associations, molecular tracers would also be generated in the disk/PDR system that are distinct from the system without a PDR. There have been no reported detections, to date, of any of the species predicted; however their averaged column densities are generally similar to those predicted (and, in four cases, observed) for a disk around a massive star. Detection of these species in a disk around a low mass star would identify that disk erosion was occurring and therefore that the disk has a limited life. This conclusion would have consequences for planet formation in the disk.

CHAPTER 7

Conclusions and Future Work

"One never notices what has been done; one can only see what remains to be done..."

– Marie Curie

During the course of this thesis, we have shown that interface layers are hosts to a rich variety of molecular species, which may be used to trace a diverse selection of regions in the interstellar medium. In Chapter 2 we modelled the transition interface in which water ice is deposited onto dust grains, using a gas–grain chemical model. We also included the effects of the photo–desorption of OH from grain surfaces, once it is formed from the photodissociation of water. We demonstrated that at high extinctions, our results showed the observed near–linear relationship between ice column density and A_V, whereas for lower extinction values, we have shown that relatively large abundances of water ice can be formed at $A_V \leq 3$ if photo–desorption of water via photodissociation is inefficient. However, if photo–desorption is found to be efficient, water ice can be retained on grain surfaces if it is initially formed on grain surfaces other than olivine (e.g. amorphous carbon), where the adsorbates bind more strongly, and hence the evaporation would be less efficient. It is clear that further work into the full understanding of the measured low–extinction ice vs A_V relation

in Taurus and other sources will require an improvement in our understanding of surface chemistry, especially on amorphous ice, and of photo–desorption on a variety of surfaces.

In Chapter 3 we considered the effects of mixing hot ionized gas into the edge of a cold neutral molecular cloud. We used a simple process to predict important tracers in the mixing zone. We predict that if the temperature remains low after mixing, species such as C, C^+ and CH are enhanced in the mixing layer. Alternatively, if there is an increase in temperature after mixing has occurred, a different set of species are predicted to be enhanced in the interface layer. The molecular tracers in a heated layer include OH, H_2O, HCO^+ and NH_3. This enhancement is caused by the higher temperatures driving the H^+/O charge exchange reaction, which feeds the oxygen chemistry. It is presumed that mixing is most likely accompanied by heating and therefore the models with an enhanced temperature are predicted to be the most typical for this type of mixing layer chemistry.

In Chapter 4 we examined the interface layer around a diffuse cloud, which is embedded in a flowing intercloud medium. Our results have shown that observable abundances of various polyatomic species can be produced if the warm interface regions occupy a few percent of the total molecular column density along that line–of–sight. We made a comparison of our results with the observational data of Liszt and Lucas and found that some models give results that are in harmony with measured ratios of several species including C_2H, HCO^+ and OH, although these models specified a radiation field intensity of about one tenth of the mean interstellar radiation field intensity. Such conditions may be more likely to occur in interfaces around diffuse clumps within Giant Molecular Clouds than those around the isolated "field" diffuse clouds. However, in some cases the results suggest that the gas–phase chemical network used may be too limited. Surface reactions may also contribute to molecular abundances in both warm interfaces and in the cold cloud

gas. Therefore, future work into this area will require further development in the understanding of gas–phase chemical reactions and their corresponding rates. This could allow a more thorough study of such interface layers to be made. The inclusion of a comprehensive gas–grain chemical network should also be included in future studies.

In Chapter 5 we studied the effect that a nearby or embedded x–ray source could have on the abundances within the cloud. In a simple case where we simulated x–ray ionization and the corresponding temperature increase in a cloud of gas, we found that the abundance of molecules such as CH, CN, OH, NO were significantly enhanced, although this effect was very sensitive to the increased temperature assumed. When considering time–dependent effects, we found a significant early time peak in the abundances for a small selection of species including CH, CH^+ and C_2H. This early time peak could provide a vital tool to determine the chronological evolution for the region. We also added the formation and destruction of C^{++} into the reaction network and found that at very high ionization values, the abundance of CH^+ could be significantly enhanced. Further work in this area is required because the chemical network for doubly ionized atoms is far from complete. We need to include a more complex reaction network for C^{++}, incorporating more accurate reaction rates, as well as considering the inclusion of other doubly ionized species. A more detailed study of the temperature effects could also produce a more accurate model of x–ray ionization and gauge for the age of the cloud.

Finally, in Chapter 6 we have explored the chemistry in a disk/PDR system around a young star and have compared it to a similar system without a PDR. For the case of a disk orbiting a massive central star, we predict that the disk/PDR system generates many abundant molecular tracers. These are generally insensitive to the adopted ionization rate, but do depend on the temperature structure that is adopted within the disk/PDR. It is found that the contribution of the PDR to

the chemistry is significant, and we predict several as yet unobserved molecules to be detectable in disks with a central massive star. Disks around low mass stars are much more common, and our models have shown that if such a disk is irradiated by nearby OB associations, molecular tracers would also be generated in the disk/PDR system that are distinct from the system without a PDR. Detection of these species in a disk around a low mass star would confirm that disk erosion was occurring and therefore that the disk has a limited life. A further study into such a disk/PDR system could include the effects of mixing of the hot PDR region into the cold central layer of the disk to see how the column densities are affected. For the low mass stellar case, variations in the orientation of the OB association could produce an asymmetry in the PDR around the disk, which could produce interesting effects on the column densities of the tracers. We should also include a more complex set of grain surface reactions into the Phase 1 calculations, to more accurately predict the initial abundances for Phase 2.

7.1 Future Work

In recent years there has been a growing body of evidence suggesting that the interstellar medium contains significant structures over scales as small as a few AU. Small scale structure has been observed via two different techniques; (i) the detection of variations in absorption occurring over extended objects and (ii) temporal variability in interstellar absorption lines.

VLBI observations of the 21–cm line towards extended extragalactic sources have been made by a number of authors (e.g. Dieter *et al.*, 1976; Diamond *et al.*, 1989; Davis *et al.*, 1996). They found large variations in the neutral hydrogen column densities over the sources. Furthermore, optical observations of binary star systems have shown significant differences in the absorption occurring in these closely spaced sight–lines (e.g. Watson and Meyer, 1996; Meyer and Blades, 1996; Price *et al.*, 2001).

Frail *et al.* (1994) observed temporal variations in the neutral hydrogen absorption towards high proper motion pulsars. Temporal variations in optical absorption lines (largely from neutral Na) have also been detected by a number of authors including Hobbs *et al.* (1982); Blades *et al.* (997); Price *et al.* (2000).

Assuming the absorption occurs within roughly spherical clouds, the implied spatial densities required to produce the variations in the the observed column densities are very large (up to 10^6 cm^{-3}). In the case of the Na absorption, and using the empirical relationship between the Na and hydrogen column densities derived by Ferlet and Gry (1985), the calculated cloud density is approximately 10^4 cm^{-3}. However, such high spatial densities are inconsistent with the observed Ca depletion (Price *et al.*, 2000).

One of the favoured explanations invoked to explain the presence of small scale structures is based on non–spherical cloud geometry (Heiles, 1997). Heiles states that clouds within the cold neutral medium are composed of cold dense sheets/filaments of gas, separated by warmer, less dense material. When these sheets and filaments are aligned along the line–of–sight, they allow for large changes in column densities over small transverse scales without requiring such high spatial densities. The densities of these filaments can be assumed to be $\geq 10^3$ cm^{-3}.

We have recently embarked on a study of these filamentary structures to determine if molecules could exist in such regions. Using the standard single–point chemical models assumed throughout this thesis, we calculated a grid of models assuming a filament with a temperature of 100 K and a variety of densities (from 10 cm^{-3} to 10^4 cm^{-3}), and A_V (from 0.01 to 1.0). We predict that a number of molecules would have observable column densities. Results of the column densities for a selection of models and species are given in Table 7.1.

Using the predicted column densities, an observing proposal was written by Dr. Ian A. Crawford, which has recently been accepted. The proposed observations

will allow a study of the line–of–sight towards κ Vel to be made. We intend to re-observe Na I, Ca II and K I, as well as making new observations of Ca I and CH. The detections, if made, will provide useful information in constraining the densities and temperatures of the filament structures.

Table 7.1: Predicted column densities for a selection of species.

Predicted Column Densities (cm^{-2})									
	n_H (cm^{-3})								
	100			500			1000		
	A_V								
Species	0.01	0.60	1.00	0.01	0.60	1.00	0.01	0.60	0.01
CO	4.97(10)	9.16(13)	1.19(16)	4.97(10)	9.16(13)	1.19(16)	6.29(10)	3.34(14)	5.99(16)
OH	1.27(11)	2.31(12)	4.42(12)	1.27(11)	2.31(12)	4.42(12)	6.21(10)	1.65(12)	2.62(12)
CH	—	1.92(13)	4.19(13)	—	1.92(13)	4.19(13)	3.06(10)	2.98(13)	4.50(13)
CN	—	2.25(10)	1.80(11)	—	2.25(10)	1.80(11)	—	7.24(10)	3.33(11)

Notation a(b) $\equiv$ a $\times$ 10^b; A dash (—) indicates that the column densities $<$ 10(10) cm^{-2}.

List of Publications

The following papers are based on work described in this thesis.

Nguyen, Hartquist and Williams (2000)

Nguyen, Hartquist and Williams (2001)

Nguyen, Ruffle, Herbst and Williams (2002)

Nguyen, Viti and Williams (submitted)

Nguyen, Crawford, Viti and Williams (in preparation)

ACKNOWLEDGEMENTS

"They say hard work never hurt anybody, but I figure why take the chance."

– Ronald Reagan

Foremost, I would like to say thank you to my supervisor, David Williams, for initially finding me the funding to do the PhD, but also for being an excellent supervisor. For never telling me what I say is stupid, for keeping me along the straight and narrow and for telling me to stop working and start writing up! The meals and parties have also made it all fun.

There are also a number of collaborators whom I would have been lost without. I would like to thank Serena Viti for helping me with the codes and for her work on Chapter 6. Tom Hartquist has also been great to work with, providing me with many useful comments and advice on Chapters 3 and 4. Eric Herbst and Debbie Ruffle invited me to spend an amusing month in Ohio (all those shopping trips and the insight into Mid-west America was also an experience). They have both taught me an incredible amount about grain surface chemistry, which has given me significant help with Chapter 2. I would also like to thank Ian Crawford for writing the observing proposal for the filamentary work. Hope the weather is clear.

There are also a number of people in the department, including Chris Evans, Phil O'neill, Stuart Colley and Richard Townsend, who I would like to give my thanks.

They have all obligingly answered my numerous (and often stupid) programming and latex questions. John Deacon has also been incredibly helpful in getting my stubborn laptop (which was kindly acquired for me by Jason Wake) to work properly, as well as retrieving vast quantities of data of backup tapes, which I felt the need to delete.

On a more personal note, I would like to thank Richard for so many things that I couldn't possibly list them all here. However, I should say that without Richard I would probably still be writing up now. He is great at making me get out of bed in the morning, even though he knows he will get hit. He always makes me work harder than I want to, and keeps me sane while I am doing it. Although, most importantly, he is great at making me endless cups of tea!

I really should not forget about my family, I would like to thank them for the moral support that they have given me throughout the course of my studies and for the numerous trips to Sainsbury's and the theatre. I should also say that I am very grateful that my mom & Robert convinced me that doing an 'A' level in Home Economics was not the best of ideas!

Finally, I would like to thank all my friends who have all hindered my attempts to submit my thesis on time! The countless trips to new and wonderful tea shops, bars and restaurants have provided for a great three years.

Bibliography

Adamson, A. J., Whittet, D. C. B., Bode, M. F., Longmore, A. J., Roche, P. F., McFadzean, A. D., Geballe, T. R. and Aitken, D. K., 1988, *Dust in the Universe* (Cambridge University Press, Oxford)

Aikawa, Y. and Herbst, E., 1999, *A&A*, **351**, 233

Aikawa, Y., Umebayashi, T., Nakano, T. and Miyama, S., 1997, *ApJ*, **486**, L51

Aikawa, Y., Umebayashi, T., Nakano, T. and Miyama, S., 1998, in *Chemistry and Physics of Molecules and Grains in Space*, volume 109 of *Faraday Discussions*, p. 281

Bally, J., Sutherland, R. S., Devine, D. and Johnstone, D., 1998, *ApJ*, **116**, 293

Barnes, A., 1992, *JGR*, **97**, 12105

Blades, J. C., Sahu, M. S., He, L., Crawford, I. A., Barlow, M. J. and Diego, F., 997, *ApJ*, **478**, 648

Bohlin, R. C., Savage, B. D. and Drake, J. F., 1978, *ApJ*, **224**, 132

Boonman, A. M. S., van Dishoeck, E. F., Lahuis, F., Wright, C. M. and Doty, S. D., 2000, *ESASP*, **456**, 67

Bourdon, E. B., Prince, R. H. and Duley, W. W., 1982, *ApJ*, **260**, 909

Cameron, A. G. W., 1973, *Icarus*, **18**, 407

Carr, J. S., Evans, N. J., Lacy, J. H. and Zhou, S., 1995, *ApJ*, **450**, 667

Caselli, P., Hasegawa, T. I. and Herbst, E., 1998, *ApJ*, **495**, 309

Charnley, S. B., Hartquist, T. W., Dyson, J. E. and Williams, D. A., 1990, *MNRAS*, **243**, 405

Charnley, S. B. and Tielens, A. G. G. M., 1992, in *Astrochemistry of Cosmic Phenomena*, volume 150 of *IAU Symposium*, p. 317

Chiang, E. I. and Goldreich, P., 1997, *ApJ*, **490**, 368

Chiar, J. E., Adamson, A. J., Kerr, T. H. and Whittet, D. C. B., 1995, *ApJ*, **455**, 234

Clarke, C. J. and Pringle, J. E., 1993, *MNRAS*, **261**, 190

Coker, R., Rae, J. G. L. and Hartquist, T. W., 2000, *A&A*, **360**, 290

Crawford, I. A. and Williams, D. A., 1997, *MNRAS*, **291**, L53

Dalgarno, A., 1976*a*, *Atomic Physics and its Application*

Dalgarno, A., 1976*b*, *Frontiers of Astrophysics* (Harvard University Press)

Dalgarno, A. and Black, J. H., 1976, in *Report on Progress in Physics*, volume 39, p. 573

Davis, R. J., Diamond, P. J. and Goss, W. M., 1996, *MNRAS*, **283**, 1105

Diamond, P. J., Goss, W. M., Romney, J. D., Booth, R. S., Kalberla, P. M. W. and Mebold, U., 1989, *ApJ*, **347**, 302

Dieter, N. H., Welch, W. J. and Romney, J. D., 1976, *ApJ*, **206**, L113

Duley, W. W., Hartquist, T. W., Sternberg, A., Wagenblast, R. and Williams, D. A., 1992, *MNRAS*, **255**, 463

Duley, W. W. and Williams, D. A., 1984, *Interstellar Chemistry* (Academic Press, London, UK)

Dutrey, A., Guilloteau, S. and Guélin, M., 1997, *A&A*, **317**, L55

Elitzur, M. and Watson, W. D., 1978, *ApJ*, **222**, L141

Ferlet, R. Vidal-Madjar, A. and Gry, C., 1985, *ApJ*, **298**, 838

Flower, D. R. and Pineau des Forêts, G., 1998, *MNRAS*, **297**, 1182

Frail, D. A., Weisberg, J. M., Cordes, J. M. and Mathers, C., 1994, *ApJ*, **436**, 144

Gerakines, P. A., Whittet, D. C. B., Ehrenfreund, P., Boogert, A. C. A., Tielens, A. G. G. M., Schutte, W. A., Chiar, J. E., van Dishoeck, E. F., Prusti, T., Helmich, F. P. and de Graauw, T., 1999, *ApJ*, **522**, 357

Girart, J. M., Rodriguez, L. F., Anglada, G., Estalella, R., Torrelles, J. M., Marti, J., Pena, M., Ayala, S., Curiel, S. and Noriega-Crespo, A., 1994, *ApJ*, **435**, 145

Goldsmith, P. F., Langer, W. D. and Velusamy, T., 1999, *ApJ*, **519**, L173

Green, N. J. B., Toniazzo, T., Pilling, M. J., Ruffle, D. P., Bell, N. and Hartquist, T. W., 2001, *A&A*, **375**, 1111

Hall, S. M. and Clarke, C. J. ad Pringle, J. E., 1996, *MNRAS*, **278**, 303

Harris, D. H., Woolf, N. J. and Rieke, G. H., 1978, *ApJ*, **226**, 829

Hartmann, J., 1904, *ApJ*, **19**, 268

Hartquist, T. W. and Dyson, J. E., 1988, *Ap&SS*, **144**, 615

Hartquist, T. W., Dyson, J. E. and Williams, D. A., 1992, *MNRAS*, **257**, 419

Hasegawa, T. I. and Herbst, E., 1993*a*, *MNRAS*, **261**, 83

Hasegawa, T. I. and Herbst, E., 1993*b*, *MNRAS*, **263**, 589

Hasegawa, T. I., Herbst, E. and Leung, C. M., 1992, *ApJS*, **83**, 167

Heiles, C., 1997, *ApJ*, **481**, 193

Heller, C. H., 1995, *ApJ*, **455**, 252

Helmich, F. P., van Dishoeck, E. F., Black, J. H., de Graauw, T.and Beintema, D. A., Heras, A. M., Lahuis, F., Morris, P. W. and Valentijn, E. A., 1996, *A&A*, **315**, 173

Herbst, E. and Leung, C. M., 1989, *ApJS*, **69**, 271

Herbst, E. and Leung, C. M., 1990, *A&A*, **233**, 177

Hobbs, L. M., Wallerstein, G. and Hu, E. M., 1982, *ApJ*, **252**, 17

Hollenbach, D., Johnstone, D., Lizano, S. and Shu, F., 1994, *ApJ*, **428**, 654

Hollenbach, D., Yorke, H. W. and Johnstone, D., 2000, in V. Mannings, A. P. Boss and S. S. Russell (eds.), *Protostars and Planets*, 4, p. 401

Hollenbach, D. J. and Salpeter, E. E., 1971, *ApJ*, **163**, 155

Horedt, G. P., 1978, *A&A*, **64**, 173

Horedt, G. P., 1980, *A&A*, **92**, 267

Howe, D. A., Taylor, S. D. and Williams, D. A., 1996, *MNRAS*, **279**, 143

Igea, J. and Glassgold, A. E., 1999, *ApJ*, **518**, 848

Johnstone, D., 2000, in *Astrochemistry: From Molecular Clouds to Planetary systems*, volume 197 of *IAU Symposium*, p. 403

Johnstone, D., Hollenbach, D. and Bally, J., 1998, *ApJ*, **499**, 758

Jones, A. P. and Williams, D. A., 1984, *MNRAS*, **209**, 955

Katz, N., Furman, I., Biham, O., Pirronello, V. and Vidali, G., 1999, *ApJ*, **522**, 305

Konigl, A., 1995, *Rev. Mex. AC*, 1, 275

Krolik, J. H. and Kallman, T. R., 1983, *ApJ*, **267**, 610

Lada, C. J., Thronson, H. A., Smith Jr., H. A., Schwartz, P. R. and Glaccum, W., 1984, *ApJ*, **286**, 310

Lahuis, F. and van Dishoeck, E. F., 2000, *A&A*, **355**, 699

Lambert, D. L., Sheffer, Y. and Crane, P., 1990, *ApJ*, **359**, 19

Le Bourlot, J., Pineau des Forêts, G. and Roueff, E., 1995, *A&A*, **119**, 111

Le Bourlot, J., Pineau des Forêts, G., Roueff, E. and Schilke, P., 1993, *ApJ*, **416**, L87

Lee, H.-H., Bettens, R. P. A. and Herbst, E., 1996, *A&AS*, **119**, 111

Lee, H. H., Roueff, E., Pineau des Forêts, G., Shalabiea, O. M., Terzieva, R. and Herbst, E., 1998, *A&A*, **334**, 1047

Léger, A., Jura, M. and Omont, A., 1985, *A&A*, **144**, 147

Lepp, S. and Dalgarno, A., 1996, *A&A*, **306**, L21

Lepp, S. and Tiné, S., 1998, *The Molecular Astrophysics of Stars and Galaxies* (Oxford Science Publications, Oxford)

Liszt, H. S. and Lucas, R., 1995, *A&A*, **299**, 847

Liszt, H. S. and Lucas, R., 1998, *A&A*, **339**, 561

Liszt, H. S. and Lucas, R., 1999, *BAAS*, **194**, 4103

Liszt, H. S. and Lucas, R., 2000, *A&A*, **355**, 333

Liszt, H. S. and Lucas, R., 2001, *A&A*, **370**, 576

Long, R. S. and White, R. L., 1980, *ApJ*, **239**, 65

Lucas, R. and Liszt, H. S., 1993, *A&A*, **276**, L33

Lucas, R. and Liszt, H. S., 1996, *A&A*, **307**, 237

Lucas, R. and Liszt, H. S., 1997, in *Molecules in Astrophysics Probes and Processes*, volume 178 of *IAU Symposium*, p. 421

Lucas, R. and Liszt, H. S., 2000*a*, *A&A*, **355**, 327

Lucas, R. and Liszt, H. S., 2000*b*, *A&A*, **358**, 1069

Manicò, G., Raguní, G., Pirronello, V., Roser, J. E. and Vidali, G., 2001, *ApJ*, **548**, L253

Martin, C. E., Heyvaerts, J. and Priest, E. R., 1997, *A&A*, **326**, 1176

Meijer, A. J. H. M., Farebrother, A. J., Clary, D. C. and Fisher, A. J., 2001, *J. Phys. Chem. A*, **105**, 2173

Meyer, D. M., 1997, in *Molecules in Astrophysics Probes and Processes*, volume 178 of *IAU Symposium*, p. 407

Meyer, D. M. and Blades, J. C., 1996, *ApJ*, **464**, L179

Millar, T. J., Bennett, A., Rawlings, J. M. C., Brown, P. D. and Charnley, S. B., 1991, *A&AS*, **87**, 585

Millar, T. J., Farquhar, P. R. A. and Willacy, K., 1997, *A&AS*, **121**, 139

Millar, T. J. and Herbst, E., 1990, *A&A*, **231**, 466

Mitchell, G. F., Curry, C., Maillard, J.-P. and Allen, M., 1989, *ApJ*, **341**, 1020

Murakawa, K., Tamura, M. and Nagata, T., 2000, *ApJSS*, **128**, 603

Nejad, L. A. M. and Hartquist, T. W., 1994, *Ap&SS*, **220**, 253

Nguyen, T. K., Crawford, I. A., Viti, S. and Williams, D. A., in preparation, *MNRAS*

Nguyen, T. K., Hartquist, T. W. and Williams, D. A., 2000, *Ap & SS*, **271**, 171

Nguyen, T. K., Hartquist, T. W. and Williams, D. A., 2001, *A&A*, **366**, 662

Nguyen, T. K., Ruffle, D. P., Herbst, E. and Williams, D. A., 2002, *MNRAS*, **329**, 301

Nguyen, T. K., Viti, S. and Williams, D. A., submitted, *A&A*

O'Dell, C. R., 1998, *ApJ*, **115**, 263

Ohioshi, M., Irvine, W. and Kaifu, N., 1992, in *Astrochemistry of cosmic phenomena*, volume 150 of *IAU Symposium*, p. 171

Ohishi, M. and Kaifu, N., 1998, in *Chemistry and Physics of Molecules and Grains in Space*, volume 109 of *Faraday Discussions*, p. 205

Phillips, J. A. and Lazio, T. J. W., 1995, *ApJ*, **442**, 37

Pineau des Forêts, G., Roueff, E. and Flower, D. R., 1992, *MNRAS*, **258**, 45

Price, R. J., Crawford, I. A. and Barlow, M. J., 2000, *MNRAS*, **312**, L43

Price, R. J., Crawford, I. A. and Howarth, I. D., 2001, *MNRAS*, **321**, 553

Rawlings, J. M. C. and Hartquist, T. W., 1997, *ApJ*, **487**, 672

Rawlings, J. M. C., Hartquist, T. W., Menten, K. M. and Williams, D. A., 1992, *MNRAS*, **255**, 471

Ruffle, D. P., 1998, *The Physical and Chemical Evolution of Star Forming Regions* (Thesis)

Ruffle, D. P. and Herbst, E., 2000, *MNRAS*, **319**, 837

Ruffle, D. P. and Herbst, E., 2001*a*, *MNRAS*, **322**, 770

Ruffle, D. P. and Herbst, E., 2001*b*, *MNRAS*, **324**, 1054

Scappini, F., Cecchi-Pestellini, C., Codella, C. and Dalgarno, A., 2000, *MNRAS*, **317**, 6

Seward, F. D. and Chlebowski, T., 1982, *ApJ*, **256**, 530

Shakura, N. I. and Sunyaev, R. A., 1973, *A&A*, **24**, 337

Shalabiea, O. M., Caselli, P. and Herbst, E., 1998, *ApJ*, **502**, 652

Shu, F. H. Lizano, S., Ruden, S. P. and Najita, J., 1988, *ApJ*, **328**, L19

Smith, R. G., Sellgren, K. and Brooke, T. Y., 1993, *MNRAS*, **263**, 749

Stantcheva, T., Caselli, P. and Herbst, E., 2001, *A&A*, **375**, 673

Sternberg, A., Dalgarno, A. and Lepp, S., 1987, *ApJ*, **320**, 676

Storzer, H. and Hollenbach, D., 1999, *ApJ*, **515**, 669

Strom, S. E., 1995, *Rev. Mex. AA*, **1**, 317

Takahashi, J. and Williams, D. A., 2000, *MNRAS*, **314**, 272

Tanaka, M., Sato, S., Nagata, T. and Yamamoto, T., 1990, *ApJ*, **352**, 724

Taylor, S. D., Morata, O. and Williams, D. A., 1996, *A&A*, **313**, 269

Taylor, S. D. and Raga, A. C., 1995, *A&A*, **296**, 823

Teixeira, T. C. and Emerson, J. P., 1999, *A&A*, **351**, 292

van der Tak, F. F. S., van Dishoeck, E. F., Evans, N. J., Bakker, E. J. and Blake, G. A., 1999, *ApJ*, **522**, 991

van Dishoeck, E. F., 1998, *The Molecular Astrophysics of Stars and Galaxies* (Oxford Science Publications, Oxford)

van Dishoeck, E. F. and Black, J. H., 1986, *ApJ*, **307**, 332

van Dishoeck, E. F. and Blake, G., 1998, in *Annual Review of Astronomy and Astrophysics*, volume 36, p. 317

van Zadelhoff, G. J., van Dishoeck, E. F., Thi., W. F. and Blake, G. A., 2001, *A&A*, **377**, 566

Viti, S. and Williams, D. A., 1999*a*, *MNRAS*, **305**, 755

Viti, S. and Williams, D. A., 1999*b*, *MNRAS*, **310**, 517

Wagenblast, R., Williams, D. A., Millar, T. J. and Nejad, L. A., 1993, *MNRAS*, **260**, 420

Watson, W. D., 1978, in *Annual Review of Astronomy and Astrophysics*, volume 16, p. 585

Watson, W. D. and Meyer, D. M., 1996, *ApJ*, **473**, L127

Westley, M. S., Baragiola, R. A., Johnston, R. E. and Baratta, G. A., 1995, *Nature*, **373**, 405

Whittet, D. C. B., Bode, M. F., Longmore, A. J., Adamson, A. J., McFadzean, A. D., Aitken, D. K. and Roche, P. F., 1988, *MNRAS*, **233**, 321

Whittet, D. C. B., Bode, M. F., Longmore, A. J., Baines, D. W. T. and Evans, A., 1983, *Nature*, **303**, 218

Whittet, D. C. B., Gerakines, P. A., Hough, J. H. and Shenoy, S. S., 2001, *ApJ*, **547**, 872

Whittet, D. C. B., Smith, R. G., Adamson, A. J., Aitken, D. K., Chiar, J. E., Kerr, T. H., Roche, P. F., Smith, C. H. and Wright, C. M., 1996, *ApJ*, **458**, 363

Willacy, K. and Langer, W. D., 2000, *ApJ*, **544**, 903

Willacy, K. and Millar, T. J., 1998, *MNRAS*, **298**, 562

Willacy, K. and Williams, D. A., 1993, *MNRAS*, **260**, 635

Williams, D. A., Hartquist, T. W. and Whittet, D. C. B., 1992, *MNRAS*, **258**, 599

Williams, J. P., Blitz, L. and Stark, A. A., 1995, *ApJ*, **451**, 252